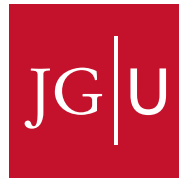# Strong light-matter interaction in confined geometries

Dissertation

Zur Erlangugn des Grades
Doktor der Naturwissenschafter (Dr. rer. nat.)
am Fachbereich Physik, Mathematik und Informatik
der Johannes Gutenberg Universität Mainz

von:
Mohammad Noaman
geboren in Gaya, India
Mainz 2019

JG|U

JOHANNES GUTENBERG
UNIVERSITÄT MAINZ

Declaration

I confirm that no part of the material presented here has previously been submitted by myself for a degree in this or any other university. The work of others has been indicated, wherever applicable.

Mainz, [Date] [Signature]

Mohammad Noaman
QUANTUM
Institut für Physik
Staudingerweg 7
Johannes Gutenberg-Universität D-55099 Mainz
monoaman@uni-mainz.de

Abstract

The laws of quantum physics have attracted immense attention to gain better understanding of the physical model of nature. With the advent of more precision experimental controls, a vast type of applications have been explored and the list is growing consistently. To understand the properties of a real complex many-body system, a quantum simulator becomes the ideal candidate [ref] which is highly complex to solve with the classical computational power. Internet security is one of the key challenges in the present time as the existing communication channel is prone to eavesdropping. The laws of quantum physics suggest a mechanism where an entangled photons pair is an ideal candidate for information exchange. The probabilistic nature of wavefunction collapse makes these photons impossible to clone which lies in the hearts of quantum cryptography [ref]. The use of wave nature of the atoms surpasses the limitations of the optical intereferrometry measurements as the associated wavelength can be prepared extremely small [ref]. Additionally, atoms prepared in a Rydberg states serve strong sensitivity towards external fields [ref]. These quantum sensing aspects open up a whole new dimension to metrology [ref].

To make use of a quantum system atoms can be prepared to represent a quantum state while photons serve as an ideal candidate for interrogation of the state. Thus, strong interaction at single photonic level becomes an important requirement. In this thesis, an atom-optics approach is made towards creating strongly interacting quantum system. To start with, ^{87}Rb atoms are cooled down using laser cooling techniques which provides an easy manipulation of the atomic states. To enhance the light-atom interaction strength, the ongoing probe beam is spatially overlapped with the atomic ensemble. In a free-space setting, such overlap is limited to the Rayleigh range of the probe beam as well as the optical trapping potential. In this project, to overcome the limitation, a hollow-core fiber is used which serves the purpose of first, keeping the trapping laser beam confined and second, simultaneous overlap of the probe beam throughout the length of the atomic ensemble. This project demonstrates an optical lattice configuration, by overlapping two trapping laser beams, to trap and a controllable guiding of cold atoms. This geometrical confinement ensures the extended overlap of the probe light with the atoms which increases the interaction probability. As a figure of merit, optical depth of 200 has been detected. Further manipulation of the probe photons can be achieved in a three level atomic configuration using a process known as electromagnetically induced transparency (EIT). For several interesting applications in quantum domain, strong nonlinearity at single photonic level becomes a key necessity which requires strong photon-photon interactions [ref]. With the EIT process, the photonic states can be mapped on to the atomic states. Thus, a strong photonic interaction can be mediated via atomic interaction. To reach exactly this

goal the EIT configuration is involved with Rydberg states – highly excited atomic states. The atom-atom interaction scales with $n^{1}1$, where n is the principal quantum number of the atomic state.

Rydberg excitation near dielectric surfaces has been a challenging task [ref] due to presence of stray electric fields. This work has demonstrated, for the first time, Rydberg EIT with cold atoms inside a hollow core fiber [ref]. Furthermore, such fibers filled with Rb atoms at room temperature shows significantly lower electric fields. This possibly is due to the homogeneous charge distribution which results in cancellation of field in the core of the fiber. These results open a novel approach for performing quantum optics experiments with neutral atoms. The fiber-atom interface presented in this project further requires a detailed understanding of the propagation of the probe beam through the extended cloud. Here, the atomic ensemble can not only impose attenuation due to absorption but the dispersive effects can modify the actual beam path through the extended atomic cloud. The transmission lineshape gets altered due to the combined dispersion and absorption of the propagating light. To understand the mechanism, a microlensing model is presented which describes the lineshapes for both, a simple two level system and as well as the EIT configuration [ref].

Contents

1. Introduction

Physical processes governed by classical mechanics have been reasonably successful in describing the dynamics of macroscopic systems. However, the same laws do not qualify, in general e.g. at smaller length scales, such as those of atoms or molecules. A fundamentally distinct approach is made to understand the nature of physics where, for example, an atom is conceived to have both, a wave and a particle nature. In this interpretation, furthermore, the nature of light carries particle properties together with the commonly accepted electromagnetic wave characteristics. Such counter-intuitive wave-particle duality provides a better model of light-atom interactions which lies in the roots of a separate division of physics known as atomic, molecular and optical physics (AMOP). Beyond providing a deeper understanding of the laws of nature, the results of AMOP have shown promising boost in both fundamental research as well as technological advancements. However, due to the fragile nature of a quantum system, the practical implementation also comes with a natural cost of precision control and measurement.

With the advancement in the experimental techniques, the gap between the theoretical model and the experimental realization is consistently narrowing down. To this end, one of the most remarkable breakthroughs achieved is the preparation of Bose-Einstein condensate (BEC) [ref] which not only confirmed the theoretical understanding but also opened a plethora of scientific research along with precision applications. As a quantum simulator, many-body systems [ref] have been studied in a wide range of parameter space which otherwise poses extreme experimental requirements. Interesting phase transitions have been explored such as superfluid to Mott insulator [ref] and Fermionization of bosons in a Tonks-Girardeu system[ref]. Wave nature of atoms is explored for measurements of local gravitational fields explore the Einstein's relativity principle. The applications are widely considered in the fields of metrology. As a tool for precision measurements, experiments with cold-atoms lie in the heart of an atomic clock [ref]. Yet another remarkable progress is ongoing for ultra-secure communication using feature of quantum behaviour. The concept of no-cloning of a quantum state allows for a communication channel which is sensitive to eavesdropping [ref]. Quantum computation is a highly spoken topic today as it promises a powerful computation [ref] which can surpass the existing classical systems in certain ways [ref]. With a handful of promising applications, however, the practical implementation comes with a precious cost of a highly controlled experimental demands. The stringent needs are imposed due to the high sensitivity of a quantum system towards the interaction with the environment which induces decoherence – a process known for projecting a quantum system into a classical one. This results in a suppressed contrast and short interrogation time for a given measurement.

1. Introduction

The long term perspective of the work performed for this thesis is developing an experimental platform for utilizing the strengths of quantum mechanics for high precision sensing, quantum information and processing. To achieve this goal, the approach is taken using atom-optics realization. In that the quantum information stored in the form of atomic states or quantum bits also popularly called as qbits can be manipulated via photonic interactions. In particular, the Rb atoms are prepared in a special geometrical setting to enhance light-matter coupling. The exchange of photonic information is mediated via atomic ensemble and thus establishing a novel light-matter interface. For the experiment in lab, laser cooled ^{87}Rb atoms are chosen for this project. The atoms trapped in a ultra-high vacuum (UHV) chamber retain all the properties of an individual atom as the density is too low to have any significant influence between a pair of atoms. This allows for manipulation of multiple atoms simultaneously neglecting the inter-particle interactions. At this stage, the weak nature of atom-photon interaction can partly be compensated by preparing large number of atoms which eventually results in a better signal to noise ratio (SNR). Parallel to that, several approaches are made to enhance atom-photon coupling on individual level such as atoms trapped in cavity where coupling strength is enhanced by a factor associated with the finesse of the cavity [ref]. Here, a single photon traverses multiple times across the atom which which effectively increases the chance of interaction with the atom. In another approach, surface plasmonic coupling is utilized where an atom is coupled to an enhanced near fields. The evanescent field are enhanced at region of interest which eventually enhances the coupling strength with the atoms in a matching dipole radiation pattern.

In this project, an alternative approach is taken where a cold atomic media is trapped in an extended confinement. Following Beer-Lambert law, as a figure of merit optical depth, (OD) scales with the length of such atomic media. This way by using geometrical control the extension length of the cloud can be manipulated and consequently the coupling strength. However, the preparation of such elongated atomic sample along with interacting light field itself is challenging. In typical experiments atoms are trapped in a focusing far red detuned (also blue detuned [ref]) laser beam. Tight confinements become natural need in order to obtain high OD. In free-space this is achieved by focusing the beam very tightly using lenses of high numerical aperture. As it is understood from a Gaussian optics, a tightly focusing beam suffers from extreme divergence. This results in a very shallow region where the atoms are trapped leaving very short interaction zone. To keep the beam confined and yet capable of accommodating cold atoms, a hollow-core (HC) fiber is introduced where a light field can be kept confined throughout the length of the fiber. Utilizing this property and making use of dipole trapping, atoms can simultaneously be held in such confinement. In the recent times, an accelerating research interest can be observed in this field for its promising strengths. Such confinement allows for an extended overlap of a weak laser beam with the atoms which has shown enhancement in light matter coupling as characterized by OD. In such fiber based systems OD of 1000 has been observed [ref]. Strong nonlinearities have been demonstrated for low light levels in such fiber based [ref] system opening a relatively new research window. A compact and ultra-precise

frequency referencing using atoms or molecules filled inside an HC fiber [ref] aims to develop a robust solution. A novel sensor based on atom-interferometry is presented [ref] with cold atoms filled inside HC fiber. Atoms are confined in the Lamb-Dicke regime which have shown phenomenal results in the scope of studying atom-atom interactions [ref].

Now, to induce photon-photon interaction, non-linear processes become natural choice. In that, the usual addition of two fields does hold true. Instead, interesting results such as sum or difference of two frequencies have been observed. Moreover, these non-linear processes can be utilized to generate non-classical photon states which will have its applications in quantum information processing other than performing many-body system with photons. In typical optical materials, such non-linear processes are visible only at higher laser intensities. However, for quantum computation and information processing where such non-linearity is required at very low photon number, typically at single photon level. To enhance the effects, among the various other competitive approaches, the features of atoms excited to very high principle quantum number states have been explored with promising results. These atoms fall in a class known as Rydberg atoms in the honor of Johannes Rydberg. An illustration is shown in Figure 1.1. Saturation at single photon levels have been demonstrated [ref]. In Rydberg atoms, the outer shell electron is weakly bound to the nucleus as a result these atoms are very sensitive to external fields making them an ideal tool for sensor. A number of experimental achievements are made utilizing the features such as high sensitivity [ref]. Furthermore, the weak overlap of the dipole transition from the Rydberg states to the ground states results in inhibited transitions which in effect extends the lifetime of the atoms once prepared in Rydberg state [ref]. This long lifetime allows for treating the system in an alternate "ground" state and has benefits in experiments. Another interesting regime is explored by the enhanced atom-atom interaction [ref]. Due to the presence of one excited atom in a volume of certain radius, all the remaining atoms encounter an energy shift hence no further excitation is possible. This phenomenon is known as Rydberg blockade. The Rydberg blockade effects have been utilized for exchange of photonic information mediated via atomic ensemble as the spatial correlations are mapped onto the photons. The tuneable and long-range interaction has added features which have been utilized in creating many-body photonic states where photons are made to interact with each other in the same way as present in a solid state crystals.

This project aims to combine the two research topics to create a novel system where the benefits of the two individuals are multiplied. For example, one idea is to use the extended cloud to create a chain of Rydberg atoms forming an arrangement of interacting photons. Generation of non-classical photons in this setting can have its advantage due to the extended length as depicted in the Figure 1.2. Here, a coherent light pulse enters into the fiber filled with atoms. By controlled excitation, such as electro-magnetically induced transparency (EIT), the photonic states can be mixed with the atomic states in a generalized system known as polariton. By choosing appropriate Rydberg states, the contribution arising from the atomic interactions can lead to the transfer of the photonic information. The tuneable nature of the atomic
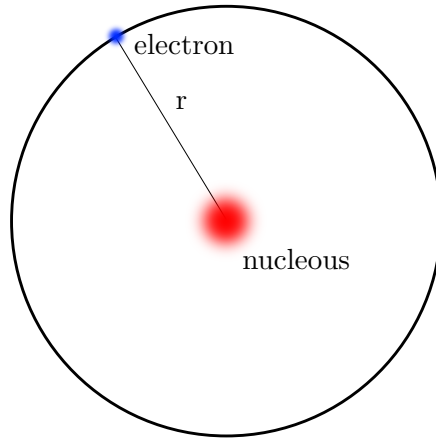
Figure 1.1.: A classical picture of a Rydberg atom. Highly electronic excitation can be visualized as the outer shell electron residing far away from the positively charged core.

interaction provides a knob to manipulate the photon-photon interaction. As the fiber being one dimensional system, interesting states of photons such as observation of Luttinger liquids [ref], Tonks-Girardeu [ref] regimes would be of great importance.
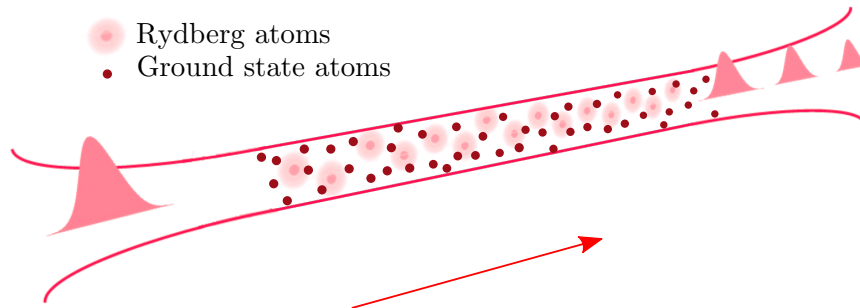
Figure 1.2.: Information stored in the form of atomic states and manipulated with photons. The confinement enhances the interaction probability and providing a quasi-one dimensional configuration.

With the promising long term goals the thesis describes experimental achievements that are prerequisite to establishing strong tuneable photon-atom and consequently photon-photon interactions. To this end, cold atoms of ^{87}Rb are prepared inside a UHV. These atoms are then transferred to optical dipole trap which passes through the HC fiber place inside the UHV chamber. This way atoms are trapped and guided into the fiber. However, in this technique the longitudinal control is not controlled. To gain more control, another optical dipole trap beam from the counter direction is overlapped into the HC fiber. This way the light fields realize an optical lattice configuration which can be set into motion by altering the relative detuning between

the two dipole lasers. The immediate step is to establish an in-line detection scheme as the atoms inside the fiber lose its optical access from other directions. A weak laser beam tuned to the main transition line of the ^{87}Rb is overlapped along with the dipole beams. This naturally confirms the overlap of the atoms with the probe beam. Although this scheme is seemingly simple, the detection requires special attention as the beam encounters a cloud with radially varying density which results in lensing like effects. This work explores the light propagation through the atomic cloud. Consequently, the spectral features are studied which show significant importance in the underlying physical processes for such quasi-one dimensional geometries. Furthermore, the detection of Rydberg EIT signals inside the fibers bring the project a step further towards the main goal. In particular, this step had been debated due to the presence of a silica surface nearby which are known for introducing stray electric fields. A variety of different fibers with inner coating are tested which have produced satisfactory results. Now, understanding the spectral lineshapes of the Rydberg EIT, the similar lensing model was introduced since the added control beam further manipulates the optical response through the two photon process. These studies are of significant importance since various types of lineshapes are observed for different interaction space.
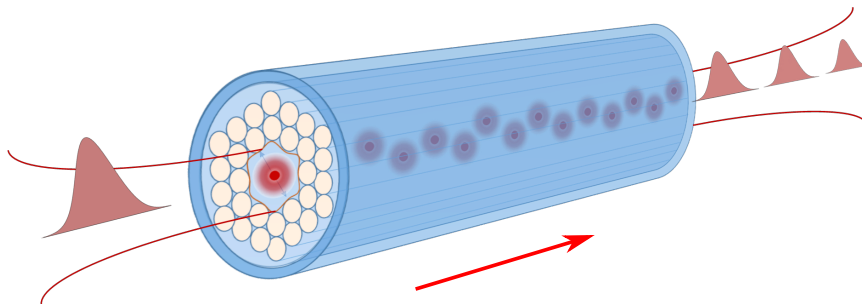
Figure 1.3.: Experimental realization using an HC fiber where both, light and matter can be filled in with an ideal overlap between them.

The Chapter 2 of this thesis overviews a three level system with the main emphasis on EIT involving Rydberg states. In addition to that the EIT features for cold and room temperature atoms are presented. The confinement and the guiding processes are presented in Chapter 3. The main parts are the experimental setup that consists of HC fiber inside the UHV chamber, the optical conveyor belt installed through the fiber that is used for the transport of the atoms and the detection scheme. This chapter further discusses one of the major experimental challenges is to overlap multi-color laser beams which is a prerequisite for the above mentioned experiment. In Chapter 4, the details of the experimental control system is introduced where an FPGA based solution is implemented and integrated with the existing experimental control. For the measurements, a user-friendly, generation of high speed and precise pulse patterns become a must in order to record the dynamics. Furthermore, the pulses need to be stored with accurate timings in order to explore the zone of interest.

Chapter 5 discusses experimental results and analysis of the Rydberg excitation of cold atoms inside hollow core fiber [ref]. These results are the first ever signals with cold atoms inside HC fiber. In a distinct setup a variety of fibers with coating and core structures are installed for characterization of the fiber-atom interactions. Here Rydberg EIT signals are studied to explore a right fiber for the main experiment. The limitations and features of the experiments with hollow core fibers are discussed. In Chapter 6 detailed experimental results and a beam propagation model inside a quasi-one dimensional cloud is studied. The results show a range of valuable information about the light-matter interaction. Moreover, it also explains lineshapes distortion [ref] appearing in the measurement results which could otherwise occur for a variety of reasons.

2. Three level system

In AMOP, atoms can be prepared to represent a quantum system such as cold atoms trapped in a potential created by various types of fields. To address the atomic states, and furthermore, to transport the associated quantum information, photons come a natural choice. Thus, controlled manipulation of light becomes one of the key requirements in the fields of quantum optics. A potential candidate to achieve this goal is coupling the light field to an atomic transition. For near-resonant condition the interaction cross-section is found to have a dramatic increase. Such light-atom setting has been proven as strong candidate for the applications such as quantum information processing, quantum sensing, precision measurements, etc [6, 2, 3].

An atom generally possesses many quantum states labeled by their quantum numbers which are obtained from the solutions of the Schrödinger equation associated with the atom. For convenience, a two level system consists of a pair of quantum states with allowed dipole transition which can be addressed by an electromagnetic field such as a laser beam, or radio frequency (RF) source. A preferred pair of states is chosen with a large dipole transition matrix element which is a measure of coupling strength of the field with the atom. One of the key features of the such atom-optics system is that an atomic species remains always the same irrespective of space and time hence the transition frequency is universally constant as long as the physical quantities such as electric or magnetic fields are kept the same. In addition, certain transition lines in some atoms show extremely narrow linewidth which is utilized for an ultra-stable frequency reference [ref]. These features lie in the heart of an atomic clock where an oscillating clock is referenced and stabilized to the narrow atomic transition. A two level system with long coherence time – a time scale over which the dynamics is governed by the quantum physics – serves as an ideal candidate for quantum information processing. Although a handful of applications are explored with just a simple two level system, control at single to few photons level is still a challenging task. This is mainly because the light-atom interaction strength is insignificant at individual photon level[ref].

Keeping the simplicity of the system, to better control the photons interacting with the two level system, an additional laser field is introduced that couples to a third state. This way a three level atomic system is realized which interacts with two light fields which shows significantly modified response. Allowed by the transition rules, general schemes for three level system with two light fields coupled are shown in the Figure 2.1. Here, three atomic states are indicated by the *ket* notation $|1\rangle$, $|2\rangle$ and $|3\rangle$. The two light fields with associated Rabi frequencies are indicated by Ω_p and Ω_c. The three configurations recognized as Λ type, Ladder type and V type conventionally have state $|2\rangle$ as commonly addressed by the two laser fields. To simplify the processes, in

a case where $\Omega_c = 0$, the system reduces to a two level type, where the remaining laser field labeled as probe beam is only coupled to $|1\rangle \leftrightarrow |2\rangle$ transition. In a case where the probe field intensity is far below the saturation intensity of the transition, strong absorption is observed as the laser frequency matches with the atomic transition line. Now, by increasing the value of Ω_c, i.e. increasing the associated laser field intensity, the spectral features are dramatically modified. Hence the light field associated with $|2\rangle \leftrightarrow |3\rangle$ transition is called control beam. A feature of EIT is to manipulate the probe photons and store them into the atomic ensemble. A general term for such state is called polariton.
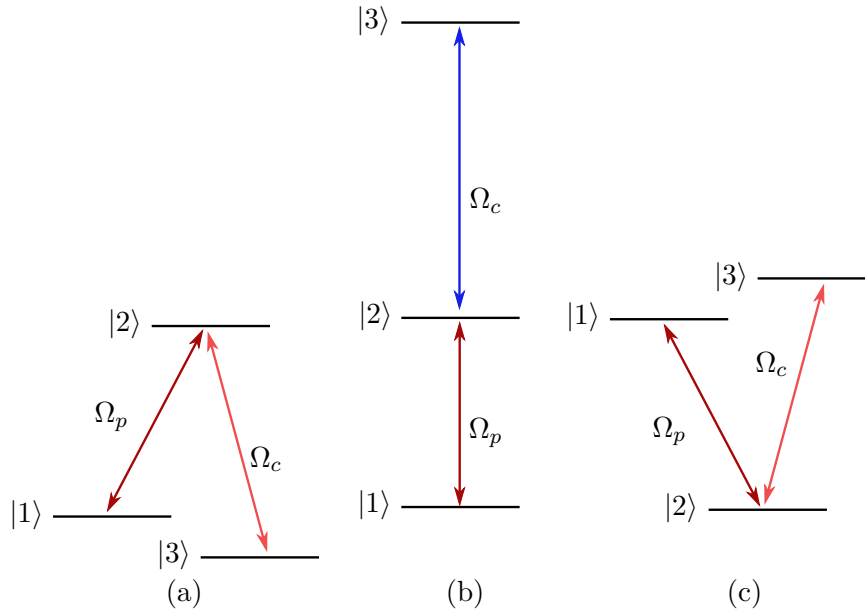

Figure 2.1.: Three-level schemes – (a) Λ type, (b) Ladder type and (c) V type.

Typically, an atomic ensemble prepared for quantum experiments are kept isolated to reduce the environmental influences. Techniques such as laser cooling and trapping have provided a way to confine an ensemble in an isolated space. There the density of the atoms is significantly small as compared to that found at atmospheric pressure and temperature. System prepared at such low temperature and density assures that the atom-atom interaction do not destroy the precise transition features of the individual atoms. Such configurations are favoured for maintaining a long coherence time which is extremely important for storing quantum information in the form of atomic states. A key requirement for a distributed quantum information processing is an efficient exchange of the stored quantum information. In this case, to achieve the goal strong interaction between the photons is desired. One way to create such interaction is to enhance the atom-atom interaction which is highly insignificant for the given atomic separation. This is generally true for atoms lying in low principal quantum number, n, however when excited to large n, the influence of one atom to the neighbouring atoms becomes significantly large. These highly excited atoms are known as Rydberg

atoms [ref]. The nature of such interactions is long-range, where the distances on the order of several micrometers have been observed [ref].

This chapter lays out a foundation for understanding light-matter interaction in different regimes. Interesting results are explored where the two lasers address three states as in the three-level system. While a general solution is rather complicated, certain special cases have shown promising results in the applications of manipulating light for quantum information and sensing aspects. In the early sections, such three level system is explored with different configurations. Furthermore, a section is dedicated to explore features of Rydberg atoms and combine the understanding with Rydberg EIT. Various technical details are also presented related to experimental limitations.

2.1. Electro-magnetically Induced Transparency (EIT)

The way to go about solving the three-level system is to obtain the interaction between the atomic ensemble and the light fields for the given configuration as shown in the Figure 2.1. In the form of total Hamiltonian it is represented as

$$H = H_a + H_i, \tag{2.1}$$

where Ha and H_i are the unperturbed atomic and the interaction Hamiltonians. As the light fields are introduced, one of the most important interests is to obtain the final atomic states. These results will provide the nature of interaction which can be utilized to manipulate atomic states. Moreover, the propagating light fields can also be controlled based on how they couple to the atomic states.

To construct the interaction Hamiltonian, H_i a semi-classical approach is made where light is considered as a wave with oscillating electric field, $\mathcal{E}$. Upon the introduction to an atom, the charges separate in a manner to create an induced dipole moment which then interacts with the field itself. The associated Hamiltonian, H_i is described by

$$H_i = -\mu \cdot \mathcal{E}, \tag{2.2}$$

where μ is the induced dipole moment. This dipole approximation is commonly applied and remains valid as long as the wavelength of the interacting light field is larger than the atomic expansion for the reason that an atom should not experience the spatial field modulation.

In the context of atom being a quantum mechanical system, the light matter coupling strength is obtained by the associated transition dipole moment involving the transition between the two states, $|i\rangle$ and $|j\rangle$ addressed by the laser field. The transition moment elements, μ_{ij} are given by

$$\mu_{ij} = e\mathbf{r}_{ij}, \tag{2.3}$$

where $\mathbf{r}$ is displacement operator with $\mathbf{r}_{ij} = \langle i|\mathbf{r}|j\rangle$ and e is the electronic charge. With the light field, $\mathcal{E}(t) = \mathcal{E}_0 cos(\omega t)$ a convenient way of expressing the light-matter coupling strength is

$$\hbar\Omega_{ij} = -e\mathcal{E}_0\langle i|\mathbf{r}|j\rangle, \tag{2.4}$$

where $\mathcal{E}_0$ is electric field amplitude and Ω_{ij} is Rabi frequency associated with the transition between the two states, $|i\rangle$ and $|j\rangle$.

Now with the general state expressed in the atomic level basis as

$$|\psi_i\rangle = a_i|1\rangle + b_i|2\rangle + c_i|3\rangle, \tag{2.5}$$

the goal is to obtain the three coefficients, a_i, b_i and c_i. By solving time dependent Schrödinger equation,

$$i\hbar\frac{\partial}{\partial t}\psi = H\psi \tag{2.6}$$

the coefficients can be obtained, however it lacks the ability to obtain results for a general case. For instance, situations where mixed states are present or decoherence processes are involved a mixed state can not be represented just by a *ket* vector, $|\psi_i\rangle$. To deal with the problem, the density matrix formalism is implemented where a system is considered as a statistical mixture of pure states,

$$\rho = \sum_i p_i|\psi_i\rangle\langle\psi_i|, \tag{2.7}$$

where p_i is probability of the system being in a given pure state ψ_i. In other words, the matrix from of the density state appears as follows,

$$\rho = \begin{bmatrix} \rho_{11} & \rho_{12} & \rho_{13} \\ \rho_{21} & \rho_{22} & \rho_{23} \\ \rho_{31} & \rho_{32} & \rho_{33} \end{bmatrix}. \tag{2.8}$$

Here, the diagonal elements, i.e. ρ_{ii} represent the population in a given pure state, $|i\rangle$ and the off-diagonal elements represent the coherences between the two states, $|i\rangle$ and $|j\rangle$. The significance of the diagonal elements is that the non-zero value of ρ_{ij} distinguish the system from a classical one, i.e. in a classical system all the off-diagonal terms are zero.

The equivalent Schrödinger equation, known as Liouville equation is derived as

$$\frac{d}{dt}\rho = \frac{-i}{\hbar}\big[H, \rho\big], \tag{2.9}$$

where, $[\cdot]$ is the commutator operator. For the given Hamiltonian the above equation governs the dynamics of the density state. One of the biggest advantages in representing a system in the matrix formalism is that the incoherent processes such as spontaneous decay from different levels can easily be implemented into the equation as

$$\frac{d}{dt}\rho = \frac{-i}{\hbar}\big[H, \rho\big] - \mathcal{L}(\rho), \tag{2.10}$$

where, $\mathcal{L}$ is a general form of Lindblad operator with the components responsible for decay and dephasing rates as shown below

$$\mathcal{L} = \frac{\Gamma}{2}\Big(\alpha^\dagger\alpha\rho + \rho\alpha^\dagger\alpha - 2\alpha\rho\alpha^\dagger,\Big). \tag{2.11}$$
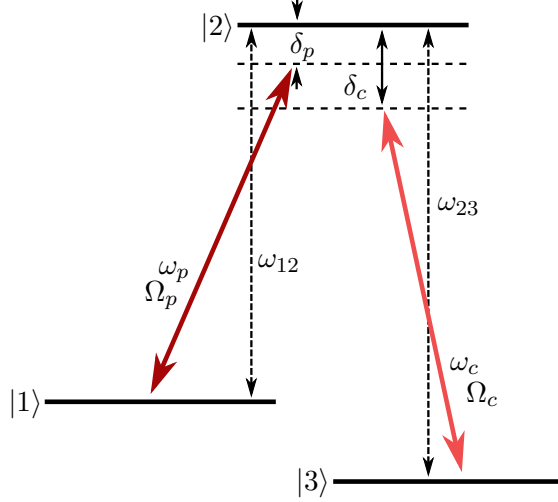
Figure 2.2.: Lambda-type EIT scheme.

Here, $\alpha = |i\rangle\langle j|$ is the atomic projection operator and Γ comprises of decay and dephasing terms from different states.

To construct the mathematical model, for simplicity Λ scheme is considered with various parameters as shown in Figure 2.2. The total Hamiltonian is obtained by the Equations 2.1 and 2.4. Normalizing the ground state, $|1\rangle$ to zero energy the unperturbed atomic Hamiltonian and the interaction Hamiltonian are given by

$$H_0 = \hbar\omega_{12}|2\rangle\langle 2| + \hbar\omega_{23}|3\rangle\langle 3|, \tag{2.12}$$

$$H_i = \frac{\hbar}{2}\Big(\Omega_{12}e^{i\omega_p t}|2\rangle\langle 1| + \Omega_{23}e^{i\omega_c t}|2\rangle\langle 3| + h.c.\Big), \tag{2.13}$$

where, ω_{ij} are the resonance frequencies for the atomic transitions $|i\rangle$ to $|j\rangle$ and $\omega_{p/c}$ are the probe/ control laser frequencies. For the given three-level configuration the Lindblad operator is expressed as

$$\begin{aligned}
\mathcal{L} =& \frac{\Gamma_{21}}{2}\big[2\alpha_{12}\rho\alpha_{21} - \alpha_{22}\rho - \rho\alpha_{22}\big] \\
& + \frac{\Gamma_{23}}{2}\big[2\alpha_{32}\rho\alpha_{23} - \alpha_{22}\rho - \rho\alpha_{22}\big] \\
& + \frac{\gamma_2}{2}\big[2\alpha_{22}\rho\alpha_{22} - \alpha_{22}\rho - \rho\alpha_{22}\big] \\
& + \frac{\gamma_3}{2}\big[2\alpha_{33}\rho\alpha_{33} - \alpha_{33}\rho - \rho\alpha_{33}\big],
\end{aligned} \tag{2.14}$$

where, Γ_{ij} are spontaneous decay rates from the state $|i\rangle$ to $|j\rangle$ and γ_i are dephasing rates for the states $|i\rangle$.

2.1.1. Optical-Bloch equation

Theoretical understanding of the evolution of a multi-level system like presented here is obtained by solving Optical-Bloch equations. The solutions of the Equation 2.10 are multi-fold – the values ρ_{ii} represent the population in the given state $|i\rangle$ and the coherences between two levels are obtained by the ρ_{ij}. The physical significance of the off-diagonal terms is to obtain influence of atomic ensemble on light filed in the form of absorption/ dispersion as will be discussed in the later sections. These parameters are some of the crucial physical components which are measured experimentally in a lab. In particular, the main interest lies here on the estimation of ρ_{12} as this influences the probe light which is detected on a sensor in the from of absorption and phase shift. To obtain the results form the Equation 2.10 the density matrix elements need to be transformed conveniently as

$$
\begin{aligned}
\sigma_{ii} &= \rho_{ii}, & \forall i &= 1, 2, 3 \\
\sigma_{12} &= \rho_{12}e^{-i\omega_p t}, & \sigma_{21} &= \sigma_{12}^*, \\
\sigma_{13} &= \rho_{13}e^{-i(\omega_p - \omega_c)t}, & \sigma_{31} &= \sigma_{13}^*, \\
\sigma_{23} &= \rho_{23}e^{-i\omega_c t}, & \sigma_{23} &= \sigma_{23}^*,
\end{aligned}
\tag{2.15}
$$

where, asterisk $(^*)$ denote complex conjugate with the normalization condition attained by $\sum_i \sigma_{ii} = 1$. In the transformed basis with the consideration of rotating wave approximation the total Hamiltonian simplifies to

$$
H = -\frac{\hbar}{2}
\begin{bmatrix}
0 & \Omega_p & 0 \\
\Omega_p & -2\delta_p & \Omega_c \\
0 & \Omega_c & -2(\delta_p - \delta_c)
\end{bmatrix}.
\tag{2.16}
$$

The Lindblad master equation 2.10 is solved with the transformed matrix elements to obtain the dynamics in the form of differential equations.

$$
\dot{\sigma}_{21} = -(\gamma_{21} - i\delta_p)\sigma_{21} + \frac{i\Omega_c}{2}(\sigma_{22} - \sigma_{11}) + \frac{i\Omega_p}{2}\sigma_{31},
\tag{2.17}
$$

$$
\dot{\sigma}_{31} = -(\gamma_{31} - i(\delta_p + \delta_c))\sigma_{31} + \frac{i\Omega_c}{2}\sigma_{21} + \frac{i\Omega_p}{2}\sigma_{32},
\tag{2.18}
$$

$$
\dot{\sigma}_{32} = -(\gamma_{32} - i\delta_c)\sigma_{32} + \frac{i\Omega_c}{2}(\sigma_{33} - \sigma_{22}) - \frac{i\Omega_p}{2}\sigma_{31},,
\tag{2.19}
$$

$$
\dot{\sigma}_{22} = \Gamma_{21}(1 - \sigma_{22} - \sigma_{33}) + \frac{i}{2}(\Omega_p\sigma_{12} - c.c.),,
\tag{2.20}
$$

$$
\dot{\sigma}_{33} = \Gamma_{23}(1 - \sigma_{22} - \sigma_{33}) + \frac{i}{2}(\Omega_c\sigma_{32} - c.c.),,
\tag{2.21}
$$

where, probe detuning, $\delta_p = \omega_p - \omega_{12}$, control detuning, $\delta_c = \omega_c - \omega_{23}$, and the coherent decay rates defined as, $\gamma_{21} = \Gamma_{21} + \Gamma_{23} + \gamma_2$, $\gamma_{23} = \Gamma_{21} + \Gamma_{23} + \gamma_3$ and $\gamma_{31} = \gamma_3$. As discussed earlier, the main focus is to obtain expression for σ_{21} as it is responsible for the propagation of the probe beam through the atomic medium. One

of the interesting regimes is to explore the steady state solution where the coherences reach an equilibrium situation, i.e. $\dot{\sigma}_{ij} = 0, \forall i, j$. In the case of weak probe beam, i.e. $\Omega_{12} << \Omega_{23}$ the Equation 2.18 reduces to

$$\sigma_{31} = -\frac{i\Omega_c}{2(\gamma_{31} - i(\delta_p + \delta_c))}\sigma_{21} + \frac{i\Omega_p}{2(\gamma_{31} - i(\delta_p - \delta_c))}\sigma_{32}. \tag{2.22}$$

Starting with total population prepared in state $|1\rangle$, for a weak probe beam, the populations in the states $|2\rangle$ and $|3\rangle$ will be a significantly small fraction of the total population. Therefore the value of the coherence, σ_{23} is negligible as compared to σ_{12}. Combining these assumptions, the contribution from the second term in the Equation 2.22 is approximated to zero.

Utilizing the Equation 2.17, the expression for σ_{21} is written as

$$\sigma_{21} = \frac{\Omega_p/2}{\gamma_{21} - i\delta_p + \frac{\Omega_c^2}{4(\gamma_{31} - i(\delta_c - \delta_p))}} \tag{2.23}$$

The optical response is obtained by comparing the analogous macroscopic optical property of a material. From electrodynamics the optical response of a dielectric material can be expressed as

$$\mathcal{P} = \epsilon_0 \chi(\omega_p)\mathcal{E}, \tag{2.24}$$
$$= \epsilon_0 \mathcal{E}_0 \left[\chi(\omega_p)e^{i\omega_p t} + \chi(\omega_p)e^{-i\omega_p t} \right], \tag{2.25}$$

where, $\mathcal{P}$ is polarization vector and χ is susceptibility and is defined as $\chi = \frac{\epsilon}{\epsilon_0} - 1$. Whereas, for an atomic ensemble with density, N the polarization is expressed as

$$\mathcal{P} = N\langle\mu\rangle, \tag{2.26}$$

where, $\langle\cdot\rangle$ is mean value of the dipole operator, μ. In the matrix formalism, the expectation value of an observable is obtained by taking trace of the product of density operator, ρ with the observable. In this case

$$\langle\mu\rangle = Tr(\rho\mu), \tag{2.27}$$

where Tr is trace of the matrix. This simplifies the Equation 2.26 to

$$\mathcal{P} = N\mu_{12}\left[\sigma_{21}e^{i\omega_p t} + \sigma_{12}e^{-i\omega_p t}\right]. \tag{2.28}$$

The μ_{23} do not contribute as it oscillates at completely different frequency. Comparison with the Equation 2.24 leads to an expression for susceptibility as follows

$$\chi = -\frac{2N|\mu_{12}|^2\sigma_{21}}{\hbar\epsilon_0\Omega_p} \tag{2.29}$$

The above expression for χ is expanded for the experimental settings which are measured in lab and results in more practical form

$$\chi = \frac{\sigma_0\rho(x,y)}{k_0}\frac{i\gamma/2}{\gamma/2 - i\delta_p + \frac{\Omega_c^2(x,y)}{\Gamma/2 - i(\delta_p + \delta_c)}}, \tag{2.30}$$

where, σ_0 is on-resonance cross section and is defined as

$$\sigma_0 = \frac{\hbar\omega\Gamma}{2I_{sat}}, \tag{2.31}$$

where, Γ is decay rate, I_{sat} is saturation intensity.

In the absence of the control beam, i.e. $\Omega_c = 0$ the expression for χ reduces to that for a two level system

$$\chi = -\frac{\sigma_0 N(x,y)}{k_0} \frac{2\delta_p/\gamma - i}{1 + 4(\delta_p/\gamma)^2}. \tag{2.32}$$

The real and the imaginary parts are related to the macroscopic complex refractive index by the following equations

$$n_r = 1 + \frac{1}{2}Re[\chi], \tag{2.33}$$

$$n_i = \frac{1}{2}Im[\chi]. \tag{2.34}$$

The imaginary part is associated with absorption due to on-resonant scattering of light, while the real part is responsible for phase shift in the beam as the laser beam propagates through the medium. The line shapes obtained from the imaginary part of the susceptibility are shown in Figure 2.3 where the probe beam is scanned near resonance while a control beam is set to resonance. As the control power is applied, which results in a non-zero Ω_c, the transmission line shape opens up at the probe detuning which was completely absorbing otherwise. This process of creating artificial transmission using light is commonly known as electro-magnetically induce transparency or EIT. In a two-level system, the typical lineshape appears as shown by the black (dashed) line. In the presence of the control beam, the transmission peaks appears as shown by the red (solid) line.
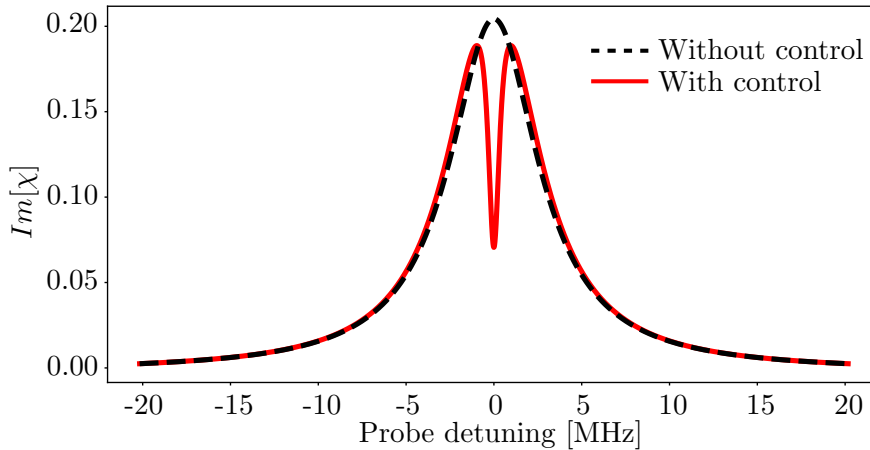

Figure 2.3.: Transmission line shapes for probe scan. In the presence and absence of control laser.

The Real part of the susceptibility which is responsible for phase shift of the propagating beam is shown in the Figure 2.4. The medium becomes extremely dispersive as the refractive index, n_r changes significantly with the laser detuning, ω_p. The value of $\frac{dn}{d\omega}$ is a measure of dispersion.
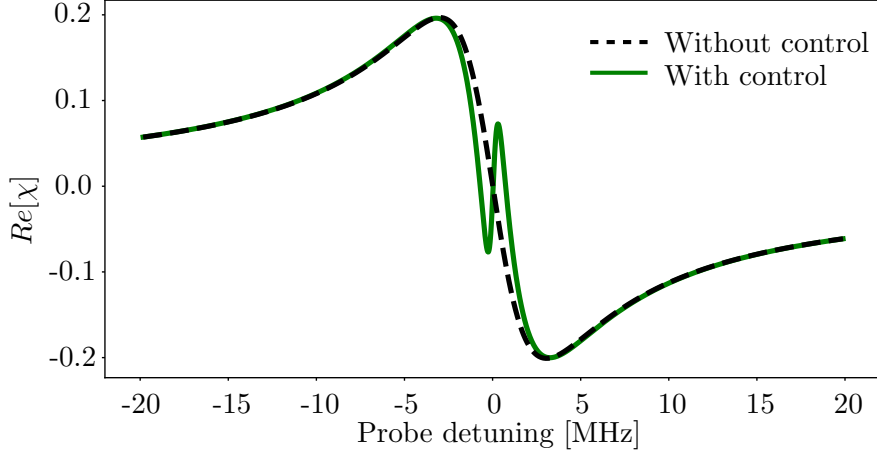

Figure 2.4.: Transmission line shapes for probe scan. In the presence and absence of control laser.

2.1.2. Absorption

As has been discussed in the previous sections a light beam passing through a cloud of atoms encounters significant change in the beam by means of both absorption and dispersion. The results are quantified by the real and imaginary components of refractive index. The absorption of light is related to the reduction in intensity while dispersion is responsible for phase shift. The absorption line shape is illustrated in this section while the significance of the dispersion is left for the Chapter 6. To quantify the values, as a figure of merit, optical depth, OD is estimated by

$$I = I_0 e^{-OD}, \tag{2.35}$$

where, I and I_0 are the intensities of the incoming the outgoing beam through the atomic medium. The transmission is defined as $I/I_0 = e^{-OD}$. Value of OD is obtained from the imaginary part of the refractive index as

$$OD = 2k_p n_i l, \tag{2.36}$$

where, k_p is magnitude of wavevector, i.e. $2\pi/\lambda_p$ and l is cloud length through which probe beam propagates. The results are illustrated in Figure 2.5 for various OD values.
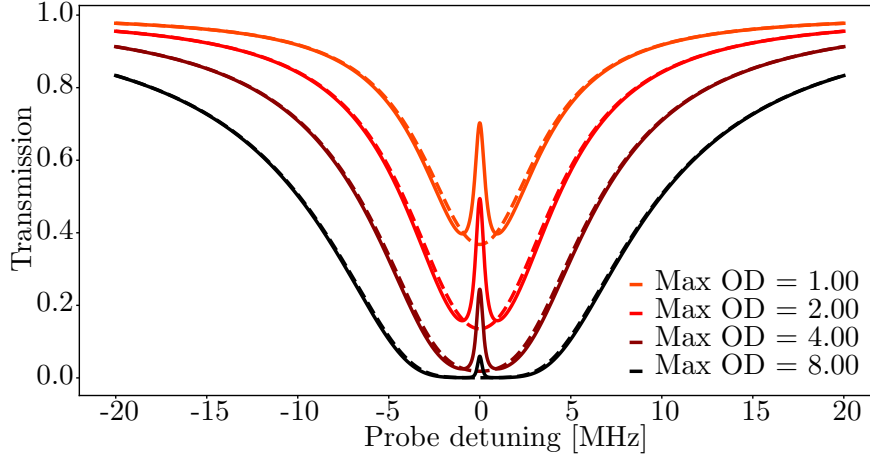
Figure 2.5.: Transmission signals for different optical depths. Dashed lines represent transmission without the presence of control field and solid lines for EIT lines.

2.1.3. Slow light

One of the remarkable results of near the resonant detunings is that the values of both, $Im[\chi]$ and $Re[\chi]$ vary dramatically. The situation becomes a lot more interesting in case of EIT conditions. The refractive index, n_r is responsible for propagation speed of the given wavepacket. This relates to the group velocity of the light as follows,

$$v_{group} = \frac{d\omega_p}{dk_p} \tag{2.37}$$

where k_p is wavenumber in a given medium and is related as

$$k = \frac{\omega_p}{c} n(\omega_p). \tag{2.38}$$

Now, using the Equations 2.38 and 2.37, the expression for group velocity is obtained as follows,

$$v_{group} = \frac{c}{n + \omega_p \frac{dn}{d\omega_p}} \tag{2.39}$$

Depending upon the laser parameters, such as power and detuning the value of dispersion, $\frac{dn}{d\omega_p}$ becomes extremely high. This results in extremely low group velocity. In certain cases, speeds of several m/s have been measured. In terms of control Rabi frequency, Ω_c the group velocity is expressed as

$$v_g \approx \frac{\hbar c \epsilon_0}{2\omega_p} \frac{|\Omega_c|^2}{|\mu_{12}|^2 N}. \tag{2.40}$$

The dependence of v_g on the control Rabi frequency provides an easy way to tune the speed of the propagating light pulse in a medium.

2.1.4. Dressed state picture

In a special case with $\delta_c = \delta_p = \delta$, the expression for Hamiltonian, Equation 2.16 reduces to

$$H = -\frac{\hbar}{2} \begin{bmatrix} 0 & \Omega_p & 0 \\ \Omega_p & -2\delta & \Omega_c \\ 0 & \Omega_c & 0 \end{bmatrix}.$$
$$(2.41)$$

To obtain the eigenstates conveniently a set of mixing angle terms are defined as follows,

$$\tan\theta = \frac{\Omega_p}{\Omega_c},$$
$$(2.42)$$

$$\tan 2\phi = \frac{\sqrt{\Omega_p^2 + \Omega_c^2}}{\delta}.$$
$$(2.43)$$

The eigenstates for this Hamiltonian are

$$|\psi_+\rangle = \sin\theta\sin\phi|1\rangle + \cos\phi|2\rangle + \cos\theta\sin\phi|3\rangle,$$
$$(2.44)$$

$$|\psi_D\rangle = \cos\theta|1\rangle - \sin\theta|3\rangle,$$
$$(2.45)$$

$$|\psi_-\rangle = \sin\theta\cos\phi|1\rangle - \sin\phi|2\rangle + \cos\theta\cos\phi|3\rangle.$$
$$(2.46)$$

The state ψ_D is called dark state as it is evident from the above expression it has no contribution from the intermediate state, $|2\rangle$. This means that the lack of the overlap with the intermediate state $|2\rangle$ leads to no scattering of the laser beams, hence atoms in the dark state are transition forbidden. In other words, on the one hand once the atoms are prepared in $|\psi_D\rangle$ they remain there as the two states, $|1\rangle$ and $|3\rangle$ are long-lived as compared to $|2\rangle$. On the other hand the states, $|\psi_+\rangle$ and $|\psi_-\rangle$ can "leak" into the dark state due the overlap between the atomic states $|1\rangle$ and $|3\rangle$. As a result, due to the unidirectional process once the above conditions are met, the atoms would end up in dark state in a process known as *coherent population trapping* (CPT). Now, by adjusting the relative Rabi frequencies of the probe and the control beams, the contribution of the two long-lived stated to the dark state can be controlled. Let's assume the probe beam is very weak, i.e. $\Omega_p << \Omega_c$, that means the dark state mostly consists of state $|1\rangle$. By slowly increasing the power of the probe beam in an adiabatic manner, i.e. $t_{ramp} << 1/\Omega_c$, the contribution of the state $|3\rangle$ can be increased. Simultaneously, by reducing the control power the dark state can be prepared with full contribution from the state $|3\rangle$ in a process known as *stimulated Raman adiabatic passage* (STIRAP).

The intermediate state in many cases are short lived thus causes limitations on coherence time. In the case of EIT processes, the intermediate state can be completely avoided and the coherence processes are then mainly dependent on the two long-lived states. Combined with the result from the Equation 2.40, the group velocity of the propagating probe beam can be reduced to zero by reducing the control Rabi frequency. This makes it a powerful tool to store the probe photons into atomic ensemble. Here both, the photonic states and atomic states are mixed together coherently

in what is known as polaritonic states. Furthermore, by adiabatically ramping up the control laser power the stored probe photons can be retrieved on demand. Such precision control over light is being explored in the fields of quantum optics and quantum information.

2.2. Rydberg atoms

In the most simple atom – Hydrogen, the observation of the discrete energy lines is a profound example of quantum mechanical processes. The results were generalized by Johannes Rydberg and formulated as follows

$$\Delta\nu = \mathcal{R}\Big(\frac{1}{m^2} - \frac{1}{n^2}\Big), \tag{2.47}$$

where, m and n are integers corresponding to the associated transition states and $\mathcal{R}$ is recognized as Rydberg constant. Later, the integers, m and n were interpreted as the principal quantum numbers by Bohr [1]. The value of the Rydberg constant, $\mathcal{R}$ is obtained as

$$\mathcal{R} = \frac{Z^2 e^4 m_e}{2(4\pi\epsilon_0\hbar)^2}, \tag{2.48}$$

where, Z, e, m_e and $\hbar$ are atomic number, electron charge, electron mass and Planck constant.

Atoms in ground state are typically found in low lying energy levels with the principal quantum number, $n < 8$. By various means these atoms can be excited to higher principal quantum states. Rydberg atoms refer to the atoms when they are excited to principle quantum numbers beyond around 20 and could range up to 100 or above. In such scenarios, the outer shell electron has a weak overlap with the nucleus and the remaining electrons. consequently, this loosely bound electron is prone to strong perturbations due to presence of relatively weaker external fields. Such fields can be produced from charges, magnetic field, etc. including neighbouring atoms in the ensemble. These perturbations can be measured by means of spectral features, such line shapes, shift, etc. and it gives important information about the nature of interaction and the underlying physics. In addition to the highly enhanced sensitivity, the Rydberg atoms have shown extended lifetimes which is a highly favourable requirement for exploring applications in quantum memory storage, information processing and quantum sensing. In the upcoming subsections, some of the most exotic features are discussed along with the basic properties. Some of the interesting features are highlighted in the Table 2.1.

2.2.1. Energy states

The configuration of a Rydberg atom resembles closely to a Hydrogen-like atom as the outer shell electron experiences a central potential. The approximation breaks down for the case when the outer shell electron wave-function lies close to the nucleus. A non-zero azimuthal quantum number, L further adds complexity in the model due

Properties	n* scaling	$5S_{1/2}$	$61S_{1/2}$
Polarizability	n^{*7}	$1.96e^{-7}$	$2.08e^{+2}$
Orbit radius	n^{*2}	$5.6a_0$	$4797.7a_0$
Lifetime at $0\,\mathrm{K}$	n^{*3}	$26.4\,\mathrm{ns}$ $(5P_{3/2} \rightarrow 5S_{1/2})$	$242.7\,\mu\mathrm{s}$
Lifetime at $300\,\mathrm{K}$	n^{*2}	$26.4\,\mathrm{ns}$ $(5P_{3/2} \rightarrow 5S_{1/2})$	$105.0\,\mu\mathrm{s}$
Blockade radius	$\sim n^{*1}$	$\sim \mathrm{nm}$	$6.2\,\mu\mathrm{m}$
Dipole moment $(nS_{1/2} \leftrightarrow nP_{3/2}\,)$	n^{*2}	$2.99\,ea_0$	$-2201.94\,ea_0$
Energy spacing $(nS_{1/2} \leftrightarrow nP_{3/2})$	n^{*-3}	$3.84 \cdot 10^{14}\,\mathrm{Hz}$	$1.64 \cdot 10^{10}\,\mathrm{Hz}$

Table 2.1.: ^{87}Rb Rydberg atom properties. Comparison of typical values for $5S_{1/2}$ and $61S_{1/2}$ states. The values are adapted from [ref].

to its angular dependence. A quantum defect, δ_{nLJ} is introduced to account for the deviation from the exact Hydrogen model. The mathematical from of the energy eigenvalues of a Rydberg atom is expressed as

$$E_{nLJ} = -\frac{hc\mathcal{R}}{(n*)^2} = -\frac{hc\mathcal{R}}{(n - \delta_{nLJ})^2}, \qquad (2.49)$$

where, n^* represents an effective principal quantum number whereas n, L and J are the principal, azimuthal and total angular quantum numbers. Besides a simple model the Rydberg atoms offer a wide range enhanced features suitable for experiments in atomic physics. The main attraction comes from the ability to tune these features by adjusting very few parameters. For instance, By choosing a particular Rydberg state, n, L or J, the sensitivity towards external fields can be tuned very precisely. Experimentally this is achieved by addressing the state by laser detuning. As evident from the Equation 2.49, the line spacing for higher principal quantum numbers become narrower in the order of sub-nanometer wavelengths. This allows for easy addressing of multi-levels using a single tunable laser source.

2.2.2. Long lifetime

The radiative coupling to the ground states are relative weak for higher Rydberg states as the wave function overlaps tend to diminish. As a consequence the transition dipole matrix elements have significantly smaller values as compared to atoms in the lower states. This results in prohibition in decay to the ground states from the

Rydberg states. The enhanced lifetime scaling, shown in the Table 2.1 is favourable for experiments that seek longer coherence times. In this case, the lifetime of immediate higher state ($5P_{3/2}$) is only 26.4 ns whereas that for the higher state is orders of magnitude longer. such long lifetimes allow for treating the excited states as an alternate "ground" state which is the backbone for realization of EIT using Rydberg states. For applications like storage of photon and quantum information processing have been particularly benefited from such longer lifetime. At the room temperature the lifetime further suffers from alternate decay channels induced by the black-body radiation (BBR) as the broad spectral radiation initiates the coupling through the neighbouring states. This way atoms prepared in certain Rydberg state branches its coherence through multiple states which leads to an additional decay rate. The effective lifetime is calculated by

$$\frac{1}{\tau_{eff}} = \Gamma_0 + \Gamma_{BBR} = \frac{1}{\tau_0} + \frac{1}{\tau_{BBR}}, \tag{2.50}$$

where, τ_0 and τ_{BBR} are lifetime at 0 K and at 300 K. Interestingly, even for the additional decay channels opened at room temperature the lifetime for $61S_{1/2}$ state is above 100 µs which is significantly large for certain time-critical experiments.

2.2.3. Stark shift

In the presence of an electric field, the energy level of a Rydberg state gets shifted in a process what is known as Stark effect. It can be understood from the argument that the electron being loosely bound to the nucleus can encounter stronger deviation as compared to the ground state atoms where and outer shell electron is tightly bound. Using perturbation treatment, the Stark shift is estimated for a given pair of states which results in a shifted transition peak. It turns out that the first order Stark shift is absent due to the selection rule associated with the atomic transition, whereas the second order shift is still present and it is quadratic in nature. Furthermore, the different sub-levels have significantly altered line shifts for a given electric field which is quantified as

$$\Delta = \frac{1}{2}\alpha|\mathcal{E}|^2, \tag{2.51}$$

where, α is polarizability. The value of α scales rapidly with the principle quantum number as presented in the Table 2.1. An enhancement of 9 orders of magnitude can be obtained for an $n = 61$ state. The high sensitivity has been utilized for sensing very weak electric fields such as those found near surfaces due to atom depositions [ref]. In the later part in this thesis the field sensitivity aspects have been explored to estimate field inside the HC fiber.

2.2.4. Rydberg-Rydberg interaction

The large polarizability associated with the Rydberg atoms has significant enhancement in sensitivity towards an external electric field. Such fields, however, can also

be generated from the charge distribution of an another Rydberg atom in the near vicinity. Therefore, a strong electric potential between the two Rydberg atoms can be expected. In the classical picture such interaction can be understood by considering the two atoms with dipole moment, μ_1 and μ_2 separated by a distance R as shown in figure 2.6. Here, the interaction is considered among the positively charged nuclei and the negatively charged outer electrons. In the quantum mechanical description, the dipole matrix elements are expressed as $\mu_{ij} = \langle i|er|j\rangle$ and the dipole-dipole interaction is given by

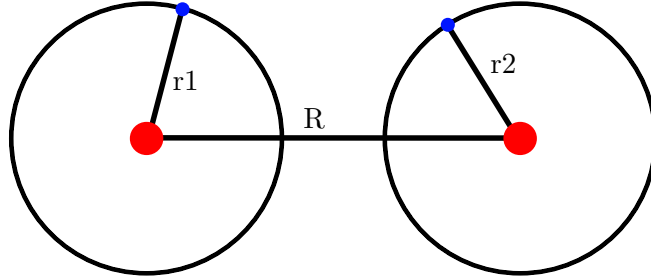$$U_{dd} = \frac{\mu_1 \cdot \mu_2}{|R|^3} - 3\frac{(\mu_1 \cdot R)(\mu_2 \cdot R)}{|R|^5}. \tag{2.52}$$

Figure 2.6.: Two atoms prepared in Rydberg state, separated by a distance R. The mutual interaction among the outer electrons and the nuclei has dipolar nature.

The second term in the equation 2.52 signifies angular dependence and can be ignored for isotropic states, as in the case with S state [ref (Walker and Saffman)]. In this case where the atoms are prepared in the same Rydberg state, $|nS\rangle$, the dipole interaction is expressed as

$$U_{dd} \propto \frac{1}{R^3}\sum_{\phi_1,\phi_2}\langle nS|\mu_1|\phi_1\rangle\langle nS|\mu_2|\phi_2\rangle = \sum_{\phi_1,\phi_2}\langle nS,nS|\frac{\mu_1\mu_2}{R^3}|\phi_1,\phi_2\rangle, \tag{2.53}$$

where, ϕ_1 and ϕ_2 are all the dipole transition allowed states. However, for practical calculations, the main contribution comes from $|nP\rangle$ and $|(n-1)P\rangle$ states. To illustrate the interaction, an excitation of a virtual photon can be considered as a result of one atom undergoing transition from its initial quantum state $|nS\rangle$ to either $n|P\rangle$ or $(n-1)|P\rangle$. The wavelength associated with the photon lies in the microwave regime due to the narrow spacing for higher Rydberg states. In experimental settings, the wavelength can be much larger than the inter-atomic distances and thus it satisfies the near-field condition. In this scenario, the excited photon interacts with the neighbouring atom resulting in a state transition. The dipole-dipole interaction results in exchange of atomic energy as

$$nS + nS \leftrightarrow nP + (n-1)P. \tag{2.54}$$

The right most part of the expression 2.53 represents the interaction in the pair state basis. In that the initial pair state, $|nS, nS\rangle$ is coupled by U_{dd} to the state $|nP, (n-1)P\rangle$. The defect in the energy, i.e. $\Delta_F = E_{nP} + E_{(n-1)P} - 2E_{nS}$ is called Förster defect and has significance in describing the shift associated with the interaction energy. In the pair state basis, the Hamiltonian is written as:

$$H = \begin{bmatrix} 0 & U_{dd} \\ U_{dd} & \Delta_F \end{bmatrix}, \tag{2.55}$$

with the eigenvalues

$$U_{\pm} = \frac{\Delta_F}{2} \pm \sqrt{\left(\frac{\Delta_F}{2}\right)^2 + U_{dd}^2}. \tag{2.56}$$

From the above expression, two separate solutions arise in the asymptotic cases, i.e. $\Delta_F << U_{dd}$ and $U_{dd} << \Delta_F$. In the case when the atoms are very close, the value of U_{dd} is very large as it has a R^{-3} dependence. In this limit, the eigenvalues are written as

$$U_{\pm} = \pm \frac{\mu_1 \mu_2}{R^3}. \tag{2.57}$$

This type of interaction is termed as dipole-dipole interaction with the well-known form $U_{\pm} = \pm \frac{C_3}{R^3}$. Here, it can easily be realized that the dipole coefficient, C_3 scales as n^{*4}.

In a more interesting regime where the two atoms are very far apart, U_{dd} would be negligible as compared to Δ_F. In this limit, the shift in the energy level of the pair state, $|nS, nS\rangle$ can be calculated using Taylor expansion as

$$\Delta U = -\frac{U_{dd}^2}{\Delta_F} = -\frac{(\mu_1 \mu_2)^2}{\Delta_F R^6}. \tag{2.58}$$

Here, the expression can be seen as van der Waals potential with $V_{vdw} = -\frac{C_6}{R^6}$ with the coefficient, $C_6 = (\mu_1 \mu_2)^2/\Delta_F$. Interestingly, it can easily be shown that the value of C_6 scales with n^{*11} since Δ_F is similar to the energy spacing, it scales with n^{*-3}. The significance of such strong scaling can be perceived in the form of long-range interaction for higher principal quantum number state. Additional interesting result can be observed for cases such as addressing different quantum states where the sign of Förster defect, Δ_F can be altered giving rise to repulsive or attractive potentials [ref]. Moreover, by applying external fields, the sign of the Förster defect can be tuned giving an experimental handle to tune the nature of interactions[ref].

2.2.5. Rydberg blockade

As is being discussed, high electric fields can be generated due to the excitation of one atom to Rydberg state which can shift the energy levels far apart. If the Stark shift is beyond the characteristic laser linewidth, the atom would be off-resonant to the given transition and hence would not excite to the same Rydberg state. The inverse square dependence of electric field forms a volume of radius, known as blockade

radius where no further Rydberg excitation is possible. For a state, $n = 61S_{1/2}$ the Rydberg blockade radius is above $6\,\mu$m which is orders of magnitude larger than a single atom radius. One way of Rydberg excitation is using three-level excitation in the case discussed under EIT section. In that the critical requirement for the Rydberg excitation is that the two lasers must match the respective transition lines. Within the Rydberg blockade radius, clearly the EIT condition is destroyed which leads to additional consequences. In the given blockade volume, once an excitation is made all the other probe photons would be absorbed. This result can be seen as extreme non-linearity induced at single photon level [ref]. An illustration is presented in the Figure 2.7.
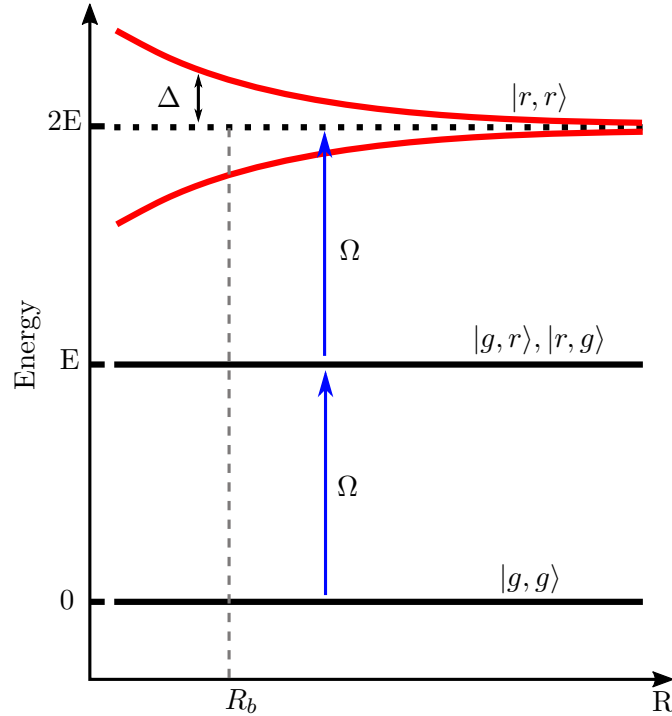

Figure 2.7.: Rydberg blockade. Excitation of two atoms to Rydberg states within the volume is prohibited. The red lines indicate the shifted energy line in case of pair excitation. The sign of the potential can be tuned to create attractive or repulsive.

Another remarkable aspect of the Rydberg blockade can be seen as the excitation being shared among all the atoms within the given volume as there is a finite probability of each atom undergoing through the Rydberg excitation as illustrated in the Figure 2.8. This leads to a phenomenon known as collective excitation which enhances the light-matter coupling strength as represented by

$$\Omega_{tot} = N^{1/2}\Omega, \tag{2.59}$$

where, Ω_{tot} is two-photon Rabi frequency of single atom coupled to the light fields
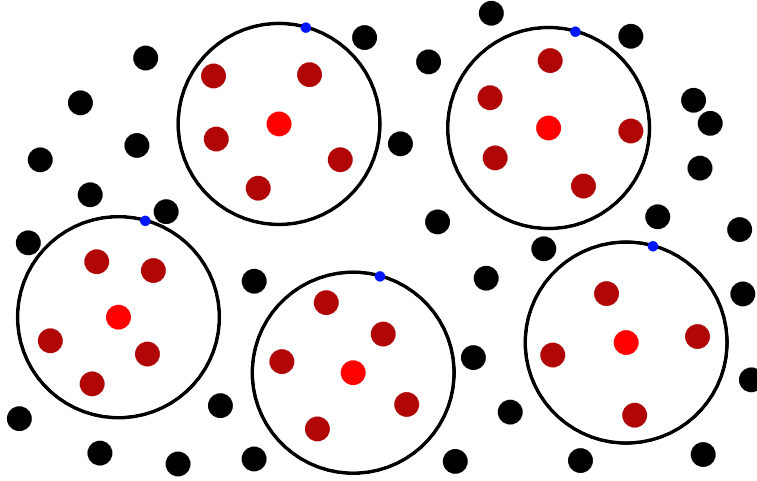
Figure 2.8.: Collective excitation within the blockade volume. Black dots represent ground state atoms. Brown and red dots represent atoms sharing the Rydberg excitation.

and N is number of atoms within the blockade radius. In another words, the collective excitation represents Rabi oscillation as seen in a two level system but with an enhancement due to the multiple atoms present in the blockade volume. In this regard, the entire collection can be thought of as a super-atom with an scaled enhancement in light-matter coupling strength.

2.3. Rydberg EIT

In this section, the features of the two previously discussed sections, i.e. EIT and Rydberg atoms are combined together. On the one hand, through EIT precision control over light is acheived by making it transparent or dispersive. On the other hand, the Rydberg atoms offer a range of enhanced interactions. The combined system has shown promising applications in the fields ranging from quantum simulation to quantum sensing, quantum information processing and communication.

For the experimental techniques, cold atoms makes a clean environment for precision measurements. In this case where the linewidth of the EIT line shapes could be 100s of KHz broad, the measurements would be very clean as the broadening due to Doppler effects associated with the atom motion is seized. The process of Rybderg excitation involves shining two lasers in a ladder configuration as depicted in the Figure 2.9. For Rb the two wavelengths are 780 nm and 480 nm for the probe and the control transitions. The laser detuning schemes shown in the figure need to be considered to obtain the two photon resonances. In the case of cold atoms where $v_{at} = 0\,\text{m/s}$, such as the case being discussed here the line shift due to Doppler effects are absent. Therefore, the two configurations, counter-propagating and co-propagating cases show no difference on the spectral features. Only for the experimental constraints, in case

of co-propagation scheme, the strong control needs to be decoupled from the sensitive detector. The lineshapes are shown in figure for different Ω_c. The two-photon resonances occurs at $\delta_p = -\delta_c$ for either cases. For increasing control power the transmission increases while it also increases the broadening. The outcomes are highly linked with the Autler-Townes splitting which is a regime where the control power is much higher such that the two peaks appear separately[ref].
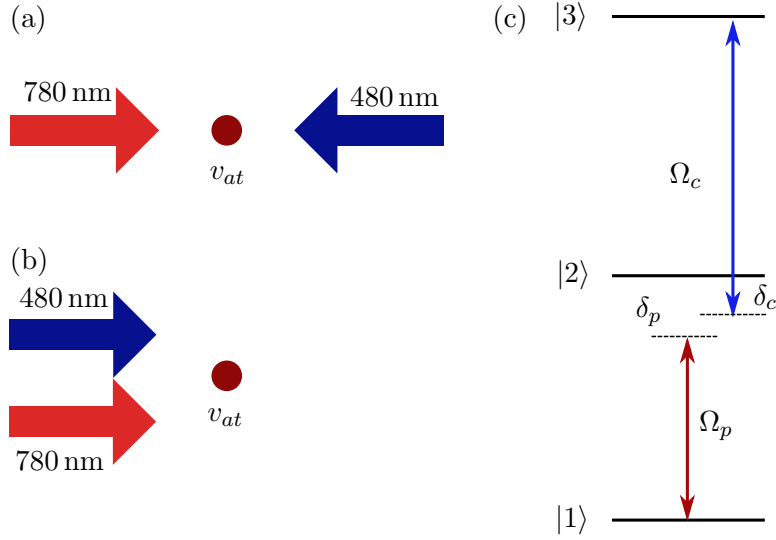

Figure 2.9.: EIT schemes: (a) counter-propagating and (b) co-propagating configurations. (c) Ladder type EIT scheme with probe and control detunings.

As was discussed previously, utilizing EIT process quantum information of a photon can coherently be stored to the atomic ensemble. Here, the strong tunability nature of Rydberg atoms can be introduced to effectively create photon-photon interaction. The EIT line is plotted in the Figure 2.10 where conveniently control laser is scanned while the probe laser kept on-resonance. This way the atomic absorption lineshape is completely removed from the study of EIT lineshape which will be of significant importance in the coming sections.

2.4. Rydberg EIT with thermal atoms

While it is spectroscopically very clean to work with cold atoms, the preparation and feasibility sets experimental limitation due to demanding constraints. Cold atom experiments require a systematic control of a large number of lasers and different fields. Measurements are limited to a fraction of time over it takes to prepare. Vapour cells filled with atomic samples have shown interesting results in certain experiments. In particular, EIT measurements when done in a Doppler free arrangement leads to much better line shapes comparable to that obtained from cold atoms measurements. In this case, the two configurations have significant effects on the detected spectral features.
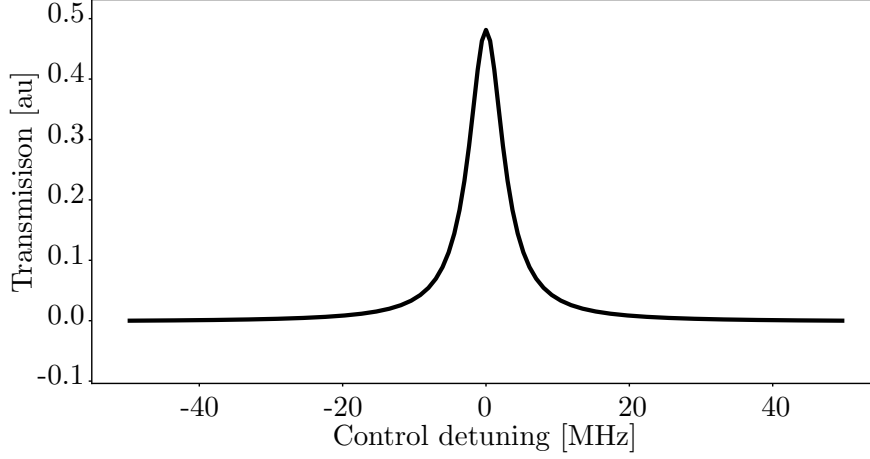
Figure 2.10.: EIT line shape for cold atoms. Control beams is frequency scanned and the probe laser is kept on-resonance.

In one case, where the beams are in co-propagating, the Doppler shift adds to the two laser beams and the total effect is highly adverse. In the case where the beams are counter-propagating, the shifts tend to cancel each other and hence the results are much better. However due to mismatch in the wavelengths, the cancellation is not complete which results in deviation in the lineshape from the cold atom lineshapes.

To calculate the susceptibility, the atomic velocity distribution is integrated over the entire velocity range dictated by the temperature. The susceptibility from the Equation 6.8 for a given velocity class atoms is

$$\chi(v) = \frac{\sigma_0 \rho(x,y)}{k_0} \frac{i\gamma/2}{\gamma/2 - i(\delta_p + \delta_p^v) + \frac{\Omega_c^2(x,y)}{\Gamma/2 - i((\delta_p + \delta_p^v) + (\delta_c + \delta_c^v))}}, \tag{2.60}$$

where, δ_p^v and δ_c^v are the shift in the probe and control laser frequencies due to Doppler effect. The values are calculated by

$$\delta_c^v = k_c v_{at}, \tag{2.61}$$

$$\delta_p^v = k_p v_{at}, \tag{2.62}$$

where, k_p and k_c are probe and control wavevectors and v_{at} is the velocity of the atoms. The susceptibility for the complete velocity class is calculated by integrating over the given velocity distribution as

$$\chi = \int_v G(v)\chi(v)dv, \tag{2.63}$$

where, $G(v)$ is the Boltzmann distribution.

2.4.1. Doppler free line shape

The thermal velocity distribution of the atoms results in shifted EIT features as presented by the equations 2.61. However, interesting geometrical arrangements can be made to cancel the shift in the lineshapes. It is apparent that for the ladder type EIT, counter propagating pair of the probe and the control lasers counteract the shift. To illustrate this, in the Figure 2.9(a) the atom with velocity would see one laser upshifted while the other laser downshifted. This way the EIT conditions are met. However for the case of $\Lambda-$type EIT, it would be the copropagating configuration that does the cancellation of the shifts.

A simulated model using the Equation 2.60 is plotted in the Figure 2.11(b). Here, the EIT lines for different velocity classes are represented by the 6color bar.
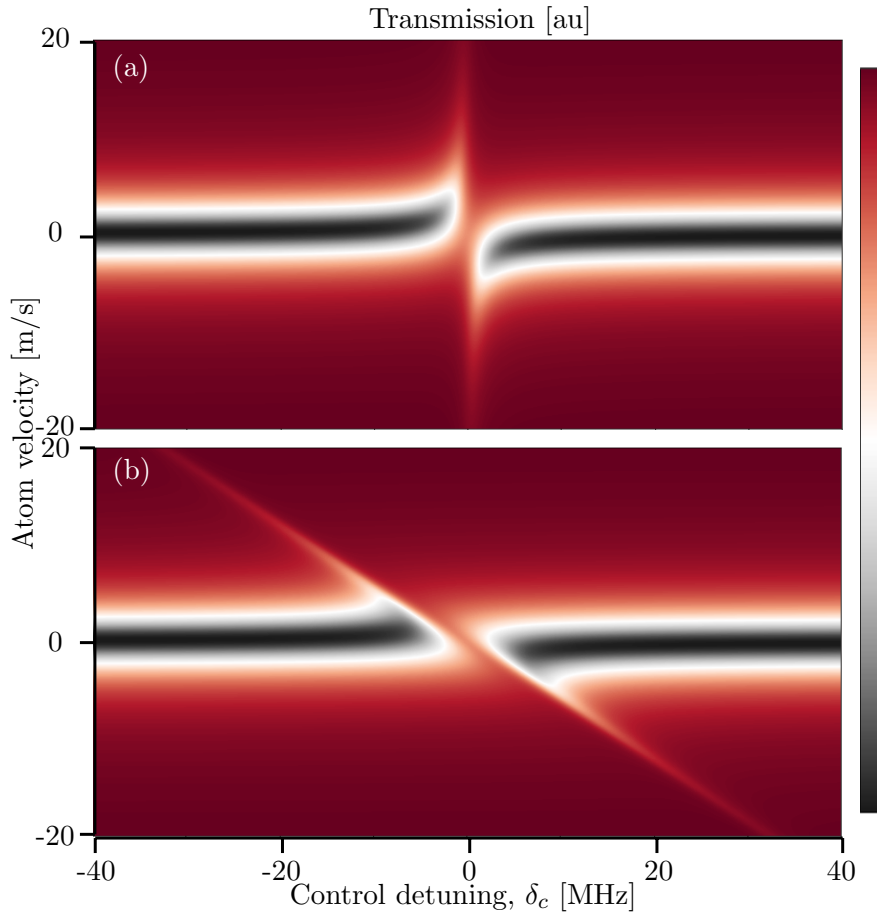

Figure 2.11.: Transmission contour for atoms of different velocity class, with (a) no Doppler mismatch and (b) Doppler affected EIT.

An easy visualization is made by plotting horizontal cuts for few velocity classes as shown in Figure 2.12(b). As it is clear from the fact that the Rydberg EIT with this scheme where the two wavelengths $\lambda_p = 780\,\text{nm}$ and $\lambda_c = 480\,\text{nm}$ are distinctly

different the Doppler compensation will not be completely effective. It is clearly noticeable that the peaks for different velocity classes are shifted apart.
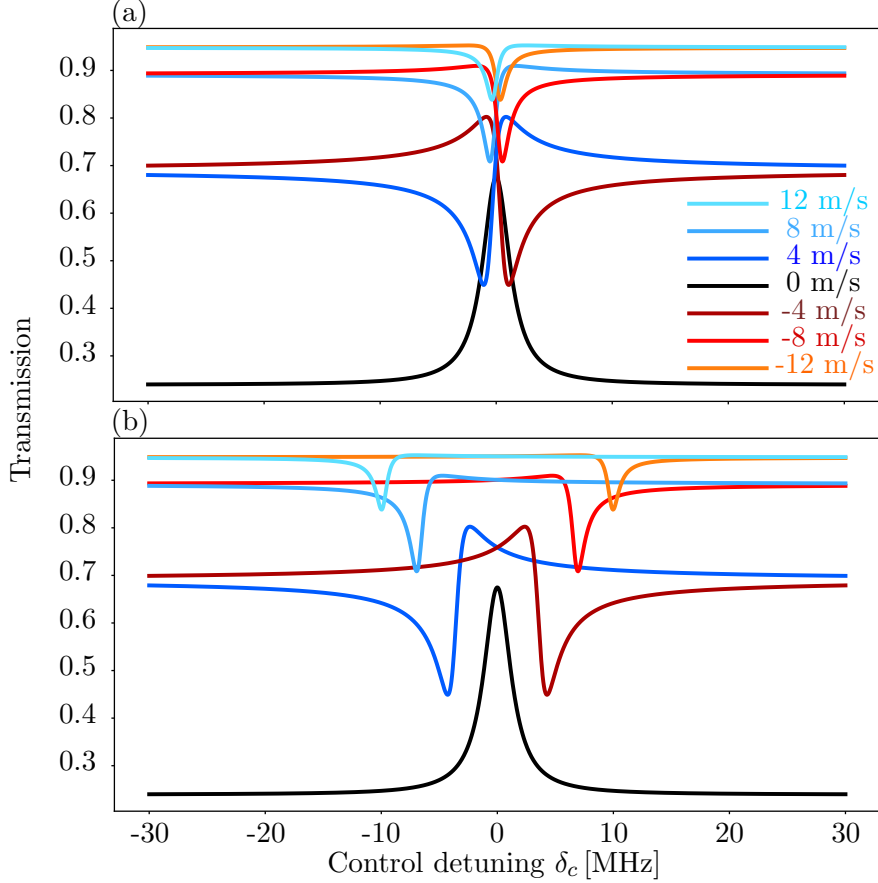

Figure 2.12.: EIT lines for several velocity class atoms towards the probe beam. No Doppler mismatch (a) EIT lines and Doppler affected traces (b) are shown.

For comparison, a hypothetical situation is presented in the same ladder-type EIT scheme but the two wavelengths chosen to be the same. The simulated model as shown in Figure 2.12(a) clearly shows the peaks mainly stay at zero detuning confirming a complete cancellation of the Doppler shifts. The 2D EIT map of this scheme, shown in Figure 2.11(a) appears significantly different than the former case.

The complete EIT lineshape for the thermal vapour is compared in the Figure 2.13 by adding the contributions from all the velocity classes. The surprising dips can be noticed near ± 5 MHz detuning as a clear signature of Doppler mismatch. Interestingly, the signal from the cold atom and that from the hypothetical thermal vapour looks extremely overlapping.
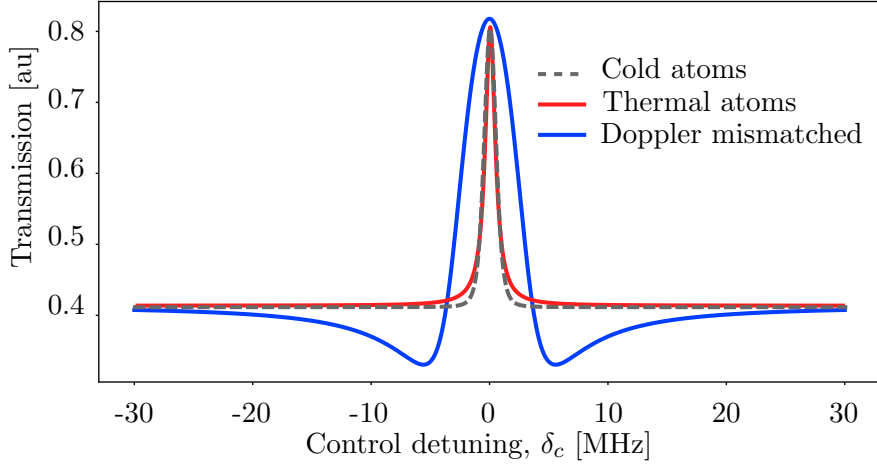
Figure 2.13.: EIT lines at different conditions. Scaled to fit for perspective.

2.5. Broadening mechanism

Even though the intermediate state involved in the EIT process has a linewidth of 12 MHz, the observed EIT signals are much narrower. Obviously, this is one of the features of the EIT that the intermediate state does not contribute in the dynamics. However, the linewidth of an EIT process still depends on the physical conditions such as the temperature of the vapour, power of the control laser along with the intrinsic coherence time. The study of the broadening mechanism uncover the underlying physical processes. In what follows, some of these mechanisms are discussed.

2.5.1. Doppler mismatch

The model discussed for the thermal vapour illustrates the contribution of the Doppler mismatch. Here due to the incomplete cancellation, the linewith and lineshape are both distinct from either Lorentzian or voigt. Therefore, it becomes difficult to assign any characteristics linewidth. Instead, the complete thermal vapour EIT model needs to be solved in order to obtain the actual physical processes causing the broadening.

2.5.2. Lifetime of Rydberg states

As seen in equation for χ the line shape has dependence on the coherences, γ and Γ for different states. Furthermore, the coherence timescale for the Rydberg state has n^{*3} dependence on the principle quantum number as shown in the Table 2.1. Therefore, for higher quantum state the linewith gets narrower and is favoured for precision experiments as the other quantities also show positive effects.

2.5.3. Control Rabi frequency

The line width of the EIT line shape is roughly proportional to the control Rabi frequency for larger Ω_c as it adds to the original linewidth. As the control Rabi frequency is intensity dependent which has a spatial distribution, it becomes important to consider the complete spatial Rabi frequency distribution to understand the lineshape.

2.5.4. Transit time broadening

During the probe time if the atoms under detection move away, it would result in drop of a signal associated with the transition. The width in time is related uncertainty in measurements. The energy-time uncertainly, which results from Fourier transformation, dictates corresponding broadening in the line shape. For cold atoms it is does not play any significant role as the motion of the atoms are seized. The situation is not so favourable with the atoms at room temperature. In cases where a considerably large probe beam is used, the time an atoms takes cross the beam could be significant resulting in linewidths of several 100s KHz which may be insignificant as compared to other broadening mechanism. However, when the beam sizes are very small, the interaction time becomes much shorter and the associated linewidth needs to be considered. Figure shows transit time broadening for different probe beam size for atoms at room temperature.

Atoms moving with average speed, v_{av} takes time,

$$t_{tr} = d/v_{av}, \tag{2.64}$$

where $t_t r$ is transit time, d is beam diameter. The expression for v_{av} at a given room temperature is obtained by thermal velocity distribution,

$$v_{av} = \left[\frac{8k_B T}{\pi m_{Rb}}\right]^{1/2}, \tag{2.65}$$

where, K_B is Boltzmann constant, T is absolute temperature and m_{Rb} is mass of individual Rb atoms. The transit time leads to broadening the transition line due to the time limitation on the detection process. This is based on the uncertainty principle as the exposure time is inversely related to the precision in observed linewidth. In the particular case, where thermal atoms are transported inside a hollow-core fiber, the beam size is limited to $40\,\mu$m. The associated transit time is on the order of $150\,$ns which leads to a line broadening of $\sim 5\,$Mhz.

3. Atoms in quasi-one dimensional confinements

One dimensional quantum systems have drawn considerable attention in the experimental as well as in theoretical physics. The simplicity and feasibility make such systems particularly suitable for practical applications. While such system represents a simple model, it still provides detailed information about the underlying physics in a quantum mechanical process. One of the crucial experimental realizations is a chain of trapped cold atoms which represents a many-body system with a plethora of control parameter space. Such as BEC to BCS cross-over transition has been observed in such system just by tuning the trap depth of the lattice confinement [ref]. In the heart of such confinements lies the trapping potential created by coherent optical forces such as those created by dipole traps. However, in free space the trapping region is limited due to the optical wave propagation. This limitation adversely affects the light-matter interaction. To overcome this problem, a novel experimental system is presented in this chapter. Here, the cold atoms are transported inside a hollow core fiber making them confined for infinitely extended quasi-one dimensional geometry. The key feature of the experiment is to gain a better control over the atoms along both, transverse and longitudinal directions. In atomic physics, generally light-matter coupling strength is weak in nature. A simple approach is to extend the region of light-matter overlap so that the encountering photons spend longer time together the atoms. For a naturally limited scattering rate, this extension in interaction time would scale up the total number of scattering events.

An important motivation concerning this project is to overcome the limitations found in exciting more than one or two Rydberg atoms in a chain[ref]. In a free-space trapped-atom configuration, due to the limited Rayleigh length and blockade radius, it has become a challenging task to excite more than two Rydberg atoms in a chain[ref]. The setup presented in this project promise to overcome the limitation by creating an extended trapped atomic cloud. Thus the setup provides an ideal condition for excitation of multiple Rydberg atoms in a chain. Creation of interacting photons and thus interesting regime such as Luttinger liquid or fermionization of photons are some of the long term goals[ref].

In this chapter, general principal of optical trapping is introduced with the limitations of free space trapping. Using hollow-core fiber as a remedy to overcome the confinement lengths is presented in subsequent sections. To gain a better axial control over the atoms, a conveyor belt is realized by creating standing wave of trapping field which allows for precise positioning of the cold atoms along the fiber length.

3.1. Free-space beam propagation

In free space, as shown in figure 3.1, a Gaussian beam is confined using a lens which is characterized by the Rayleigh range,

$$z_R = \frac{\pi w_0^2}{\lambda},\tag{3.1}$$

where, w_0 is beam waist and λ is the wavelength of the propagating beam. At distance, z_r away from the focal point, the beam size increases to $\sqrt{2}$ times the beam waist. It is clearly evident that for a tighter focal point, i.e. smaller w_0, the confinement length, z_R becomes smaller.
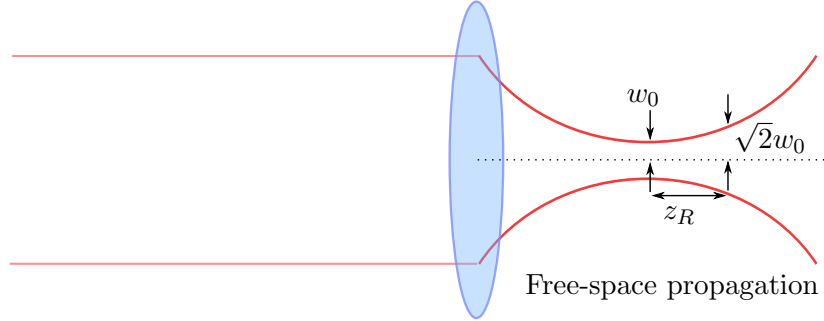

Figure 3.1.: Beam confinement in free space using a lens leads to immediate expansion.

A general form of a Gaussian beam evolution is given as

$$w(z) = w_0 \sqrt{1 + (\frac{z}{z_R})^2},\tag{3.2}$$

where, z is the axial distance from the focal point. The beam size expansion takes a linear form for larger distances.

3.2. Optical dipole trap

In presence of a light-field, a two-level atom shows response that depends on the wavelength of the light beam. When the laser beam and the atomic transition frequencies are the same, it results in resonance condition. In this case, the scattering of photon from the atom is maximized. Each scattering event imparts a momentum to atom which is equal and opposite to the scattered photon. This is the underlying principle explored for laser cooling techniques by manipulating the atomic motion. However, as discussed in the earlier chapter, this process is random which induces decoherence phenomena in a quantum system. For storage of a quantum system such traps are highly restricted.

Interesting results have been explored in the case, when the laser detuning is kept very far from the atomic transition. In a classical picture, the charge distribution

of an atom responds to the electric field present in the light beam. The magnetic interaction is much weaker and hence it is ignored. It is the induced dipole moment due to the light field which in turn creates a potential for the atom when it interacts with the light field. At this stage, depending upon the sign of laser detuning the atom either gets attracted to or repelled from the laser beam. In case, when the laser detuning is negative, i.e. the electric field oscillation is slower than the atomic transition frequency, the atomic charge distribution is capable of following the electric field change. Such process leads to attractive potential for the atoms. Conversely, for the blue detuning case, the induced dipole of an atom does not follow the change in field hence it encounters a repulsive potential. For a Gaussian beam geometry, the trapping laser has to be red detuned in order to trap the atoms. This type of trap is known as dipole trap for the reasons explained here.

The off-resonant scattering and the trap depth depends on the laser detuning as

$$\Gamma_{sc} \propto 1/\delta^2, \tag{3.3}$$

$$U_{dip} \propto I/\delta, \tag{3.4}$$

where δ is detuning of the laser and I is the laser intensity. Even though the proportionality constant for scattering rate is higher, the steeper $1/\delta^2$ term rapidly decays to zero while, the dipole trap term is still non-negligible.

For this experiment, the laser was tuned to $805\,\mathrm{nm}$ which corresponds to negative detuning for all the major transition lines. The total force is estimated by considering both, the D1 and the D2 lines. Even though the D1 transition strength is weaker, the laser detuning is rather small for this transition hence its contribution can not be avoided. The exact trap depth of a dipole beam is expressed in the forms of detunings from the D1 and D2 lines as

$$U_{dip} = 2\pi c^2 \Big[\frac{2\Gamma_{D2}}{\omega_{D2}^2 \Delta_{D2}} + \frac{2\Gamma_{D1}}{\omega_{D1}^2 \Delta_{D1}} \Big] I(r,z), \tag{3.5}$$

where, Δ_{D1} and Δ_{D2} are detunigs from the corresponding energy states and the ω_{D1} and ω_{D2} are the on-resonant transition frequencies for the $D1$ and $D2$ states.

Now, considering a typical Gaussian intensity distribution, the atoms are attracted towards the center of the beam as the trapping potential is minimum at the focal point as illustrated in figure 3.2.

For the focusing Gaussian beam using a lens, the atom density takes the shape of the dipole trap beam which has significant importance in manipulation of the atomic cloud. In this case, the atom distribution is governed by the potential which has a wider spread along the beam propagation direction. As a result, position control over the atoms is not precise. A strong periodic longitudinal modulation is introduced to trap and precisely locate the cold atoms which is discussed in the next section.
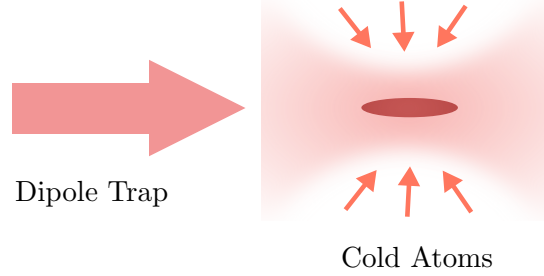
Figure 3.2.: Atoms in optical lattice.

3.3. Optical lattice

The limitation due to the smooth and shallow potential along the beam propagation axis is broken by adding additional trapping beam from the counter direction. In the case, when the two lasers are derived from the same source, i.e. the phase and the frequency stay fixed, the two beams form a standing wave pattern. This results in longitudinal intensity modulation with a periodicity of $\lambda/2$. The atoms are attracted towards the intensity maxima and thus they end up trapped in the periodic potential. This resembles the lattice configuration as seen in a solid state crystal, thus it is widely known as optical lattice.

The optical potential for the lattice configuration mainly follows the euqation 3.5 with a modified intensity pattern

$$I(r, z) = I_0 \exp\left(-\frac{2r^2}{w(z)^2}\right) \cos^2(\phi - kz), \tag{3.6}$$

where, ϕ is the relative phase between the two lasers and k is the wavenumber associated with the laser beam. The intensity for the two laser beams is modified as

$$I_0(r, z) = \frac{2P}{\pi w(z)^2}, \tag{3.7}$$

where, P is the power in each of the beams. For maximum intensity modulation, the powers in each of the beam is kept equal. The intensity pattern and subsequently the trapping potential simulated for the lattice configuration is illustrated in the figure 3.3. Note the scale is exaggerated for visual clarification.

3.3.1. Conveyor belt

Atoms trapped in the optical lattice have tight radial confinement due to beam focusing. However, the axial confinement is even more steeper due to the formation of standing wave as a result of interference which has extent of $\lambda/2$. Atoms stay trapped in the local potential wells even though the global minima does not coincide with it. Such confinement has been explored for trapping and isolating atoms for quantum mechanical experiments. Such as configurations where atoms are trapped from an
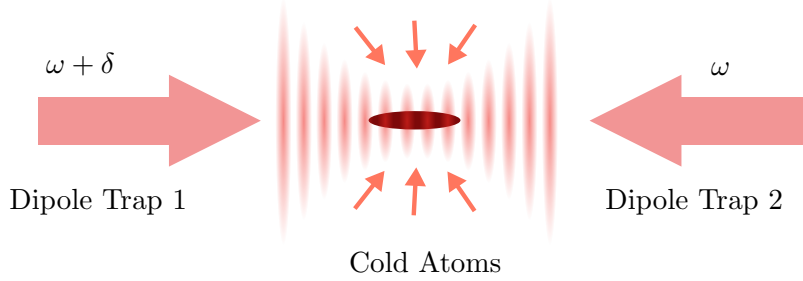
Figure 3.3.: Atoms realized in optical lattice with $\delta = 0$.

accessible region, i.e. MOT cloud and transported to regions which are inaccessible [ref].

At this stage, it turns out from the equation 3.7 that the axial position of the lattice sites can be shifted by modulating the phase, ϕ. The trapped atoms will now follow the potential and occupy the new location given that the change in ϕ is slow enough. The constraints on the rate is described by the adiabaticity condition

$$\dot{\phi} << \omega_{trap}, \tag{3.8}$$

where, ω_{trap} is the trap frequency.

Now, by introducing a phase shift in one of the laser will shift the lattice position, keeping the same lattice periodicity. In a typical experiment, one of the lasers is detuned precisely creating a continuous moving lattice, known as optical conveyor belt. With the help of optical conveyer belt, atoms are trapped and transported along the optical lattice beams in a highly controlled manner.

3.4. Light-matter interaction

The light matter interaction is achieved by overlapping a probe beam along with the atomic cloud. As a figure of merit, OD signifies the strength of coupling. For a given atomic density, the OD scales with the length of the interaction length, l as

$$OD \propto \rho l, \tag{3.9}$$

where, ρ is atomic density.

As it is clear for a free space beam, the length of the interaction region, l is roughly equal to the Rayleigh range, z_R which sets a natural limitation on the maximum OD. Even for atomic cloud trapped in an extended length by other means such as magnetic trapping [ref], the probe beam does not stay overlapped with the entire atomic region. Hence, this technique results in a limited light-matter interaction strength.

A way to overcome this limitation is to utilize a waveguide such as an optical fiber. However, in order to accommodate both, the light beam and the atoms, a typical solid core fiber fails to meet the goal. An ideal solution would be an empty core

waveguide where atoms can potentially be filled in as illustrated in figure 3.4. In the guided geometry, the Rayleigh range has no limitation that is found in free-space propagation. This feature can be utilized to extend the length, l for macroscopic distances ranging several cms as opposed to the free-space case where this length is limited to few 100's of μm [ref]. ODs above 1000 have been realized in such simple arrangements [ref]. Such goal is met by hollow core fibers which is the central topic of discussion for the next section.
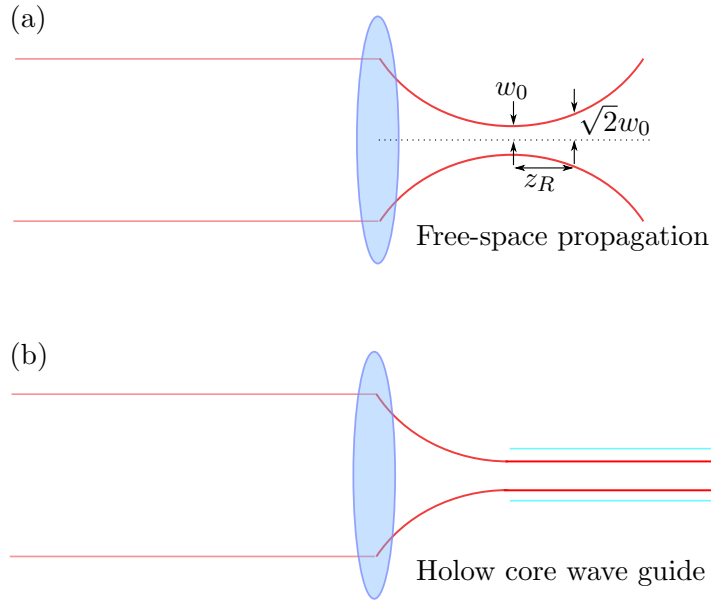

Figure 3.4.: Light beam diverges in free space. A guided wave stays confined.

3.5. Hollow-core fibers

Guided transmission of light has been critical and revolutionary to a wide range of applications. As a typical example, optical fibers have been implemented for along with scientific research, inter-continental high speed data transfer via sea-link fiber cables. In a typical atomic physics lab, fibers are utilized for carrying light close to the main experiment. Common to all these fibers, the principle of light guiding relies on the total internal reflection. A necessary step for this condition is a definite relationship between the refractive indices on the core and the cladding. In particular, the refractive index of the core material needs to be higher than the cladding in order to support the guiding mechanism. Such conditions, however, set limitations on manipulation of light. For example, transport of high power laser beam could induce non-linearity in the core medium which can lead to damages or losses. To circumvent the issues, in the recent times a different approach have been made to guide light which crucially relies on the light propagation through the empty space in the core. This not only allows for high power transmission but also offer very low or no distortion on

the light field. Moreover, the empty core now can be filled with atoms or molecules to produce a range of interesting physics in a confined geometries which otherwise is limited due to free-space beam divergence as has been discussed in the previous sections.
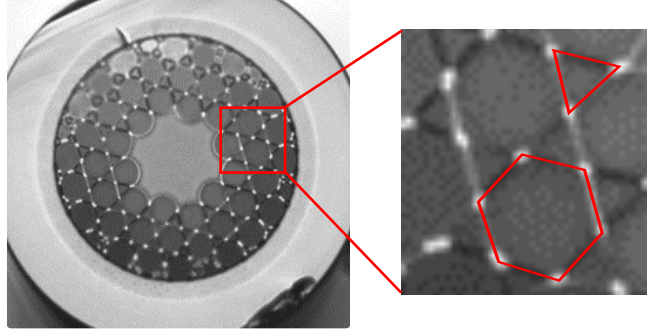
Fiber tip

Figure 3.5.: Cross section of the fiber. Empty core is surrounded by lattice structure which is responsible for light guiding. Zoomed shot of lattice structure indicating Kagome type lattice.

The fibers used for this work are produced in the group of Dr. Fetah Benabid at XLIM, Limoges, France. A Kagome type lattice structure of the core is shown in the figure 3.5. The periodic lattice structure is responsible for an interference pattern which has none of very small values for the outside the core region. In a process known as inhibited coupling, the guiding mechanism is well explained [ref]. With such a large core size, the fiber is highly multi-moded. As a result higher spatial order mode of light can be excited and supported by the fiber. A critical requirement for the trapping and transporting of atoms utilizes the Gaussian beam shape. Moreover, the light-matter overlap for creating strong interaction demands guiding of the same mode. Hence, a careful coupling procedure is needed in order to excite the fundamental mode of light into the HC fiber. In what follows the characterization procedure of the fiber is presented in the coming subsections. Another technical aspect concerning the cleaning of the HC fiber for UHV compatibility is discussed in the appendix C.1.

3.5.1. Light guiding

One of the key requirements for the chosen fiber is the guiding properties of the different wavelengths which are required for trapping and transport of atoms followed by two-photon Rydberg EIT excitation. In particular, the associated wavelengths are $810\,\mathrm{nm}$, $780\,\mathrm{nm}$ and $480\,\mathrm{nm}$ for ^{87}Rb atoms. Important aspect here is to observe the mode quality in addition to the coupling efficiency for different wavelengths. The test and characterization of the mode shape and coupling efficiency are performed separately before installing the fiber inside the UHV chamber to benchmark the fiber properties.

In the figure 3.6, the test and characterization setup is sketched. The HC fiber is mounted on an XYZ translation stage along with a lens that can be replaced for better optimization. By adjusting the micrometer mounts, the mode quality is optimized.
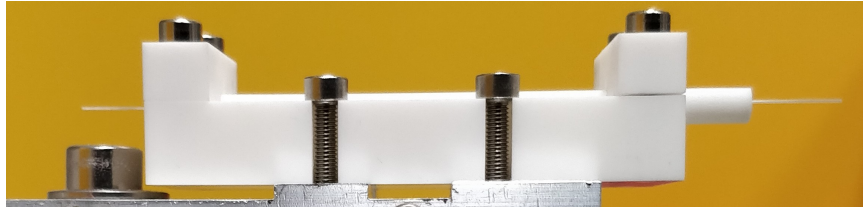
(a)
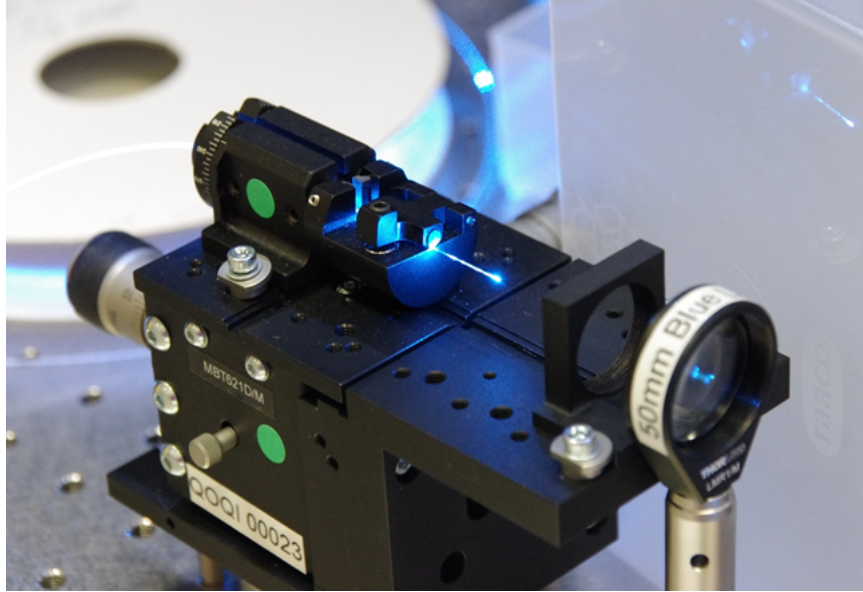
(b)

Figure 3.6.: (a) HC Fiber characterization setup. Fiber position adjustments made with micro-meter knobs. (b) The fiber placed in a V-groove made in a ceramic holder horizontally inside the UHV system

The coupling is a challenging task, particularly for the reason that the $10\,\mathrm{cm}$ long fiber is capable of guiding higher order modes. In this case, the usual optimization technique where the output power is maximized, fails to work. Misaligned beam can still be guided through with little or no drop in the total intensity. The strategy here is to observe the mode shape and optimize for a Gaussian shape. In the figure 3.7, a set of different mode profiles are displayed. The focal length of the lens and the incoming beam diameter is selected to match the mode field diameter (MFD) of the fiber by using Gaussian optics. In the initial stage, when the incoming beam just hits the fiber cladding, the Kagome structure pattern can be illuminated as seen in the figure 3.7(a). By iteratively optimizing the angle and the lens position of the beam,

the coupling in the fundamental mode can be enhanced. The results are indicated by the figures 3.7(b), (c) and (d). One good indicator of a good coupling is the mode shape starts to appear smooth and less sensitive to fiber tapping.
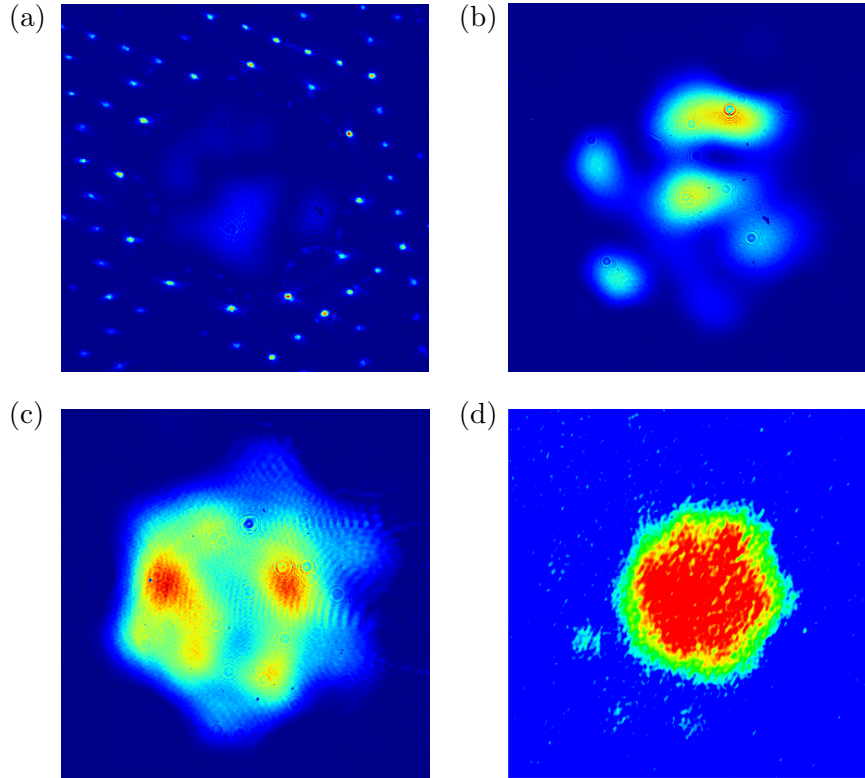

Figure 3.7.: Near-field mode profile at different coupling stages. The hexagonal pattern is an indicator of the 6 periodic edges of the core.

Different wavelengths are detected for the near field and the far field configurations as shown in the figure 3.8. The coupling efficiency for all the wavelengths is obtained above 95 % which is a favourable for the atom transport and the EIT spectroscopy.

3.5.2. Mode matching

One of the key requirements for the formation of standing wave is the overlap of the counter-propagating dipole trap beams. Particularly interesting is to explore the feasibility in the cases where the beams are propagating through the HC fiber. As the HC fiber is highly multi-moded, the quality of overlap is not always guaranteed to be perfect. For the simplified fiber setup shown in figure 3.9 the reasonable way is to roughly couple the dipole trap beam, DT1 into the HC fiber. The outgoing beam is coupled into the DT2 single mode fiber. Now, retracing the path, the dipole beam, DT2 is overlapped and coupled into the HC fiber. The transmitting beam is now coupled into the DT1 fiber. By improving the coupling iteratively, the best

Near field   Far field
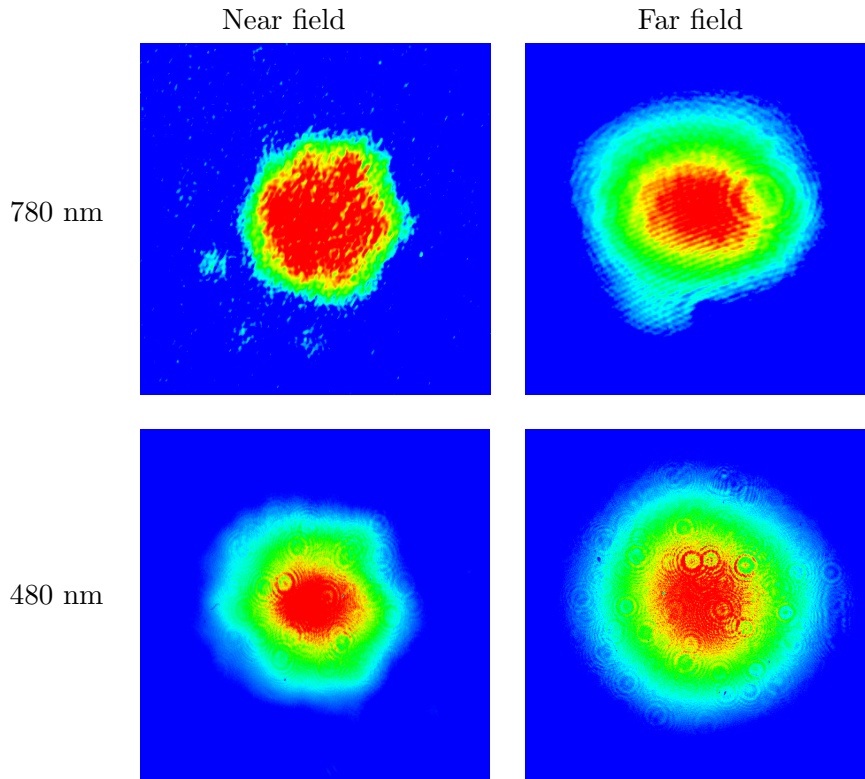

780 nm

480 nm

Figure 3.8.: Near-field and far-field intensity profile for different wavelengths.

mode overlap is achieved. visual verification of the far field images also confirms the coupling quality.
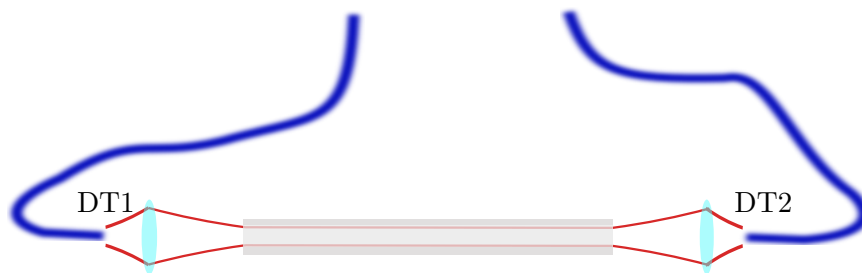

Figure 3.9.: Dipole trap beams mode overlapping.

3.6. Atom-HC fiber interface

To guide cold atoms into hollow-core fibers, dipolar forces are utilized. Cold atoms are trapped in MOT and further cooled and positioned in front of the hollow-core fiber

as sketched in the figure 3.10. A dipole trap beam passing through the hollow-core fiber overlaps with the atomic cloud. The initial trapping potential for the atoms are lowered down while increasing the dipole beam intensity. This results in transfer of atoms into the dipole beam intensity maxima. The untrapped atoms disperse away due to both, gravity and thermal velocity distribution. As it is evident the intensity of the dipole beam increases towards the fiber tip as the confinement gets narrower. Hence, the atoms naturally follow towards the fiber tip as shown in figure 3.10. These atoms keep going further and further inside the fiber as the potential is favoured for the atoms. This way a controlled radial confinement is realized to fill the fiber. However, in order to study the atom transport process as well as how light propagates through such extended cloud, axial control additionally would be an immediate requirement.
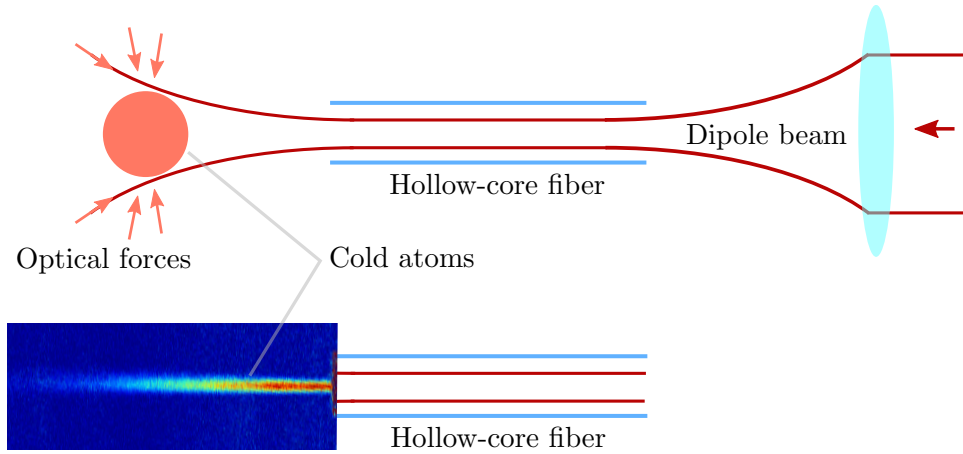

Figure 3.10.: Atoms trapped in dipole trap moving toward hollow-core fiber. Absorption image of cloud with fiber end is overlaid with sketch.

As discussed in the previous section, in order to control the atoms along the fiber axis, another dipole beam is overlapped through the fiber from the counter-propagating direction. This is to realize an optical lattice through the fiber is sketched in figure 3.11. At this stage the atoms get trapped in the extended optical lattice sites.
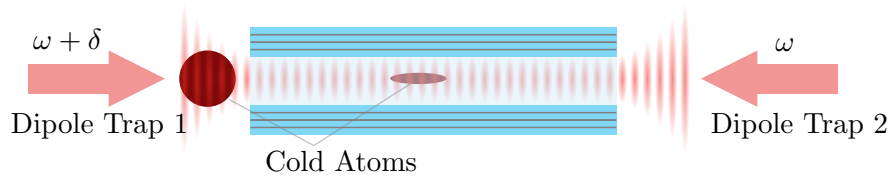

Figure 3.11.: Atoms in optical lattice.

By controlling the detuning of either of the laser beams, the trapped atoms can precisely be moved with a desired speed which is obtained by the equation[ref]. The

relative detuning of the two lasers are controlled by FPGA controlled DDS solution [ref]. These RF sources drive two separate AOMs through which the dipole beams are passing as shown in figure 3.12. The tuneable Ti:Sapphire laser is original source of the 810 nm. By tuning the absolute frequency, the trap depth and scattering rates can be adjusted which follows the equation[ref]. The source laser beam is seeded to the two separate thermally stabilized tapered amplifiers (TA). The output beam passes through optical isolators and beam shaping optics through two separate AOMs. The frequency of the AOMs are controlled by a DDS synthesizer synchronized to a single clock source. The frequency of the two AOMs are adjusted independently to high precision which provides a high degree of control over the atomic position. Additionally, the RF amplitude of the AOMs can be adjusted to control the trap depth of the trap. Using TTL controlled switches, the output power is enabled or disabled at very high speed that has significant importance for the detection procedure which is discussed in the next chapter.
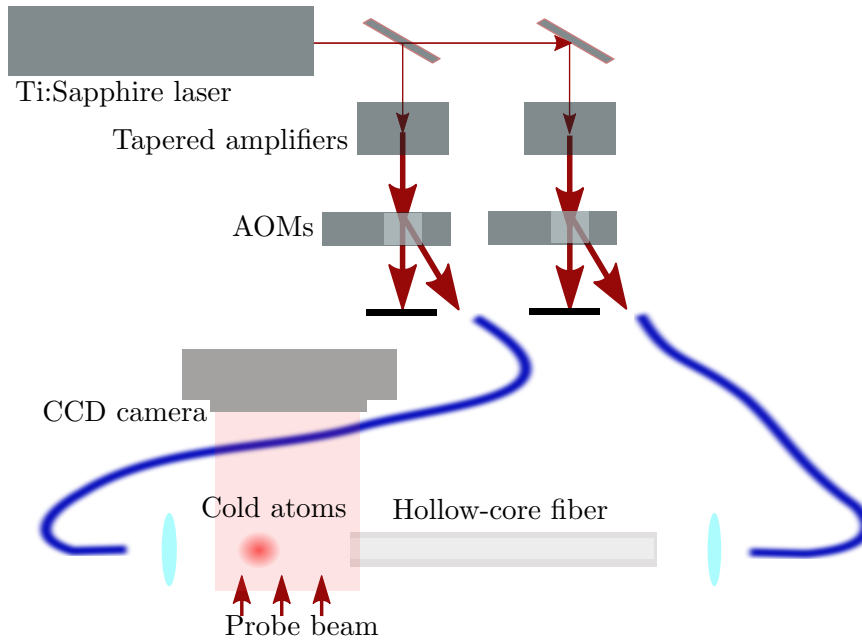

Figure 3.12.: Dipole laser schematics. Ti:Sapphire laser produces tunable wavelengths which is then amplified using TAs.

With the experimental setting shown in the figure 3.12, the optical lattice through hollow-core fiber is realized.

In the figures 3.13, the absorption images of atoms reaching the HC fiber tip is presented. Here, by setting the detuning, the atoms are set into motion. The detuning is reversed back to halt the atom at a desired location. The cloud is detected along the transverse axis using the absorption imaging to obtain the position, number of atoms and the temperature. For the controlled parameter space, the transport efficiency of above 70 % has been achieved. Temperature of the atoms stay below 300 μK

with a lifetime above 500 ms. Once the atoms are transported inside the fiber, the usual detection scheme fails to work. This leads to establish an independent detection scheme using a weak probe beam passing through the HC fiber and is a part of separate discussion for complexity involved with beam propagation. The experiment and a theoretical model is discussed in the chapter 6.
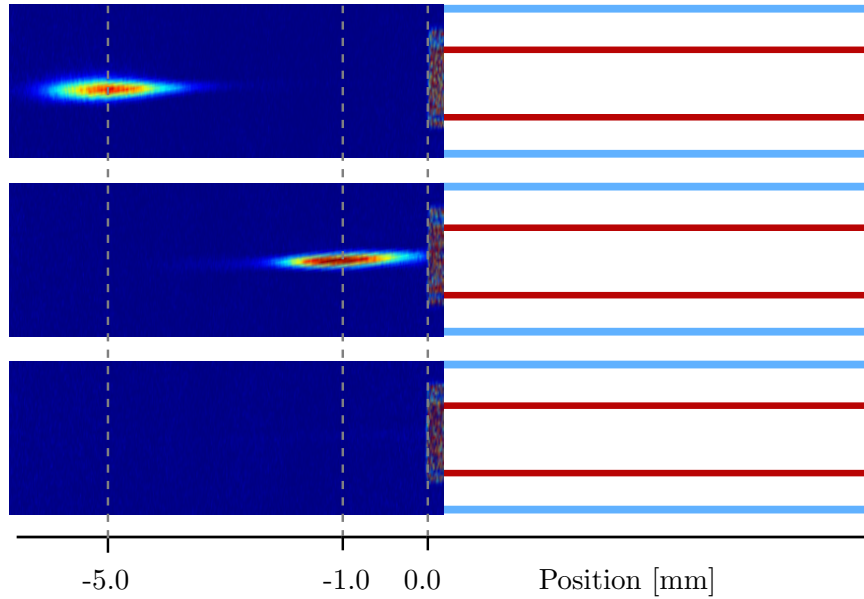

Figure 3.13.: Atoms trapped in optical lattice and moved towards fiber tip.

This high degree of control over the atomic position establishes the quasi-one dimensional confinement for cold atoms. The results from the experimental achievement serves as a playground for creating strong light-matter interaction.

4. Experimental techniques: control and detection

Experiments in atomic physics typically require high precision and stable timing controls. The stringent requirements are demanded by the time scales associated with the various experimental parameters such as coherence lifetime, atom-loss or spin relaxation times, etc. In this chapter, the system for the high precision experimental controls and detection relevant for this project are discussed. The main principle relies on the precision time pattern generation referenced to a single stable clock. This is achieved by using a hardware timed digital solution to control a sequence of signals, eg. laser pulses, ramp trigger, etc. Consequently, additional synchronized triggers are produced to mark and store data only for the interesting time windows. The high speed pulse pattern generator used for this project eventually is integrated with the existing 'slow' experiment controller along with the software interface.

4.1. Pulse pattern generator

The precision experiments performed in Chapter 5 required high-precision timed control pulses as shown in Figure 4.5. In such experimental control and measurement, time scales ranging from nanoseconds to several seconds are desired. To meet such requirements, hardware timed, stable clock based signal pattern generators and fast oscilloscopes are used. Certain dedicated hardware devices are typically interfaced with a central processing unit (CPU) for control and user access. Although, CPUs run at very high clock speed and are utilized for such time demanding experiments, they themselves lack the generation of precision timing sequence because of the the way the core architecture functions. Hardware timed devices such as Application Specific ICs (ASICs), Field Programmable Gate Arrays (FPGAs) are the natural choice for such experimental controls. While ASICs are capable of handing and producing signal at frequencies over several GHz, they lack the reconfigurability and therefore the versatility is limited. Moreover, the time to implement for a general application is much longer which limits its practicality. For the context of the experiment in this thesis, FPGAs are fast enough to produce all the relevant control signals. In this work, a Xilinx FPGA (Spartan-6) based high precision-timed sequence generator is implemented which then is integrated with the main experiment controller hardware to facilitate high speed measurements. In the Figure 4.1 a visual implementation of the sequence generator is depicted. Here, the sequence pattern data is captured from the user input using a GUI on the computer. The data is pushed via USB port to the FPGA internal memory. Specific USB communication devices are used for this

purpose. The treatment of the user data is configured in the FPGA using HDL codes which are presented in the appendix. The IO part of the hardware is interfaced to drive the AOMs, switches and triggers. The sequence pattern is generated in sync with the external trigger input. In this experiment, the trigger is given from the main experiment controller. The precision experiment section is then handled by the FPGA sequence generator.
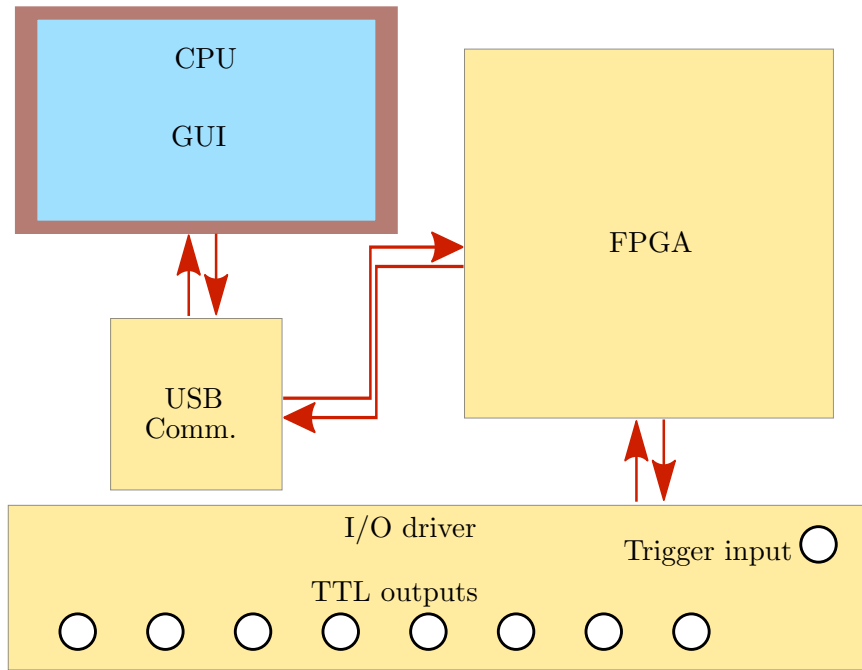

Figure 4.1.: Schematic of working principle of USB-FPGA interface for the pulse generator. Pulse-pattern is stored on the FPGA memory via USB communication. External trigger enables the output on demand.

4.1.1. FPGA

As the name suggests, an FPGA primarily consists of three types of functional components– logic block, IO block and interconnects shown in the Figure 4.2. The logic block consists of millions of basic logic cells such as flip-flops, selectors, comparator, etc. whose task is to perform primitive gate operations. The IO block comprises of transistors and registers for driving and storing the input and output state. This block interfaces with the outside world with various types of signals, such as TTL (single), LVDS (differential), etc for clock or data operation. The two blocks are interlinked with a large number of wires which can be configured to route the signal in a number of ways. Such routing is made possible by the interconnects which make an FPGA a platform for reconfiguration in field operation. This reconfigurability is what gives an FPGA the main power in the domain of digital electronics. It stands clearly

away from microprocessors and microcontrollers in the sense that the logic 'wiring' in the later ones are hard burnt making them only suitable for specific application. Furthermore, even single logic operation undergoes a series of events making them unreliable for time critical applications. In contrast, the functionality of an FPGA can be thought of as real hardware logic units operating all in parallel. Such challenges are met by the interconnect which can be configured to trigger in sync with a single global clock input. On a side note, the clock rate of an FPGA only ranges upto several 100s MHz which is much smaller than modern CPU clocks which have surpassed 5 GHz. Nevertheless, the capability of parallel processing provided by an FPGA can not be fulfilled by any CPU as CPUs work on sequential operations. However, the benefits an FPGA enjoys from the primitive logic architecture also poses certain limitations. For instance, any operation would require reconfiguration of a large number of logic cells in a specific structure. Additional difficulty comes from the actual human readable code as the structure of the code does not strictly follow a sequential manner due to the feasibility of parallel operations.

The clock line of an FPGA is distributed throughout internally throughout the IC with equal propagation time delays at each gate. Using SRAM based memories, different interconnects and logic cells are configured based on a given application. The programming software mainly translates the human written codes into a binary file which is stored inside the FPGA chip. The language is called hardware description language (HDL) for the obvious reasons. For this project the task included in the HDL code is to establish a communication protocol inside the FPGA which can read data transferred over USB-Serial device which is discussed in the next section. The data is then transferred to the internal memory, block RAM (BRAM) of the FPGA which can be read on demand. The configuration further defines the different IO pins for input or output as it is required for clock, trigger or output channels. One limitation lies with FPGAs as the internal memory is all based on SRAM type which looses once the device has no power. This means, the device needs to be reconfigured everytime it boots. For this purpose a flash memory also comes soldered on the development board where the configuration binary data is saved.
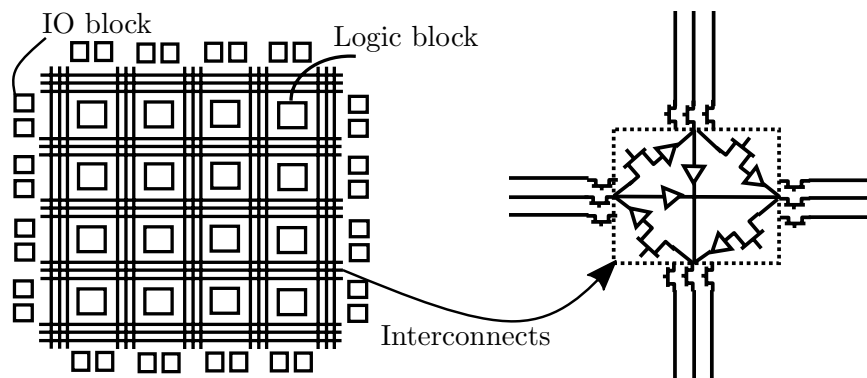

Figure 4.2.: Internal functioning of FPGA.

Once configured and data is loaded from the computer, the given pulse pattern can be generated on the multiple pins of the FPGA. The pulse generation events are triggered with an external event to maintain the synchronization with the main experiment.

4.1.2. USB-communication

USB being one of the most common ports in the modern computers offers an easy and universal solution for data transfer between a host and a client. For this project, a very simple USB UART protocol was used. As the need to the data was not too large, it worked mostly fluently for our purposes with distances larger than 15 meters. UART is an acronym for Universal Asynchronous Receive and Transmission. The data is send from the PC to the FPGA board with a fixed rated, also know as baudrate. In order to set a proper communication, the baudrate has to be known in advance as this kind of communication does not carry any additional clock. The data is broken and sent in packets, with each packet carrying 10 bits of those 8 are actually used as data, while the other 2 bits are overhead that is needed for the communication protocol. As shown in Figure 4.3, the idle state of signal on the Rx/Tx is high. Which after detecting the negative fall starts a trigger to sample data after predefined intervals. In this case, the data is sampled in the middle to avoid ambiguity. A dedicated device is used for converting USB to serial type data. The serial data is then interpreted and saved in the FPGA Memory which is discussed in the next chapter.
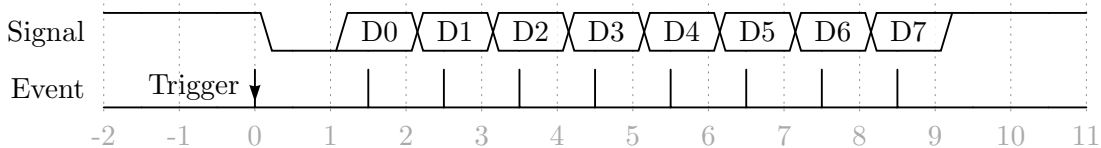

Figure 4.3.: Time diagram of UART communication protocol. Idle state of signal is high which is lowered at the beginning of communication. Data bits are sampled after a predetermined time period.

4.1.3. Control interface

The data received from the PC is stored in the BRAM. The FPGA outputs the data on the digital pinouts once it gets a trigger on the preconfigured input pin. The digital signal pattern and time information is stored in multiple words with each word length was equal to 108 bits. The first 48 bits controls the registers attached to the output pins, while the remaining 64 bits are used for interpreting time information. A typical GUI software interface is shown in the Figure 4.4. In this example interface, a 8 bit patter is generated with time resolution of 10 ns. Multiple loops of these patterns are realized by placing values on the right side, eg. num1 and num2. The loops are also independed to each other, meaning they can be operated in sequential

order or one loop inside other. Such flexibilities offer a number of possible output pulse pattern which are extremely important for control and measurements. The GUI program is written in Python and included in the Appendix.
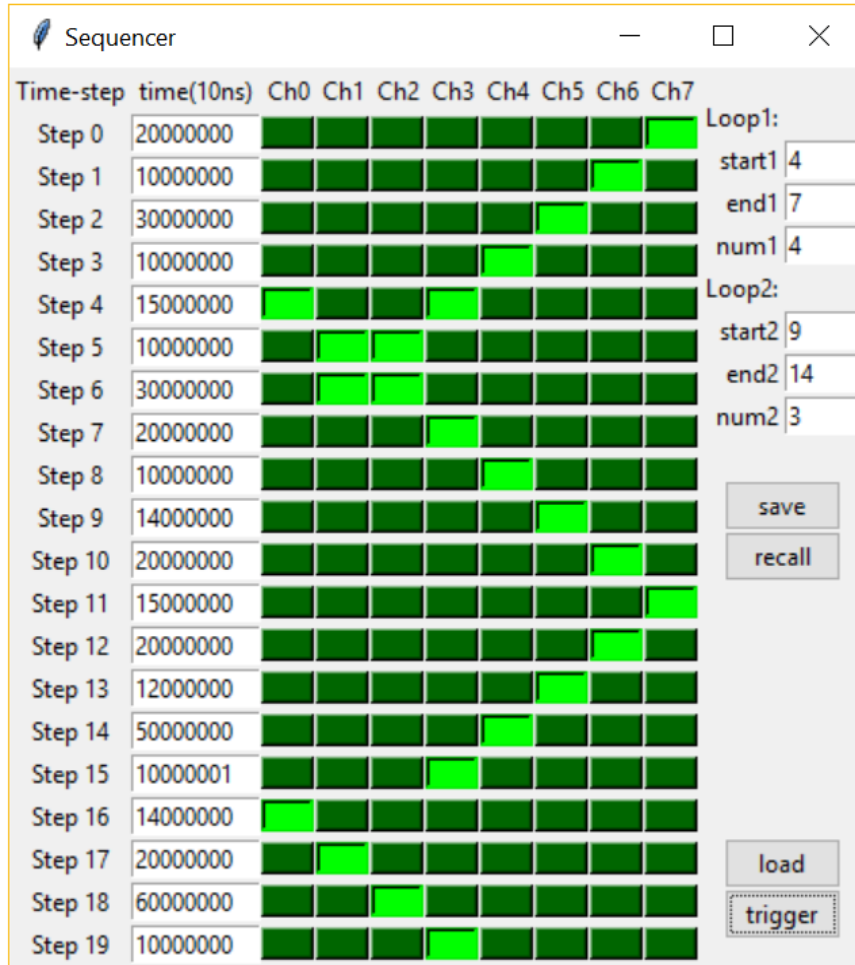

Figure 4.4.: Control software interface for FPGA pulse generator. The word pattern is stored using a GUI interface. Output pattern is generated via either software of external trigger.

4.1.4. Pulse generation and testing

In this section, the performance of the home-built pattern generator is presented. The device is capable of generating pulses as short as 10 ns and multiples of it for a duration of beyond several weeks which is way beyond one would need for the application si cold atom experiments. In the final stage, buffer line driver ICs were implemented for both, protection and high current driving capabilities. The PC side interface is based

on Labview. The in-build usb serial communication is used which transfers the used input data. The screenshot of the program looks like this. It has looping options for repeating certain step pattern for a large number of times. A typical pulse pattern is shown at high sampling rate in Figure 4.5. The different digital signals drive the two spectroscopy and the two dipole laser AOMs.
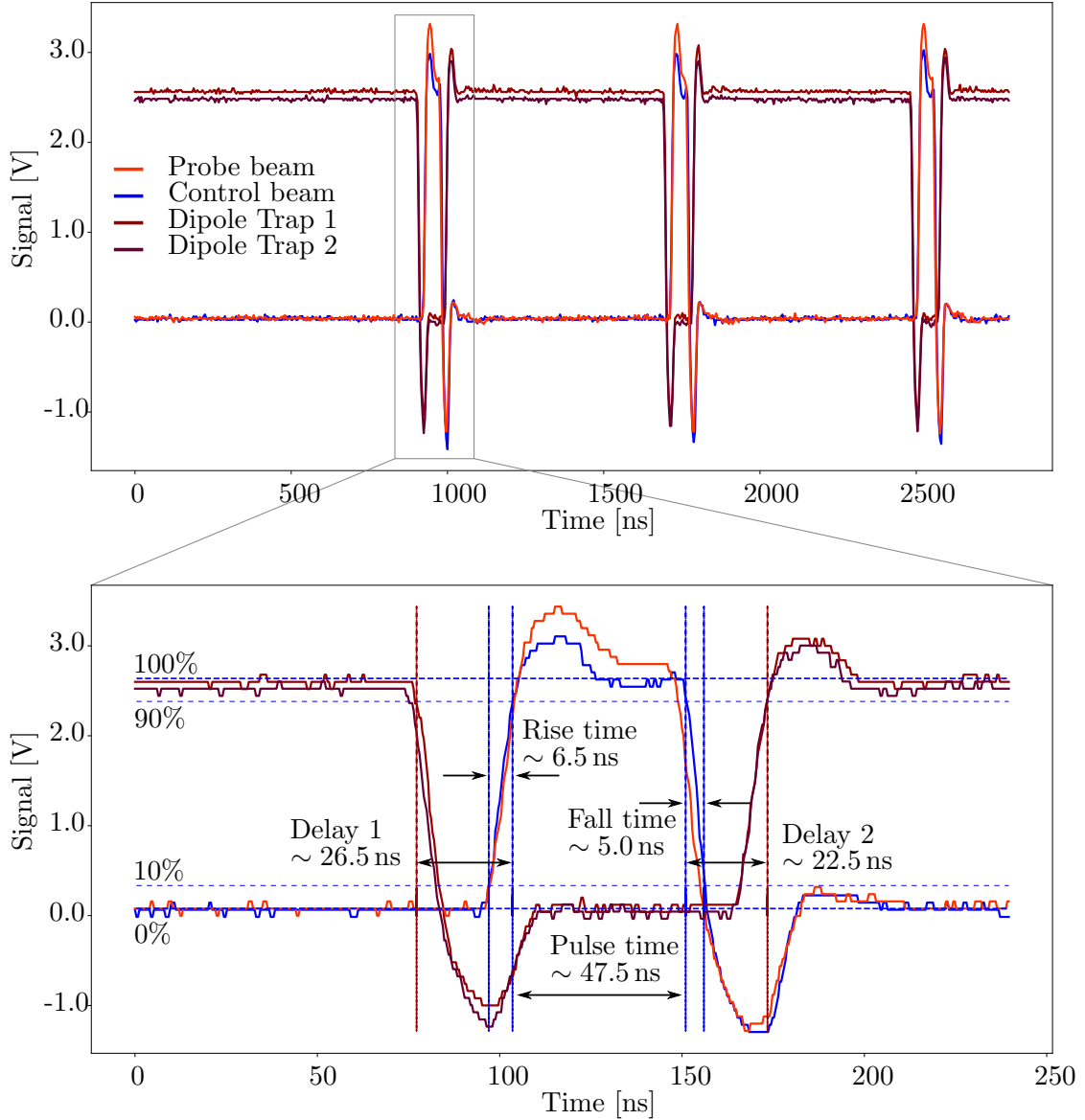

Figure 4.5.: Pulse durations for different channels. Delays were added between the probe/control and the lattices switch signals.

The temporal delays are adjusted accurately with 10 ns steps. In the shown trace, the two dipole trap lasers are turned off when the detection is made. In order to avoid

	Set timings	Measured timings
Delay 1	20 ns	26.5 ns
Pulse Time	50 ns	47.5 ns
Delay 2	20 ns	22.5 ns

Table 4.1.: Time diagram of signals for controlling various AOMs.

the overlap between the detection, additional delays are padded to the both side of the probe/control AOM signals. Considering the transmission/capacitive and length distortions, the signals are clearly separated. The rise time and the fall time ($10\% \leftrightarrow 90\%$) of the signals (shown for the blue trace) are well below 10 ns. The exact timings as sent from the PC are shown in the Table 4.1. All the high speed measurements in the project range sever 100's of ns. The ringing effects can be seen which is a trade-off with rise-time. However for our application, use of a proper termination solves the issues which was also confirmed by the actual laser pulse timings.

In conclusion, a simple and easy solution was implemented for a relatively high precision and time demanding performance. Satisfying outcomes were observed, some of them are presented here. The device was implemented in the experiment with a trigger input afterwards, the device takes control of both the dipole trap lasers and probe and control beams along with all the trigger outputs for the oscilloscope for data acquisition.

4.2. Detection and data processing

Pulsed signals are stored on high-speed oscilloscope (Lecroy waverunner xxx) for further analysis. The scope is capable of storing signals with segmented memory style to reduce the total data size while only storing the useful events. Data files are stored in hard drive which is shared with a local PC. The data is loaded in MATLAB or Python for analysis. A series of traces are taken which includes signals with atoms, without atoms and without probe beam to remove background noise and offsets.

To match the right timings, a trigger pulse is generated from the pulse generator to synchronize the detected probe beam pulses. Timing offsets are matched by observing the signal on the scope which appears due to lags in the different electronic stages for the probe beam AOM.

4.3. Laser stabilization

One of the most important parts of a cold-atom lab is a source of a highly stable laser beam. Such stringent requirement is needed for a wide range of applications such as laser cooling, manipulation of atomic states, spectroscopy, etc. There are different techniques developed to stabilize the laser frequency. In this work, we used reference line from atomic spectra to stabilize the laser to different states. To precisely modulate and control the frequency, we used AOMs. In this work, frequency of several
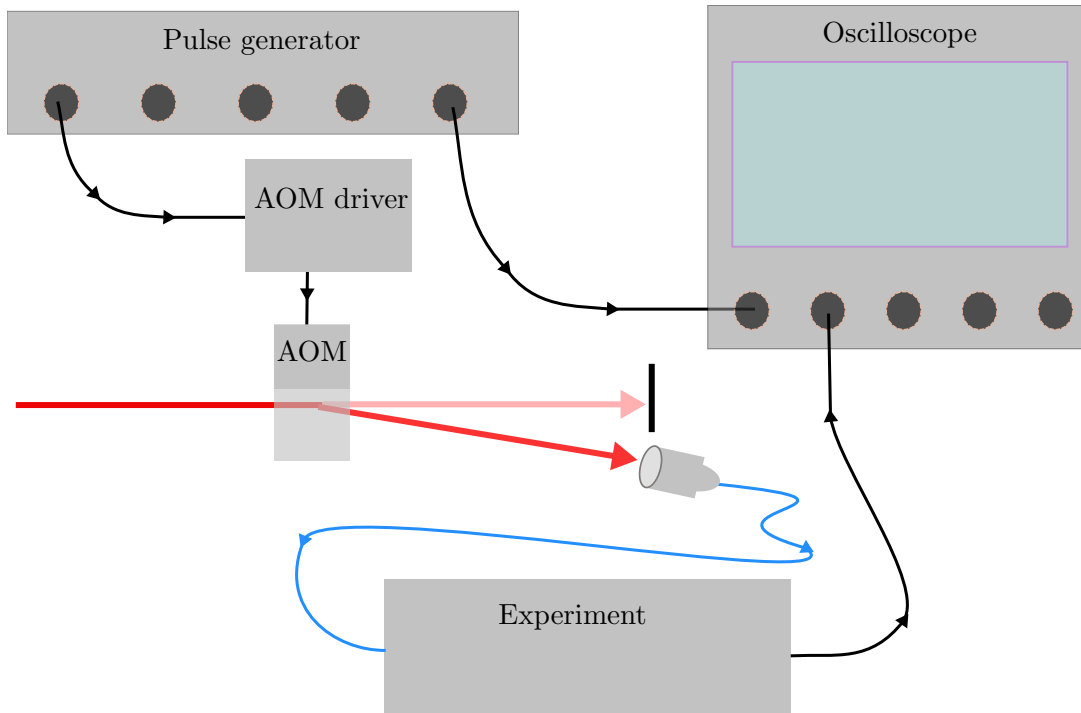
Figure 4.6.: General detection setup with trigger and AOMs signals driving the experiment and detected on fast Oscilloscope.

lasers were stabilized using frequency modulation (FM) spectroscopy technique. In this technique, the phase of a laser source is modulated which results in generation of sidebands. This beam is now scanned near the atomic transition and when demodulated using a Pound-Drever-Hall detection technique, it generates error signal which is fed back to the laser driver to stabilize the laser frequency.

4.3.1. Laser locking

Lasers are stabilized and locked to the relevant 2-level atomic transition line for laser cooling and detection. For our experiment, we use ^{87}Rb atomic vapour cell for stabilization. A near-resonant weak laser beam is passed through the cell which then is probed on to a photo detection. By scanning the laser detuning, the absorption signals are obtained which corresponds to multiple lines consisting of fine and hyperfine lines. However, a well known reason discussed earlier in Chapter 3, Doppler shifts due to atomic motion gives rise to significant broadening in the line shapes. Typically such line shapes are several 100s MHz broad which makes it difficult to address the hyperfine lines as they are separated by similar values. To circumvent these issues, Doppler-free saturation absorption spectroscopy is set up.

To obtain a Doppler free atomic, some part of the scanning laser beam is split up and
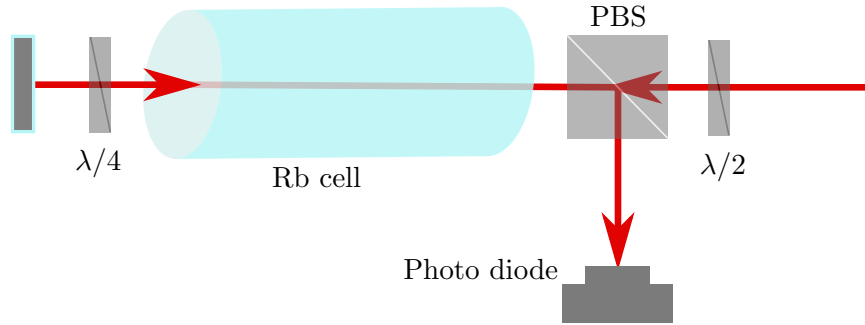
Figure 4.7.: Saturation absorption spectroscopy for laser locking.

sent from a counter propagating direction inside the Rb vapour cell. This results in velocity independent detection of atomic transition lines. Additionally, it also shows what are known as cross over lines which are even stronger than the constituent transition lines. These peaks are well related to the original lines.
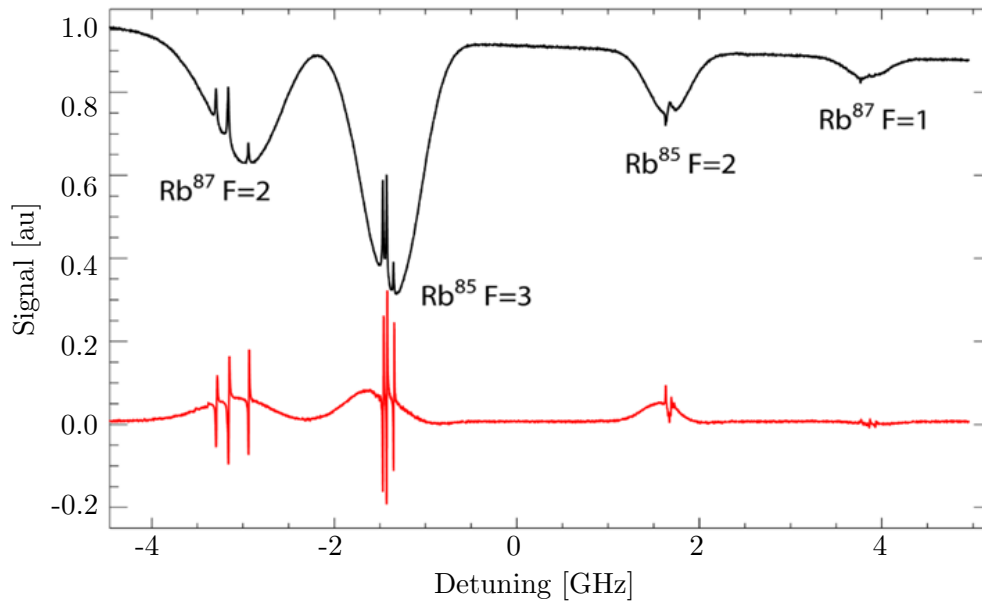
Figure 4.8.: Doppler free lines and error signal for laser locking.

Using the Pound-Drever-Hall detection scheme, the laser is stabilized to either of the transition lines. By adjusting the laser input frequency, by an AOM, the finally stable laser detuning is precisely controlled. Although this method has advantage of keeping the power constant while scanning the frequency, this lacks the speed and control at which the laser is modulated. Furthermore, it also lacks power controls. An AOM is placed after the stabilization stage to allow for power adjustment along with the frequency control. This method offers very high speed power and frequency

adjustment of the laser ranging up to 100s ns only.

4.3.2. EIT locking

Laser for addressing Rydberg states are stabilized using EIT-locking where error signal is generated by using a control laser in addition to the probe beam. In this scheme, a weak probe laser stabilized to the $F = 2 \rightarrow F' = 3$, using the previous method, is sent through a vapour cell. From the counter propagating direction, the control beam near a given Rydberg state transition line is scanned. As the laser scans, it creates a transmission signal, via the process already discussed, EIT. To stabilize the control laser frequency, again, an error signal is generated. This is achieved by frequency modulating the probe laser and demodulating using Pound-Drever-Hall technique. The error signal is now fed back to the control laser via a PID lock box. With a right selection of the parameters, the laser locking is engaged which then stabilized to the error signal.

The detuning of the control laser is controlled by either changing the reference probe
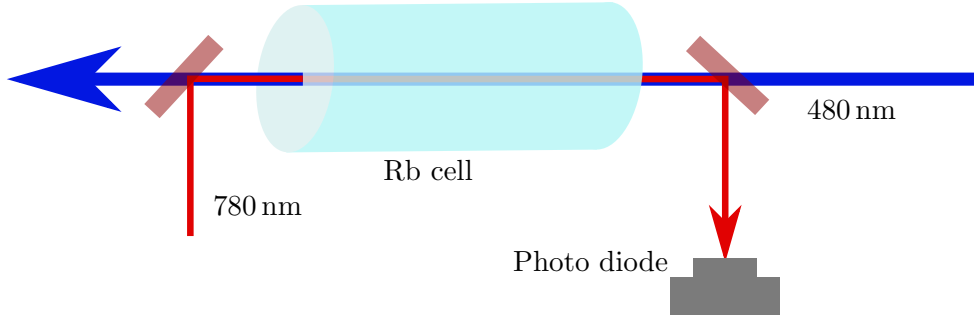
Figure 4.9.: Doppler free EIT locking scheme.

laser frequency or by using an AOM in the output of the control laser. As discussed earlier, there are trade-offs between the two methods and what is implemented depends on the particular requirements. However, it is important to note here that since the two laser wavelengths are not equal so the Doppler cancellation is completely achieved hence a clear understanding is required. Two-photon EIT signals are under off-resonant probe frequency require the understanding of the Doppler shifted detunings,

$$\delta_c = -k_c v, \tag{4.1}$$

$$\delta_p = k_p v, \tag{4.2}$$

where, at a given velocity of an atom, the control and probe detunings are δ_c and δ_p. For the thermal cloud, there is always abundance of atoms at velocities near zero. This is important to take it under consideration as the EIT lines are extremely two-photon detuning dependent. In that, the lines would be strong only if the two detunings are

matched and moreover, the probe laser is on resonance. For a given probe detuning Δ_p, a class atoms with velocity, v such that $\Delta_p + \delta_p = 0$. This results in

$$v = -\Delta_p/k_p. \tag{4.3}$$

Now, the same atoms would see the control laser at a detuning

$$\Delta_c = -k_c(-\Delta_p/k_p), \tag{4.4}$$
$$\Delta_c = -\Delta_p\lambda_p/\lambda_c. \tag{4.5}$$
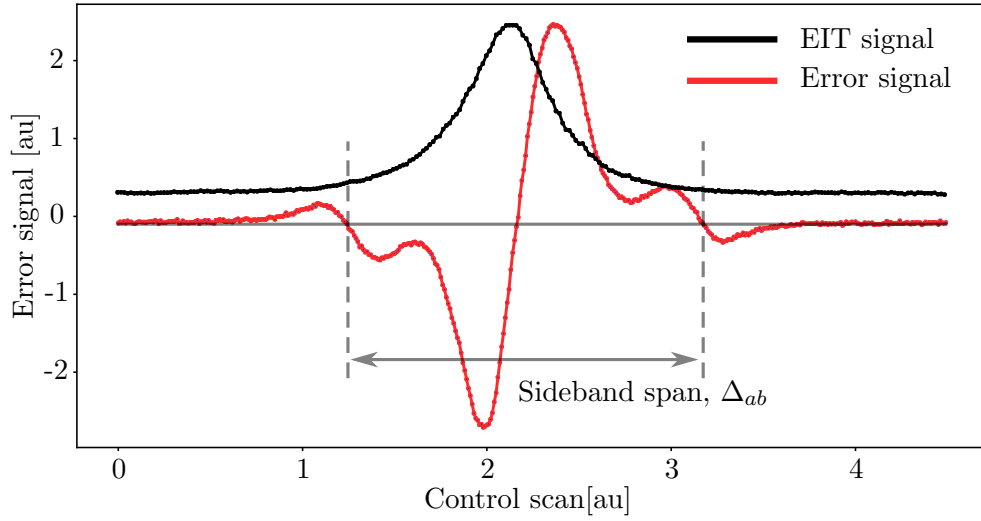
Figure 4.10.: Doppler free EIT locking scheme.

Using the sideband span, Δ_{sb} the axis is calibrated. The Δ_{sb} is obtained from the EOM frequency of driven by a function generator. In this experiment, the value of $\Delta_{sb} = 10.4\,\text{MHz}$. The observed span between the two cross points is

$$\Delta_{ab} = 2\Delta_{sb}\frac{\lambda_p}{\lambda_c}, \tag{4.6}$$

$$\Delta_{ab} = 2 * 10.4 * \frac{780}{480} = 33.8\,MHz \tag{4.7}$$

In simple words, the control laser detuning is set to the ratio of the wavelength of the two lasers times the detuning of the probe laser. In particular, with our laser configuration, the control frequency is adjusted by 1.625 times the detuning of the probe. This factor was taken into consideration in all the experiments performed and analyzed.

5. Rydberg excitation inside hollow core fibers

As has been discussed in the introduction and Chapter 3, atoms in the Rydberg states have drawn considerable attraction. On the one hand long-range interactions allow for a tunable control via the Rydberg states on the other hand longer lifetimes offer a range advantages for the practical usage. Combined with the quasi-one dimensional systems demonstrated by the hollow-core fiber interface, atoms excited to Rydberg states should propose another novel platform for quantum information processing or simulations. By tuning the blockade radius excitations the dimensionality can be tuned which has a range of features in the photon statistics aspects.

The task becomes challenging particularly considering the closeness of dielectric surface near the atomic ensemble. Such interfaces have known to show high electric fields which leads to shifts and broadening hence reducing the contrast of the EIT signals. With our approach, the first part of this chapter discusses the first Rydberg EIT signals with the cold atoms loaded inside the fiber. In the later part the characterization and measurements with another setup where room-temperature atoms are loaded inside hollow-core fiber are presented. The idea is to understand the influence of fiber inner core structures and coating of different materials.

5.1. Rydberg EIT with cold atoms

The idea is to realize a controllable system where atoms excited to Rydberg states form spatial correlation due to Rydberg blockade effects. This type of system has potential applications in understanding many-body photonic states, storage of quantum information and repeater. A handful of research has been performed in this direction ref. However, this work differs from others by two means – first, the extended long atom-light interface enhances the interaction strength and second, again due to the extended system, the accommodation of multiple excitations along the ensemble length would allow for interesting correlations. The photon storage and retrieval experiments have significant benefit from the cold atomic ensemble. This is due to the frozen atomic movements which reduces the decoherence processes as well as allow for longer interrogation times.

One of the ways to go about exciting atoms to Rydberg states is via EIT processes where two photons of matching wavelengths are projected to atomic sample. In this case, the EIT measurements are performed with the cold atoms transported inside the hollow-core fiber. The task itself is challenging due to the presence of the atoms

very close to silica surface. On such dielectric materials, charges are prone to attach and have known to create significant amount of field. These fields are highly undesirable as they produce lineshifts and broadeings in addition to facilitating ionization processes. In the following parts the experimental procedure and results are presented.

5.1.1. Experiment

Experimental sketch is shown in Figure 5.1. In the setup, a hollow-core fiber is placed horizontally inside the main UHV chamber. Cold atoms of ^{87}Rb is trapped in MOT in front of the fiber at a distance of about 5 mm. The guiding principle is discussed in the Chapter 3 where a pair of counter-propagating dipole trap beams are mode matched through the HC fiber. The control over the position of the atomic cloud has been demonstrated as shown in Figure 5.1. To address the Rydberg states, a probe beam at 780 nm and a control beam at 480 nm are overlapped in the counter propagating configuration using two photon processes as discussed in Chapter 2. These beams are also mode matched with the dipole beams in order to assure that the maximal coupling with atomic ensemble is achieved. As discussed earlier in the Chapter 3 the guiding properties for a range of wavelengths allow for such good overlaps. Using dichroic mirrors the probe beam is aligned and overlapped through the fiber. Consequently, the probe beam is deflected off and sent to a PMT for detection.
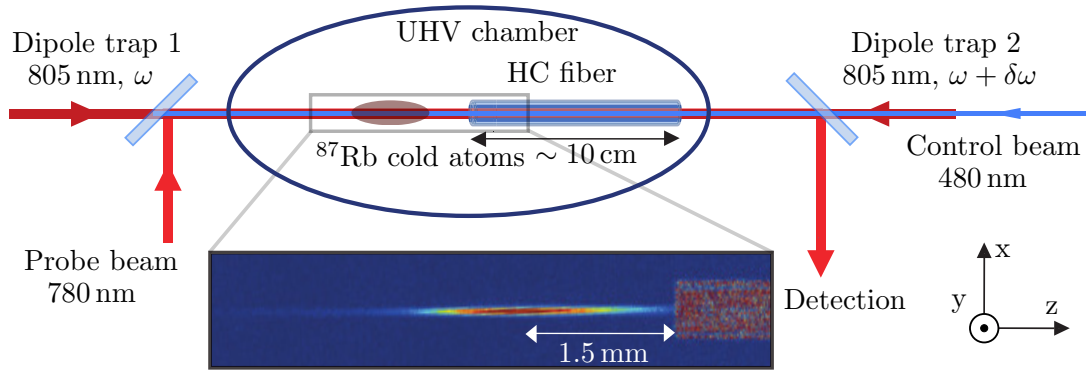
Figure 5.1.: Experiment setup for cold atoms Rydberg excitations. Inset shows a real image of atoms reaching the HC fiber.

5.1.2. Time resolved detection

The experimental control consists of loading MOT, transferring to optical lattice, transporting atoms to a desired position along the fiber length and finally detection. This section focuses on the details of detection schemes. Broadly, the detection process involves two photon excitation while avoiding the lightshifts produced by the trapping lasers. In order to do so, the lattice beams are turned off for a precise time interval. Probe and control beams are flashed within the given time interval and repeated

several times to obtain better statistics. The probe signals detected on PMT are stored on a fast Oscilloscope for further analysis. Two different schemes are implemented to detect and identify the EIT processes. In the first case, as shown in Figure 5.2 (inset (a)) the control and the probe beams are both turned on at the same time. By scanning probe detuning for each experimental run, the transmission profile is recorded.
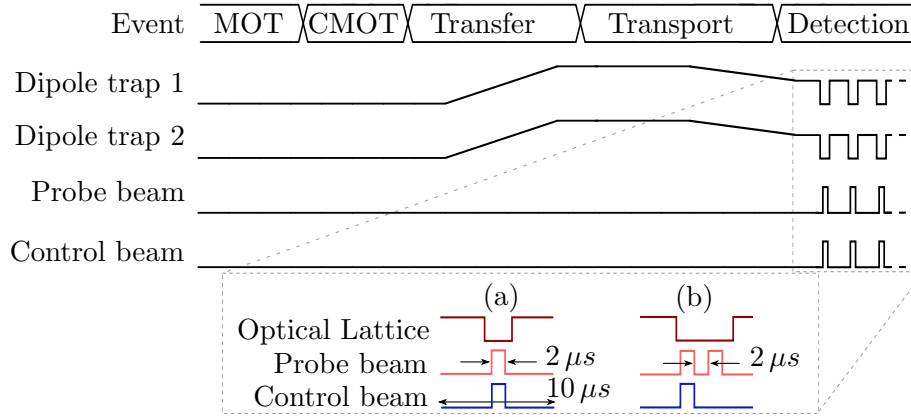

Figure 5.2.: Experiment time sequence. In the inset, dipole beams are turned off when the probe and control beams are sent. Two different schemes used to verify Rydberg EIT processes.

As the atoms are transported inside the fiber, the confining trapping potential keep the atoms away from the fiber wall. This is also important for spectroscopic reasons as the temperature still remains below few 100s μK. For such a narrow core size, the atoms as they are released can hit the fiber and will eventually be lost. The time scales are on the order of 100's μs. In order to detect these atoms while reducing noise level, a repeated measurements are made. The dipole trapping beam is responsible for inhomogeneous ac stark shift, hence while probing, dipole beams are turned off. Such a sequence follows a repeated on and off pattern as shown in the Figure 5.2 (a). When the probe pulses are turned on, simultaneously a trigger signal is sent to oscilloscope which stores the data in segmented mode to avoid unnecessary large amount of data. A comparison between outside and inside the fiber signal is shown in the Figure 5.3.

Cross section at pulse number 100 is plotted for the two data sets.
To verify the coherence processes and hence actual EIT signal, scheme using double probe pulses as shown in Figure 5.2 (b) is used. In this case, the first pulse, where the control beam is also enable should show typical EIT feature while the second pulse should monitor the optical density. In order to understand if the signals are not affected by other destructive mechanism such as hole-burning, the second pulse, i.e. the od data is utilized. In the Figure 5.5, the time resolved transmission signals are shown for outside and inside the fiber. The red zone shows actual transmission

Figure 5.3.: Full time resolved Rydberg EIT signal for inside and outside the fiber.
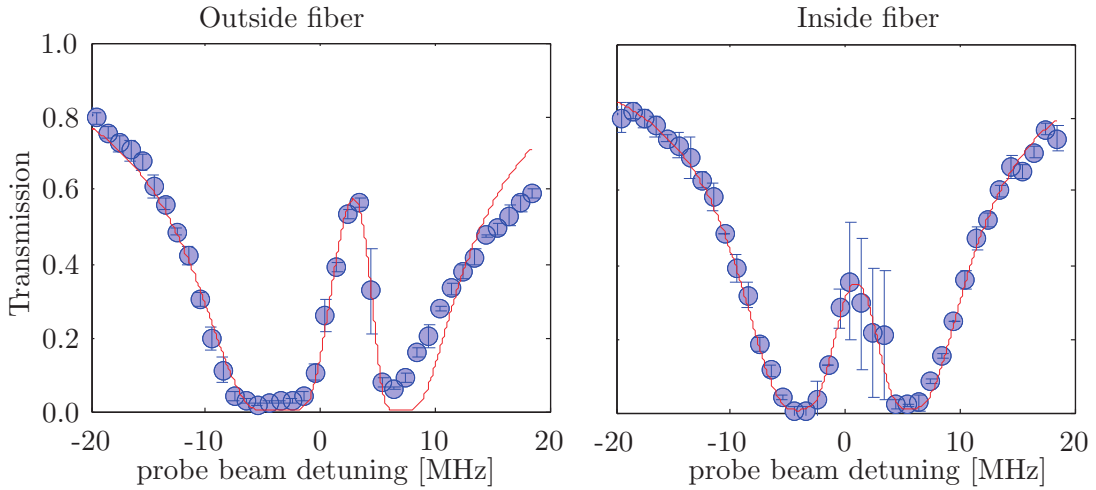
Figure 5.4.: Cross section at pulse number 100 Rydberg EIT signal for inside and
outside the fiber.

process governed by EIT mechanism.

The EIT and OD signals directly measured using double pulse technique are plotted for
different pulse numbers in the Figure 5.6. As is evident that initially, the EIT pulses
are showing clear distinction from the OD pulses which means that the conditions
required for EIT are met. At the later time, the OD signals and EIT signals merge
together, indicating hole-burning effects as result of atom loss or certain decoherence
processes. These results are also clear form the EIT-OD difference plots in Figure 5.5.

As hinted from the previous results where control laser is kept fixed and the probe laser
laser detuning is scanned, the shift in the Rydberg line results in an off-resonant EIT
process. A correction in the control laser detuning needs to be made in order the meet

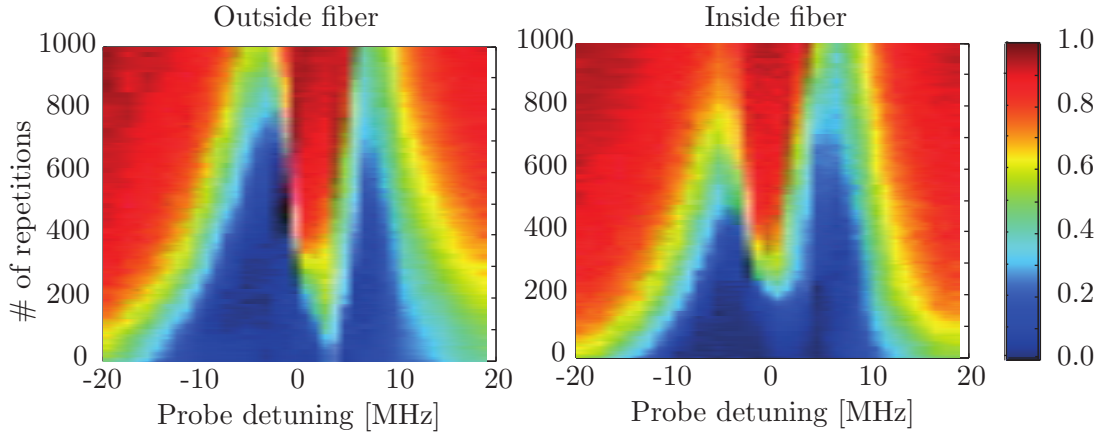Figure 5.5.: Cross section at pulse number 100 Rydberg EIT signal for inside and outside the fiber.
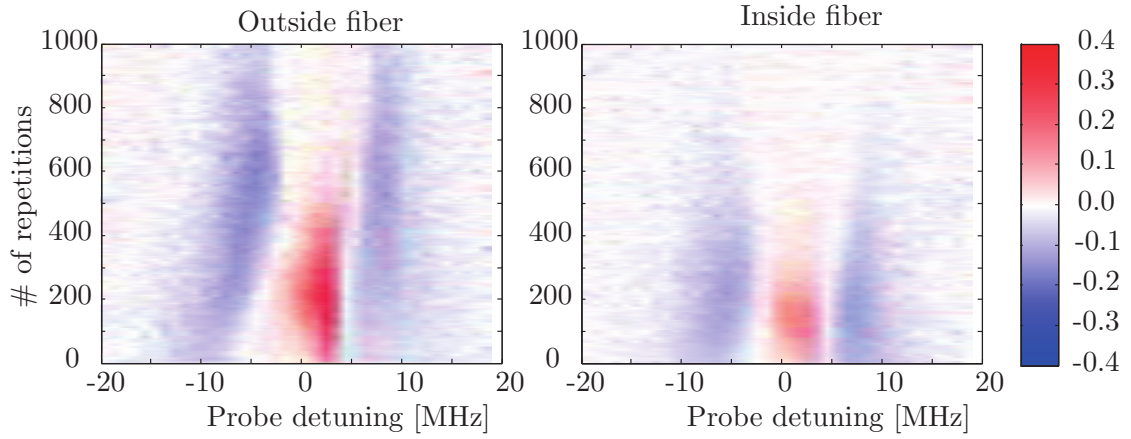

Figure 5.6.: Cross section at pulse number 100 Rydberg EIT signal for inside and outside the fiber.

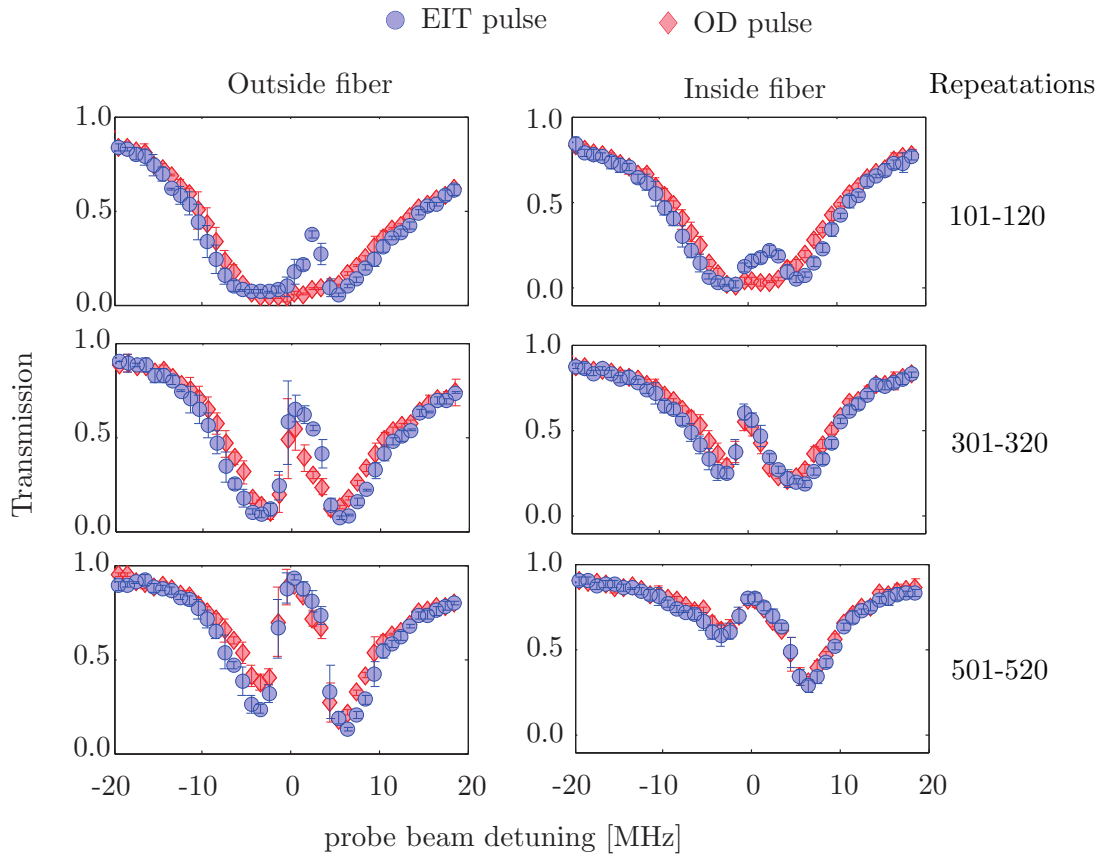the on-resonant condition. An alternate approach is to scan the control laser while keeping the probe detuning on-resonance. In this configuration, continuous detection of Rydberg EIT signals are made. For this scheme, the trapping beams were switched off first as shown in the figure 5.7.
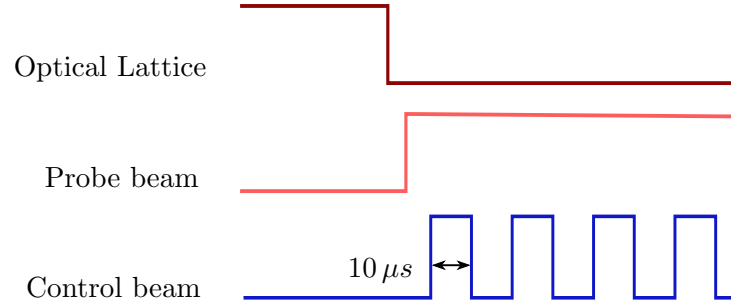
Figure 5.7.: Continuous detection scheme: Probe beam turned on shortly after switching off the optical lattice. The control beam is periodically pulsed.

Weak probe pulses were continuously sent through the expanding atoms and detected on PMT. To induce the EIT process, the control beam is flashed with a constant time interval. In the presence of the control beam, transmission window opens up which are visualized in the figure 5.8. Here, the signals from outside and the inside of the fibers are displayed. For comparison, continuous absorption traces are also plotted which is in good agreement with the signals when the control pulses of off. The ensemble becomes completely transparent for longer time due to all the atoms disperse from the region.
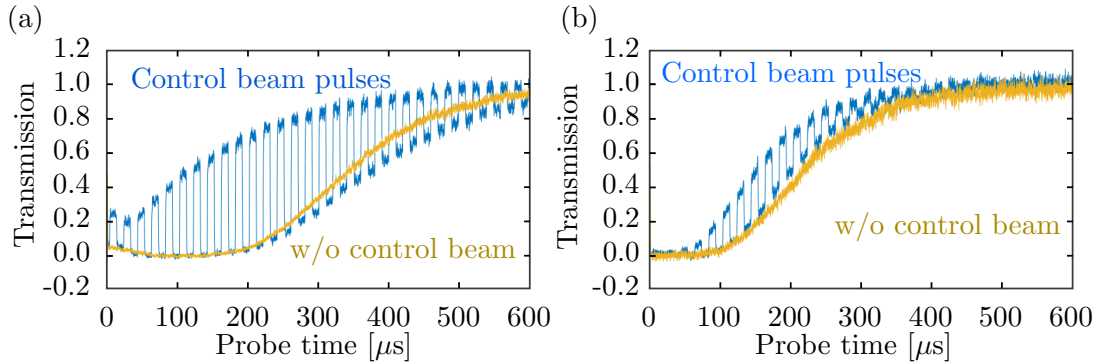
Figure 5.8.: EIT signals: Outside the fiber (a), inside the fiber (b). Resonant probe beam passes through atomic ensemble and is detected on the PMT. Periodic pulses of resonant control beam induces transmission.

To further confirm the transmission and analyze the spectral features, the control beam is scanned near the resonance frequency. To signify the transmission, a background corrected transmission signal is shown in the figure 5.9. Clearly, a peak in the spectrum confirms the process associated with EIT.

(a) (b)
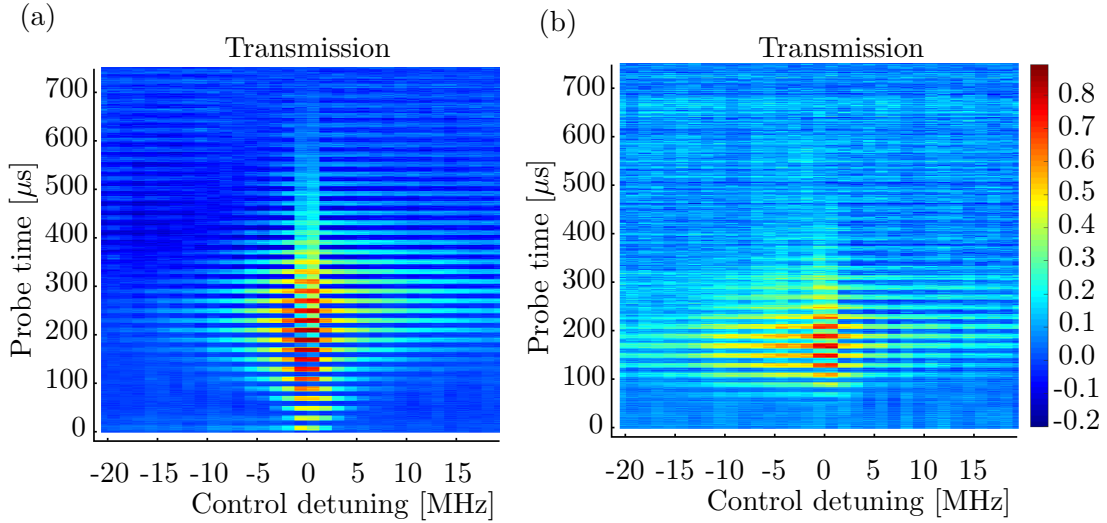
Figure 5.9.: EIT signals: Outside the fiber (a) and (c), inside the fiber (b) and (d). On resonance probe with control switches on and off (a) and (b). Transmission spectra for different detunings (c) and (d).

Additional effects of probe power is studied in order to avoid unwanted effects such hole-burning in the spectral feature. In this case, for the probe beam with $4\,\mathrm{nW}$ and $400\,\mathrm{pW}$ powers are used while keeping all the other parameters fixed. The beams correspond to intensity of $.25 I_{sat}$ and $0.25 I_{sat}$ where I_{sat} is saturation intensity. The spectral features are plotted in the figure 5.10. It is evident that on-resonance process undergo through a rapid change in transmission. This can be attributed to the loss of atoms from the region of interest. As it is discussed in the chapter 2, in the case with Rydberg EIT process, the steady state population of the atoms in the Rydberg state scales with the probe Rabi frequency. Therefore, for the higher probe powers the number of atoms going to Rydberg state would be higher and due to the relatively short lifetime, a decay channel opens up resulting in less transmission also known as hole burning.

Common to all the measurements, the low initial transmission needs a considerable attention. To investigate the properties, the control beam is switched on at different delays while leaving all the parameters fixed. The measurements results shown in the figure 5.11 suggests that the rise in the transmission signal at later time not a cumulative effect of the control beam. Instead, the thermal diffusion reduces the density over time, which inversely related to the transmission peak as well as the width of the EIT line.

5.1.3. Stark shift and electric field present inside fiber

On the one hand, the high sensitivity to electric fields brings the Rydberg physics to an interesting domain by exploring long range interactions while on the other hand presence of even weak stray electric field can cause undesirable shifts and broadening

Transmission

Transmission
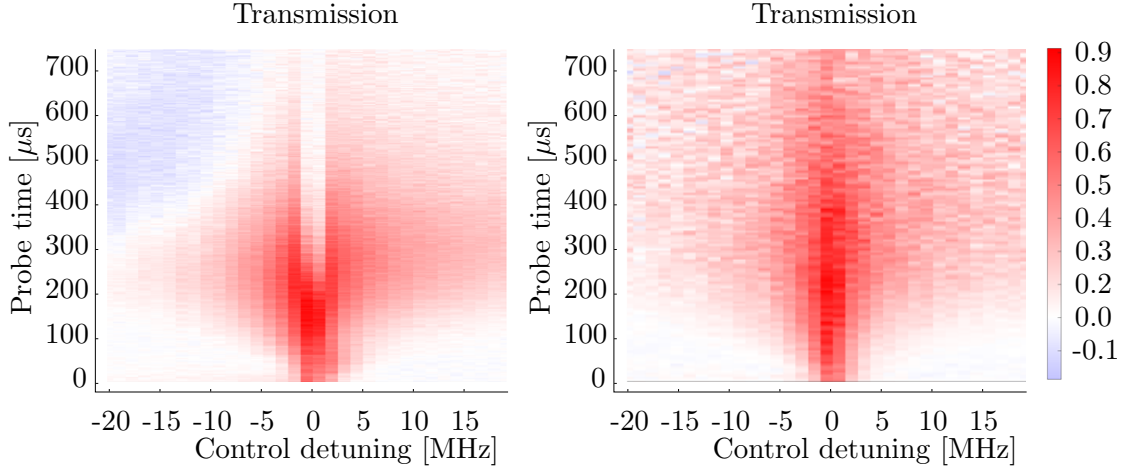
Figure 5.10.: EIT signals for two different intensities (a) $.025I_{sat}$ and $.25I_{sat}$.

Transmission
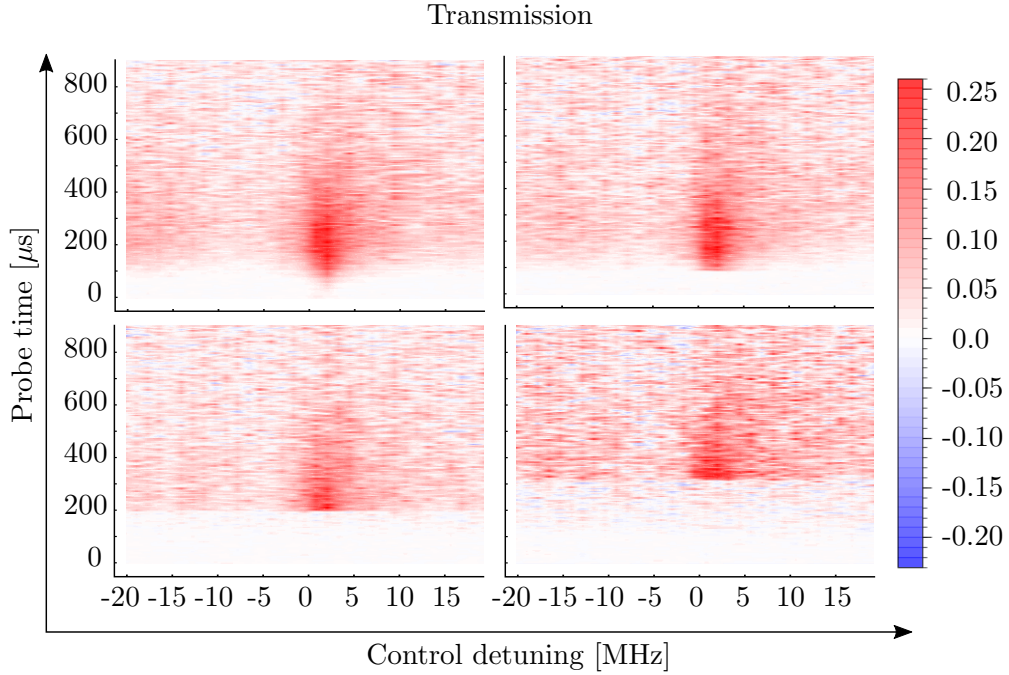
Figure 5.11.: EIT signals control beam turned on for dalays (a) $0\,\mu$s, (a) $100\,\mu$s, (a) $200\,\mu$s and (a) $300\,\mu$s. Measurements are performed for $26D_{5/2}$ state.

in EIT lines which could result in decoherence. In this experiment, atoms guided inside the fiber are exposed to fiber surfaces in a very close vicinity. Neutral atoms or ions sitting the fiber surface can produce significant electric field capable of shifting the Rydberg EIT lines. This was hinted in the previous measurements by observing the shift as the atoms are taken inside. To explore the nature and cause of the shift in more details, a set of measurements are made by selecting different Rydberg states.

By fitting a model obtained from Alkali atom line calculator, which predicts the lineshift as n^7 dependence as shown in Figure 5.13. A good agreement between the data and the model explains the origin of shift which is coming from electric fields. The estimated value of electric field is about $3.3\,\text{V/cm}$ which was also reported in previous experiment.
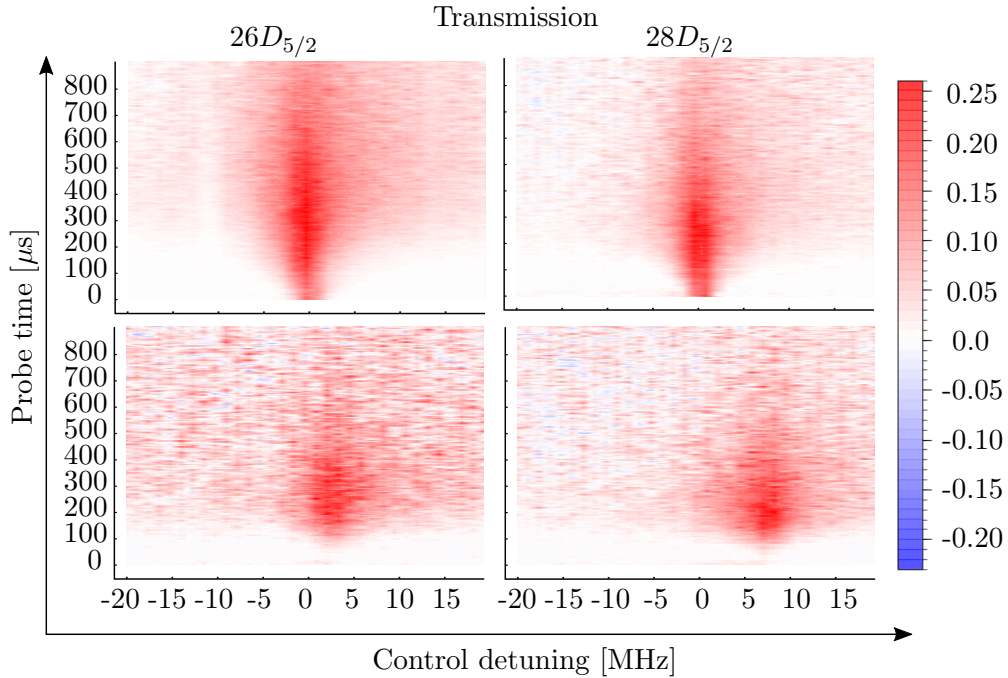
Figure 5.12.: Shift in EIT signals for $26D_{5/2}$ and $28D_{5/2}$ states.

5.2. Rydberg EIT with thermal atoms

Cold atoms physics have shown a range of advantage in measurements and simulations of quantum system. Primarily supported by its longer coherence times and preparation of pure states, there are have been a growing interest. However, all these features come with a price and that is resources and time needed to establish such a working system is highly demanding. Added to that, the actual measurement time is only a fraction of the sample preparation time which also sets a limitation to the number of measurements made in a given time interval. Although it lacks the ability, atoms at room temperature would an ideal choice for exploring features set by quantum physics. In this regard a set of measurements can still be made, of course with limitation yet capable of giving interesting outcomes.
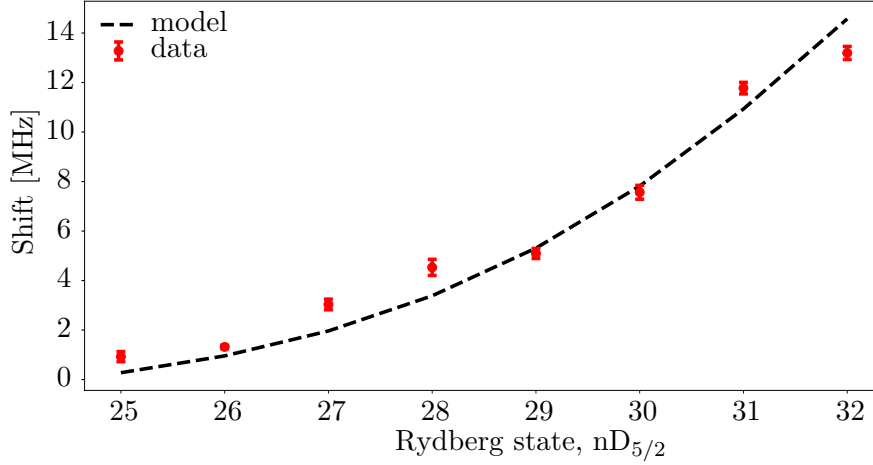
Figure 5.13.: Lineshift for different Rydberg states. Model maps the data to estimate electric field present.
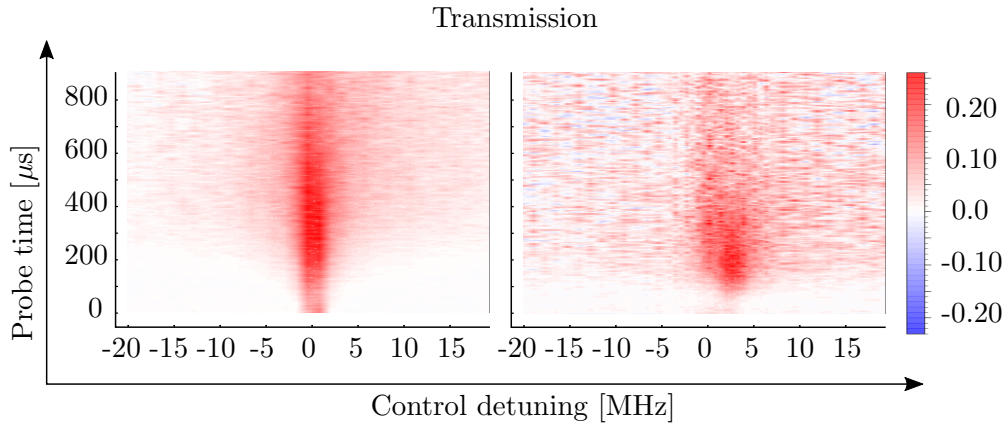
Figure 5.14.: Shift in EIT signals at MOT position and 14 mm away inside the fiber.

5.2.1. Experiment

The experimental setup consists of fibers placed inside a vacuum chamber shown in Figure 5.16. On the one end of the chamber, a glass ampoule of Rb is placed inside bellows attached to a gate valve. During initial pumping, the Rb atoms are isolated due to the glass ampoule. Once the sufficient vacuum level is reached, the ampoule is broken by bending the bellows. This increases the pressure inside the chamber as the gas inside the ampoule comes out. The turbo pumping system is kept operational which eventually pumps out the excess particles and the original vacuum level is reached. An ion pump is attached to the chamber to maintain the low pressure inside the chamber for stand-alone operation. The ion current is also calibrated to monitor the pressure inside the chamber. The gate valve is closed and the pumping-station is removed once the desired pressure is reached.
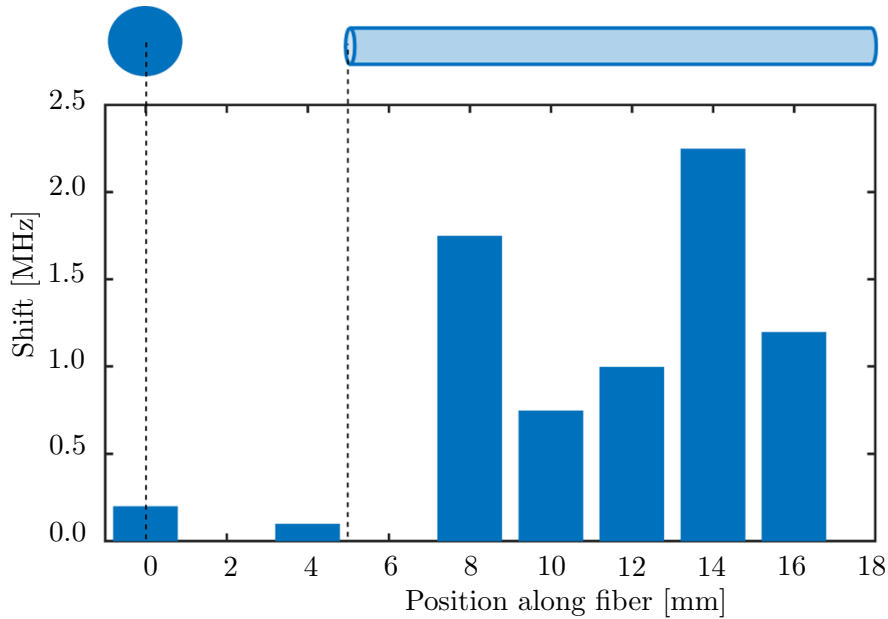
Figure 5.15.: Lineshift for different fiber position.

A heating tape with a temperature sensor is tied to the bellows to maintain a desired temperature. By adjust the temperature and the opening of the gate valve, the pressure and quantity of Rb inside the main chamber is controlled.
– Fiber cleaning procedure
By repeatedly filling the chamber with N_2 and repumping the chamber, it is speculated that the fiber is cleaned from inside. This process is illustrated in the Figure. Once the final pressure is reached, the ampoule is broken by bending the bellows. This releases gases that are filled in the ampoule which increases the pressure a little bit. Further pumping takes care of the additional increase. All these fibers are placed inside glass capillaries to avoid contacts and for labelling puposes.

Once the vacuum level below 10^{-7} Torr is achieved, the main pumping station is disconnected and the pressure is maintained just by the ion pump. Rb valve is opened and the ampoule container is heated. A near-resonant $780\,\mathrm{nm}$ laser beam is scanned to verify the presence of Rb atoms inside the chamber. Initially for several days no signs were detected which was presumably caused by the atoms sitting the inner walls of the chamber and various surfaces. Once the process was saturated, the sufficient absorption signal was clearly visible.

5.2.1.1. Light induced atom desorption (LIAD)

Rb atoms are known to bind with any surface by the process of adsorption. As a result, inside the fiber, there is a significant large surface area to volume ratio. This
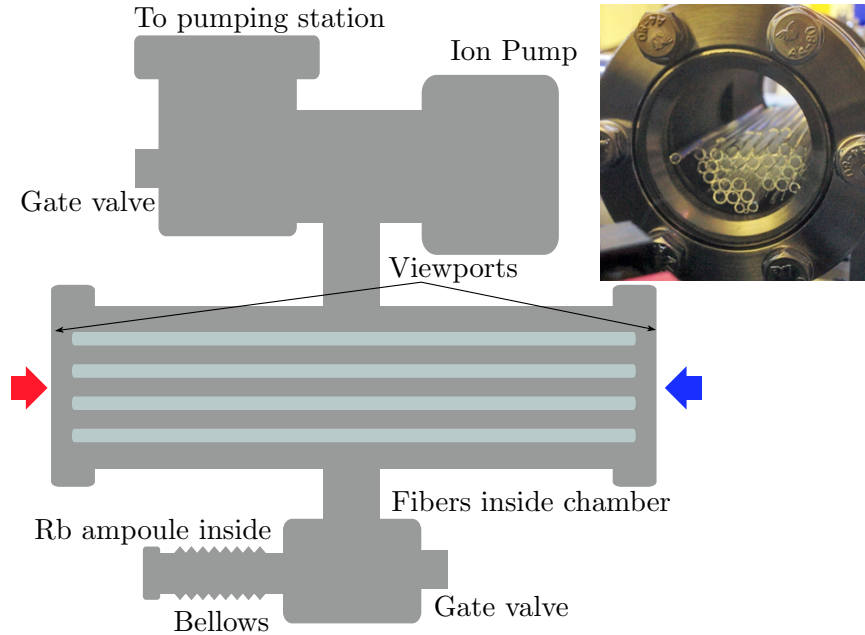
Figure 5.16.: Vacuum chamber for room temperature atom-fiber setup. Optical access are through the two viewports. Hollow-core fibers are placed inside the main chamber.

leads to a large number of atoms filling the fiber and sitting at the inner surface. By shining a light to this interface, atoms can be released by a process known as light induce atom desorption or LIAD. Much like photo-electric effects, the desorption rate further depends on the wavelength, i.e. for smaller wavelengths larger the atoms get released. In this project, the 480 nm laser is used to engage the desorption process as the effects are significantly larger as compared with 780 nm wavelength. The blue laser is slightly misaligned such that a large fraction of light beam propagates through the inner glass material.

In and ideal condition, the release of atoms from the surface is depicted in the Figure 5.18. Here, initially a high density of atoms are stuck at the fiber wall. After the launch of the blue beam, the atoms start to come out and eventually fill the fiber. This is where the density is maximum. At this moment, the pressure inside the fiber is way above than that of the vacuum chamber. This leads to outflux of the atoms from the fiber. This results in slow decay of OD over time. In the end, the total number of atoms inside the fiber decays down. After a period of a day, the loss is recovered by slow influx.

Although a perfect coupling into the glass material is not guaranteed by this method, a significantly large OD is detected as a result of desorption. For OD detection, the transmission signal of the weak probe beam is recorded. To avoid Rydberg EIT process, the blue laser is kept away from any transition lines. The peak OD appears immediately after shining the laser beam and starts to decay. The characteristic decay

Near-field profile　　　　　　HC fiber　　　　　　Coupling beam
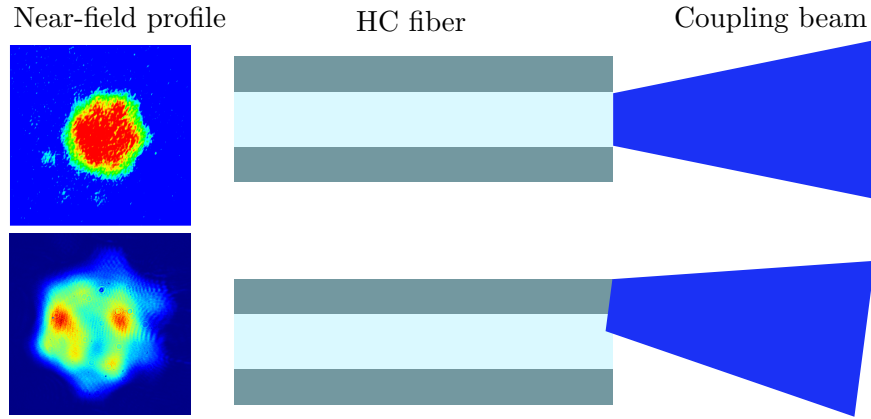
Figure 5.17.: Misalignment of blue beam for LIAD.

(a)　　　　　　(b)　　　　　　(c)　　　　　　(d)

(e)　　　　　　　　　　　　　(f)　　　　　(g)
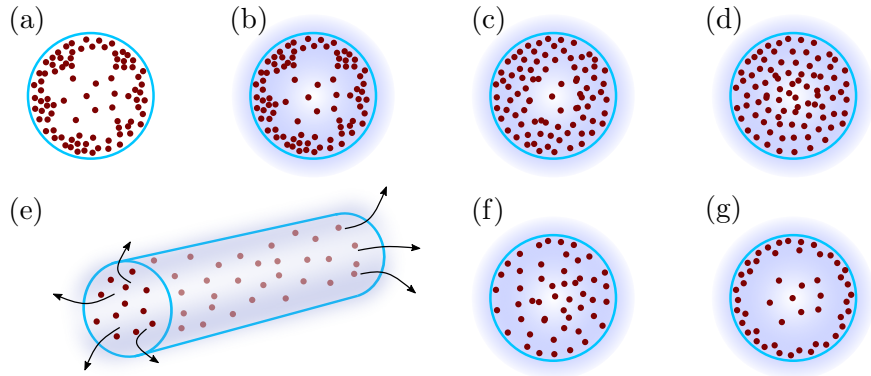
Figure 5.18.: Atoms inside HC fibers. The process of LIAD increases the atom density inside the fiber. (a) Atom distribution inside HC fiber, (b) to (d) with blue light turned on, pressure increases, (e) atoms come out of fiber, (f) and (g) density decreases inside the fiber.

time is on the order of several seconds.

Such adsorption processes have been known to introduce uncontrolled electric fields. The valence electron of the surface bound atom is attracted towards the Oxygen atoms present in the glass material. This in return creates a positive field near the Rb atoms pointing towards the fiber core.

5.2.2. Rydberg EIT inside fiber at room temperature

Obtaining Rydberg EIT signals at higher states has been challenging task which for various exciting properties. The implementation of room temperature setup is to study the processes that can affect the line shifts seen with the cold setup. Here, fibers with different core sized, geometries and coating were used to explore the interaction of Rydberg EIT processes. With scanning the control laser, the thermal background can
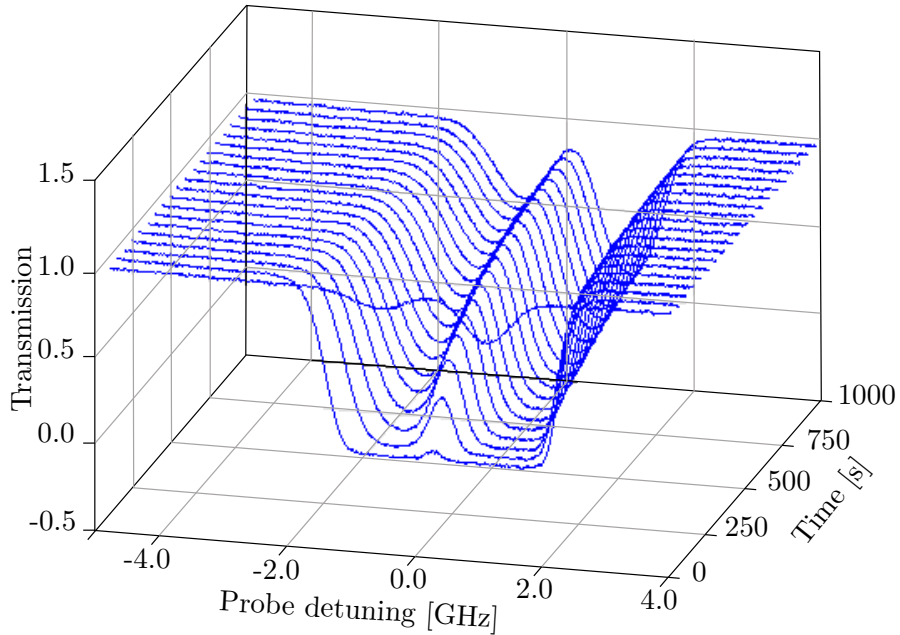
Figure 5.19.: Release of atoms inside HC fiber due to LIAD due to blue light.
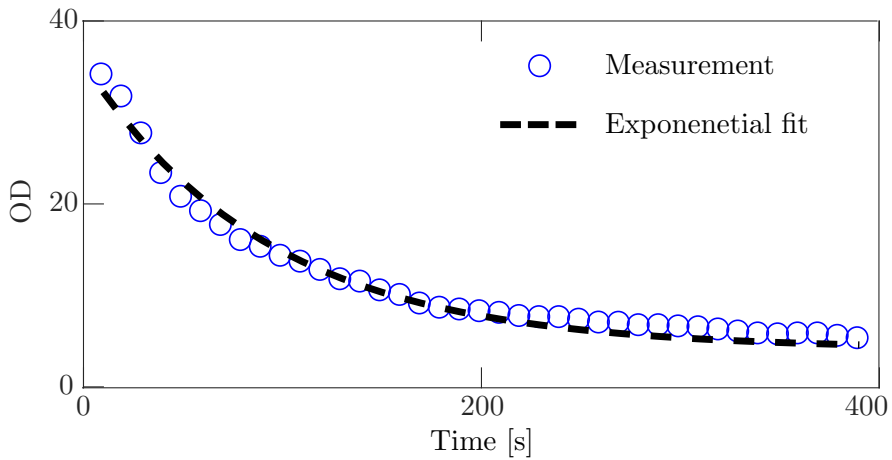
Figure 5.20.: OD with LIAD beam on.

be avoided and only the EIT lines would be detected. In the Figure 5.16, for probe laser fixed at resonance, the EIT signals are detected. This observation of EIT lines at very high states with only marginal shifts proposes several features, such as the overall fields present inside the fiber is somehow canceled. The idea is supported by the considering that the layer of atoms sitting inside can act as a metallic shielding. Hence, any charge produced inside can be shared inside making the central zone free of field in much like Faraday cage. Typically the Rydberg states are prone to shifts due to external fields, hence the EIT signal strength will become weaker if the lines

are far away due to off-resonant EIT process.

The Rydberg EIT lineshape is shown in the Figure. The EIT inside the fiber has a dramatically different shape as compared to the lineshape seen from the chamber signals. Transit time effects are included in order to best fit the lineshapes.
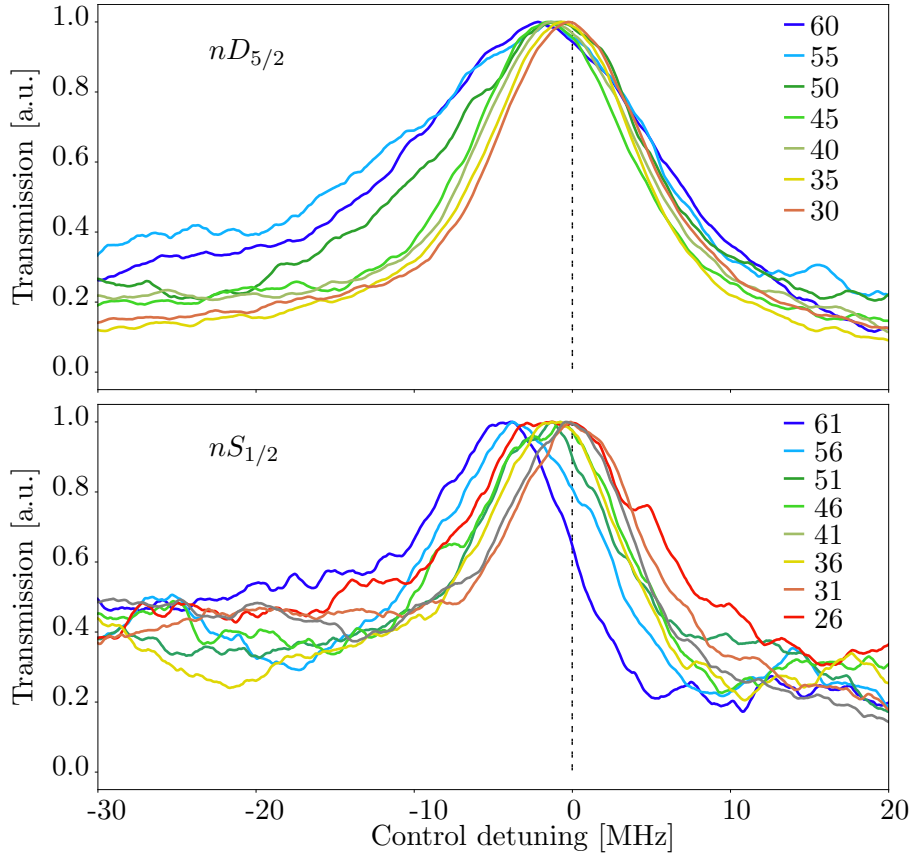
Figure 5.21.: Rydberg EIT for different n states shown by the legends. Promising results are confirmed from the insignificant shift.

In these measurements, EIT lines are recorded for different Rydberg states. These EIT lines, in contrast with the cold-atom setup can still be seen all the way upto 61 state. These results are remarkable and counter-intuitive as one would expect the cold-atom setup more "clean". The speculated reasoning here is that the fibers get all coated from inside by Rb atoms. This creates a shield which prevents any external field to shift or broaden the lineshapes. These results on hand hints at a possible way of performing high Rydberg state experiments in the cold-atom setup by utilizing fiber core coated with metalling materials.

Transit times are taken into consideration for the thermal vapour as for the given fiber core size, the atoms would only spend a time ~ 150 ns exposed in the laser beams. The short exposure eventually reflects limits the measurement accuracy as a result of line broadening. Nevertheless, experiments performed fast enough, such as storage

and retrieval of photons within few ns, can benefit from the simplicity of the setup as well as the implementation.

The exact lineshapes of the measured EIT signals inside the fiber required understadning of various parameters. For example, the narrow laser beam inside the fiber leads to transition of atoms in a time of 150 ns. The associated linewidth is about 4 MHz. Furthermore, the intensity of the probe beam is kept high in order to see any EIT signal which led to saturation broadening. The fit is obtained by numerically solving the optical Bloch's equation for non-negligible probe powers. To reduce the field sensitivity, the Rydberg excitation was chosen to 25D state. For reference, an EIT signal is simultaneously recorded from the chamber. The EIT lineshape is very well explained by the model here. However, the signal from the inside the fiber has significant deviation from the model. The possible reasons could come from how the probe beam propagates when it encounters an inhomogeneous optical path. In this case, the susceptibility due to the atoms inside the fiber is modified by the control beam which has a steep Gaussian shape. The details of such possibilities are discussed in the next chapter.

The Rydberg EIT measurements for different states have shown alteration in the transmission signal as presented in Figure 5.21. As, the exact mechanism for linewidth is not yet understood, the observation of the shift in the peak signal also carries certain useful information. A usual speculation is the shift could arise from electric field due to atoms or charge distribution inside the fiber. To analyse the lineshifts, S state signals are considered as the D state contains three sublevels which have different shifts associated with electric field. The shift is plotted in the Figure 5.23 with an overlay of simulated line due to polarizability calculated for the given states. Keeping the electric field as free parameter, the optimized fit results in the values of electric field for different fibers. It is remarkable to notice that the present field is much smaller than that in the fiber for the cold-atom setup. This has led to excitation of Rydberg EIT lines beyond $n = 60$ state. The speculations for the lack of stray field is due to the coating of the inner layer of the fiber with Rb atoms. As a result, any unbalanced field will be cancelled.

Another point to observe that the shift is not clearly dependent on the fiber or the coating as three of the fibers showed very small fields. The reason for relatively high field present in the 4th fiber is not clear yet but it could result from incomplete cancellation due to inhomogeneous layering of Rb atoms inside. Part of the reason can come from the inhomogeneous distribution of the blue beam on the inner surface of the fiber. As a result the redistribution of Rb atoms can only take place in certain regions.

5.2.3. Fiber core types and coating

The other purpose of this experiment is to verify the influence of core geometries or material coating which can affect Rydberg EIT lineshapes. To this end, 6 different types of fibers were used which each of them were either uncoated or coated with PDMS or Sol-Gel materials. These materials have proven to enhance spin relaxation
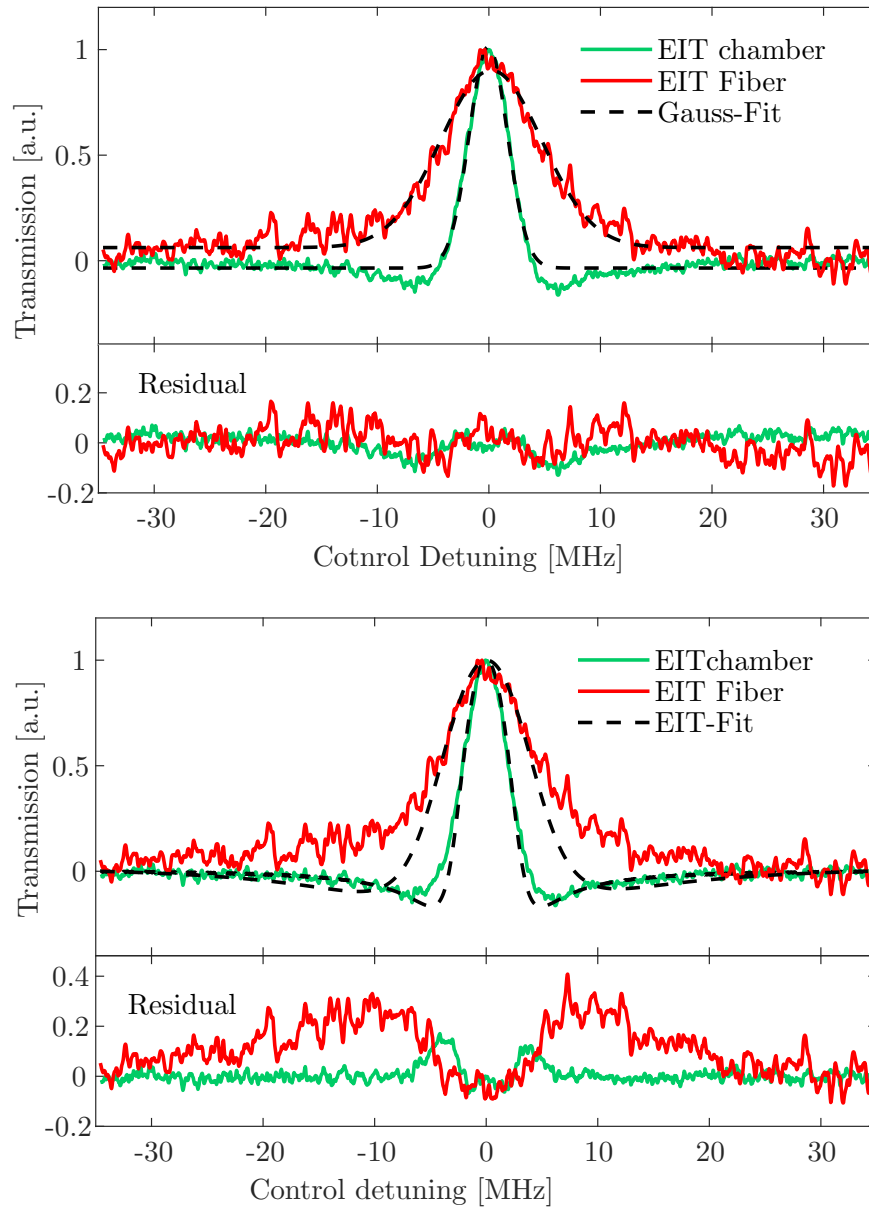
Figure 5.22.: Rydberg EIT lineshapes for signals from chamber and HC fiber. The EIT model for thermal vapour explains the chamber data while fiber data is not explained. The Gaussian model is reasonably close to the fiber data and is used for the study of peak position.

times with ground states atoms. The motivation was to explore how these coating affect the lineshapes associated with Rydberg states.

As with the previous case, the Rydberg EIT lineshapes were only marginally affected
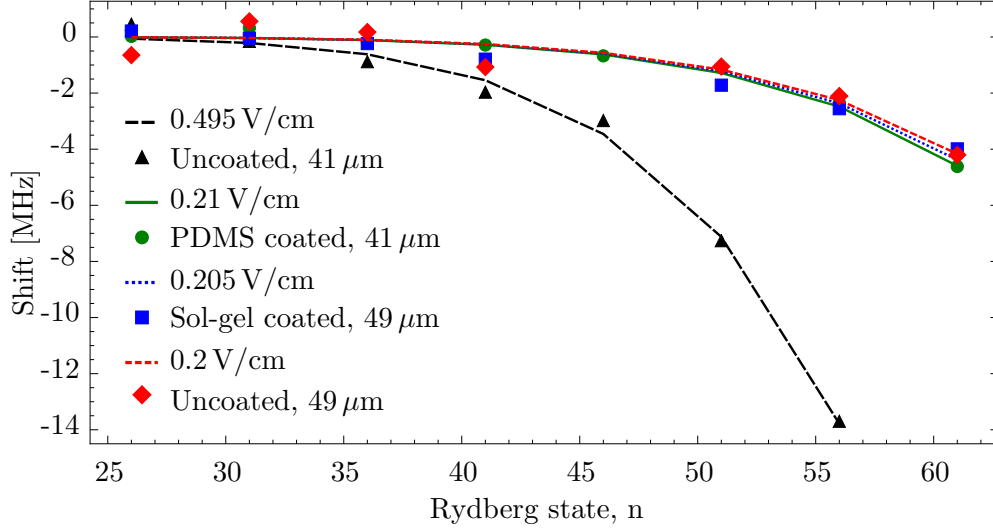
Figure 5.23.: Shift in EIT lines for different states for difference fibers shown by the markers. Fitting a model using stark shift for different states shown by the dashed lines. The predicted field is shown in the legend.

by the coating or the core structures. The dominant effects were governed by the transit time broadening.

As final words, the confirmation of Rydberg EIT signals has set up the platform required for a fiber based light-matter interface. The difficulty of Rydberg excitation near surfaces as found in various research have shown seemingly impossible task. However, in such experiments, flat surfaces were chosen which had shown very high electric field. Here, however, utilizing the closed surface which leads to formation of Faraday cage. This naturally favours the field cancellation. Furthermore, the field inside the room temperature setup had added advantage of relatively thick layer of Rb coating inside which acts as a metallic layer. The observation of reduced Fields has immediate consequence of excitation of higher Rydberg states. The results forward the research towards achieving storage of quantum information and generation of non-classical photons.

6. Beam propagation and detection

The experimental setup discussed in Chapter 5 features a novel technique for creating strong light-matter coupling. Here, such coupling is explored by the geometrical confinement between the atomic and optical overlaps. On the one hand, the precision control over the axial direction allows for positioning the cloud accurately at any location along the fiber direction, on the other hand, the radial confinement allows for a control over the coupling of light and matter by tuning the spatial overlap. An ensemble of atomic cloud strongly modifies a probe beam specially when it is tuned near the resonance. In a semi-classical treatment, these atomic media offer a complex refractive index as the weak probe beam passes through. As a result, the beam encounters strong dispersion along with resonant scattering. In a typical transmission measurement, where a probe beam passes through a large atomic ensemble the absorption properties are dominant and have significant contributions in the detected signals. The weak dispersion effects only change the global phase of the beam and leave no influence on the detected signal. In contrast, the confined atomic ensemble featured in the experimental setup in Chapter 5 produces spatially varying phase modulation much like a lens. Due to the inhomogeneous dispersion, the mode of the propagating light beam gets altered which strongly depends on the laser detuning from the atomic transition line. Combined with the absorption which is also spatially dependent due to the atomic density, the exact probe-beam field profile after passing through the cloud requires a complete understanding of beam propagation through the atomic ensemble.

In this chapter, dispersive effects are utilized for non-destructive measurements. The beam profile after passing through confined atomic cloud is calculated by a beam propagation model. By analyzing the full beam propagation, complete absorption line shapes are calculated which are compared with the detected signals. Furthermore, Rydberg EIT line shapes are studied where the control beam additionally modifies the inhomogeneity of the dispersion.

6.1. Atomic ensemble as dispersive medium

In the detection scheme, a Gaussian probe beam is mode overlapped with the optical lattice beams. As the trapped atoms acquire the lattice beam configuration, the probe beam encounters a high degree of mode overlap with the atomic ensemble. Due to the extended overlap between the light and atoms, the interaction strength which is a measure of light-matter coupling, gets enhanced. Among the various other techniques, a system presented in this work provides interesting light matter interface. As a figure of merit, optical depth (OD) of this system demands a need for detailed study of beam

propagation through the cloud which acts as an optical media that modifies both, the absorption and transmission. To a good approximation, the atomic cloud is assumed to have radially symmetric Gaussian distribution with much longer extent along the fiber axis.

$$\rho = \rho_0 \exp\{-\frac{z^2}{2\sigma_z^2} - \frac{x^2 + y^2}{2\sigma_r^2}\} \tag{6.1}$$

To obtain the beam propagation, the paraxial wave equation (PWE) with the atomic density distribution in the geometric confinement is solved. As discussed in Chapter 2, atomic cloud serving as a medium with susceptibility, χ containing the features of absorption and dispersion is represented as

$$\chi = -\frac{\sigma_0 \rho(x, y)}{k_0} \frac{2\delta_p/\gamma - i}{1 + 4(\delta_p/\gamma)^2 + I/I_{sat}}, \tag{6.2}$$

where experimentally convenient parameters, I and I_{sat} are the probe beam intensity and the saturation intensity associated with the transition. In the experiment, the power was kept below $200\,\mathrm{pW}$ which corresponds to intensity below 1% of I_{sat} and can be ignored for the subsequent calculations. The susceptibility is related to the real and the imaginary parts of refractive index as shown by the Kramer-Kronig relation as shown below:

$$n_r = 1 + 1/2Re(\chi), \tag{6.3}$$
$$n_i = 1/2Im(\chi). \tag{6.4}$$
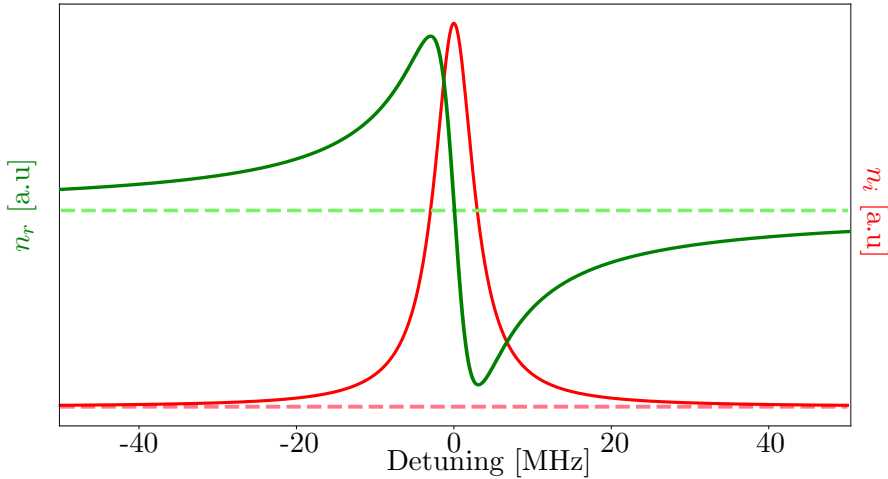
Figure 6.1.: Detuning dependence of real and imaginary parts of refractive index. The dashed lines represent signal in absence of atoms.

The Figure 6.1 shows the qualitative values for refractive indices for varying laser detunings. To include the complete atomic distribution, χ is calculated for the atomic cloud released from the confinement. Along with density dependence, the real and

the imaginary parts of refractive index are highly modulated by the detuning of the probe laser beam. An illustration is shown in Figure 6.2 where the real and the imaginary parts of refractive index is represented for a set of detunings and radial positions. It is evident from the simulated results that the values of the two indexes are maximum at the center of the cloud where the density is maximum. Additionally, the spectral response adds meaningful information about the type of interaction – in the pure absorption, n_i, the values drop very rapidly as one goes away from the detuning. While for the dispersion, i.e. n_r, remains non-vanishing for farther detunings. Moreover, the dispersive detection techniques have been proven useful for non-destructive measurements. Here, the laser detuning is kept far enough to minimize the on-resonant scattering processes while still having significant influence to be detected utilizing the dispersive features. In the coming sections, these features are explored with applications in detection techniques.
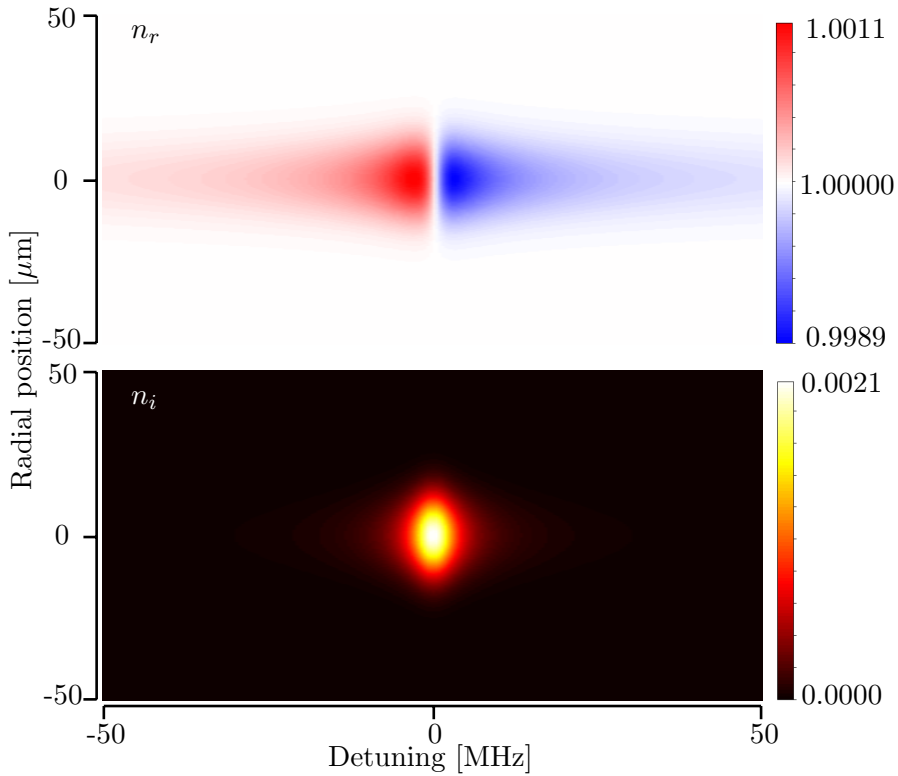
Figure 6.2.: Detuning dependence of real and imaginary parts of refractive index for radial distribution.

6.2. Polarization rotation

In the cold-atom physics one of the most conventional detection schemes is using absorption imaging where an on-resonant probe beam is sent through the atomic sample. As the beam propagates, it gets scattered by the atomic cloud with the maximum scattering rate occurs when the the laser is tuned exactly to the corresponding atomic transition line. Fluorescence or absorption imaging techniques are based on this scattering phenomenon. Although such methods are widely utilized in the fields of cold atoms, it also comes with certain issues. One of the major limitations is that this technique is destructive, in that once an atom undergoes the scattering event, either it looses its coherence properties or it gets kicked out of the region of interest due to momentum transfer. No further measurements can be made regarding its quantum properties. Alternate methods need to be established to circumvent these issues. Off-resonant imaging can reduce the scattering rate but it simultaneously suffers from the noise as the signal strength also gets reduced significantly as depicted in the Figure 6.1. Dispersion, as the signal does not decay as rapidly as with the scattering rates shows a potential tool in non-destructive detection. In this case phase of the beam gets altered based on the detuning from the atomic transition as shown in Figure 6.1. Using a phase sensitive detection scheme, presence of atoms can be estimated. To implement this scheme, atomic transition rules are utilized for precise controls. In particular, polarization dependent phase shift is generated which results in rotation of the beam's plane of polarization and can be detected using a balanced pair of photo-detector.

6.2.1. Detection scheme

This detection technique utilizes the ground state hyperfine states of ^{87}Rb that have relatively very long coherence time. This makes these states suitable for applications like photon storage, atomic clock, interferometry. Common to all these experiments lies the challenge of making precise measurement of the atomic population of the two hyperfine sates. Among the other noise sources, the shot-to-shot atom number fluctuation causes noise in the measured quantity. The remedy is to measure the population in both the states in the same experimental run. A typical on-resonant detection leading to scattering can alter the population of the two states. Hence, simultaneous measurement of the two states is prone to inaccuracy associated with the measurement process. In contrast, the dispersion signal being non-vanishing even for far off-resonance where the population mixing processes are insignificant. Therefore, simultaneous detection of two states is not limited by the detection process. Furthermore, longer integration times are possible which reduces the detection noise. For experimental realization, ultra-cold ^{87}Rb are prepared in $|F = 1, m = 0\rangle$. The hyperfine transition resonant radio frequency of 6.835 GHz RF is coupled to drive the atoms to $|F = 2, m = 0\rangle$. These states are decoupled from the first order magnetic Zeeman effects therefor are used for precision measurements as in the case with atomic clock, hence also known as clock states. Based on the amplitude and the pulse dura-

tion, different RF spectroscopy schemes are applied to manipulate the atomic states in what is known as Bloch sphere. Such schemes are typically used in precision measurements using atom interferometry, atomic clock, quantum information processing, etc. The goal here is to establish a novel detection system while preserving the atomic number state such that repeated measurements can be performed to obtain more accurate information about the atomic population and hence the associated measurements. To achieve this goal, two probe beams, tuned near D1 transition line are used. In particular, the two beams address the transitions $|F = 1, m = 0\rangle \leftrightarrow |F' = 1, m = 0\rangle$ and $|F = 2, m = 0\rangle \leftrightarrow |F' = 2, m = 0\rangle$. To establish the dispersive detection, both the lasers are set off several linewidths away from the actual transitions as shown in Figure 6.3(a).

For the chosen level scheme shown in Figure 6.3(b), the π transition is forbidden due to the transition rules. Hence, a laser beam corresponding to π transition will not have any influence from the atoms. While the σ transitions cause the beam to encounter a phase shift. As a result when a linearly polarized beam at certain angle is passed through the cloud, it becomes elliptical. which results in axis rotation when passed through a waveplate. The rotated beam has different intensity in the two arms as it passes through the PBS. Two detectors placed on the both arms show imbalanced signals.The difference between the two is a measure of polarization rotation, which inherently gives an estimate on atom numbers in the two states in the same experimental run.
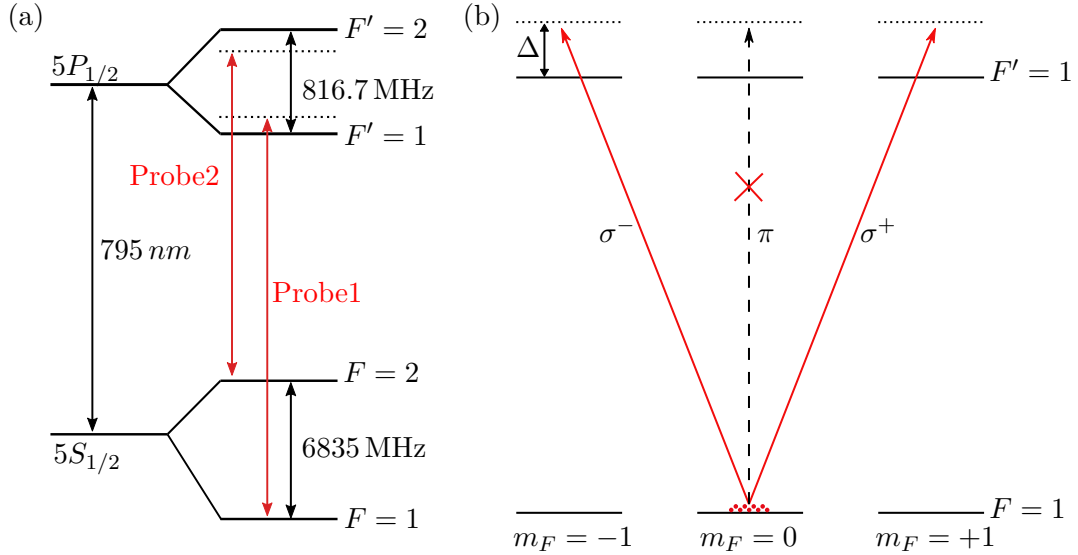
Figure 6.3.: (a) D1 transition line structure of ^{87}Rb. Two beams, probe1 and probe2 address the population in $|F = 1\rangle$ and $|F = 2\rangle$ states. (b) Magnetic sublevels of the two hyperfine lines with allowed transitions.

To illustrate the polarization rotation effects, D1 transition of ^{87}Rb $|F = 1, m = 0\rangle \leftrightarrow |F' = 1, m = 0\rangle$ is utilized as shown in Figure 6.3. Linearly polarized probe beam is

sent through the cloud. The axis of the beam is precisely adjusted using a half wave-plate. Additionally, a weak magnetic field is applied to set the quantization axis along y-axis as shown in Figure 6.4. As the beam passes through the cloud, the light-field component along the y-axis can only excite π transition which is forbidden for the selected transition states. Hence, the beam does not sense the presence of atoms. While the orthogonal component, e.g. polarization axis along x-direction excites σ transitions. As the beam passes through the cloud, it encounters a polarization dependent phase shift much like birefringence. As a result, the linear beam becomes circular. A pre-adjusted quarter waveplate rotates the primary axis and make it linear. The beam after passing the PBS shows imbalance in the intensity in the two arms which is detected on detectors.
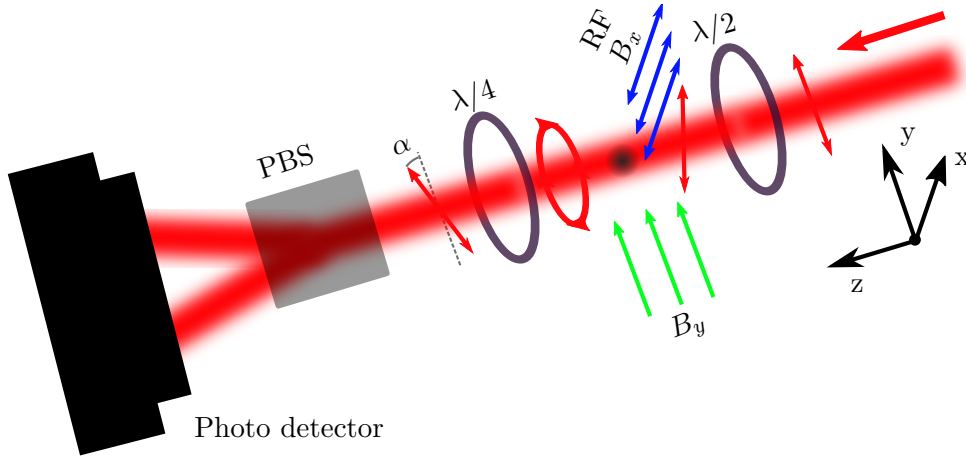
Figure 6.4.: Polarization rotation detection experimental setup. Two probe beams are overlapped and exiting from a single mode fiber.

6.2.2. Imaging

The beams after the PBS is directed on spatially distinct parts of a CCD camera. Additional sequence of images are taken to isolate the background light from the actual image of the cloud. A typical processed image is shown below in Figure 6.5. The polarization angle scales with the atom density hence the larger numbers correspond to more atoms. It is noteworthy to mention that the positive and negative values are results of lack or gain of light falling on the sensor. The signal is in sharp contrast with absorption imaging. For the experimental parameter, the number of atoms were about $2.0 \cdot 10^6$. The beam detuning was set beyond $-40\,\mathrm{MHz}$ to minimize any absorptive effects and thus the interferences in the dispersive detection scheme. Another aspect on noise estimation is that the off-resonant dispersion does not have steep dependence with the laser detuning, hence the frequency noise of the laser has relatively weaker influence on the measured signals.

Towards the detection, the atoms are prepared in the $F = 1, m_f = 0$ state, an RF
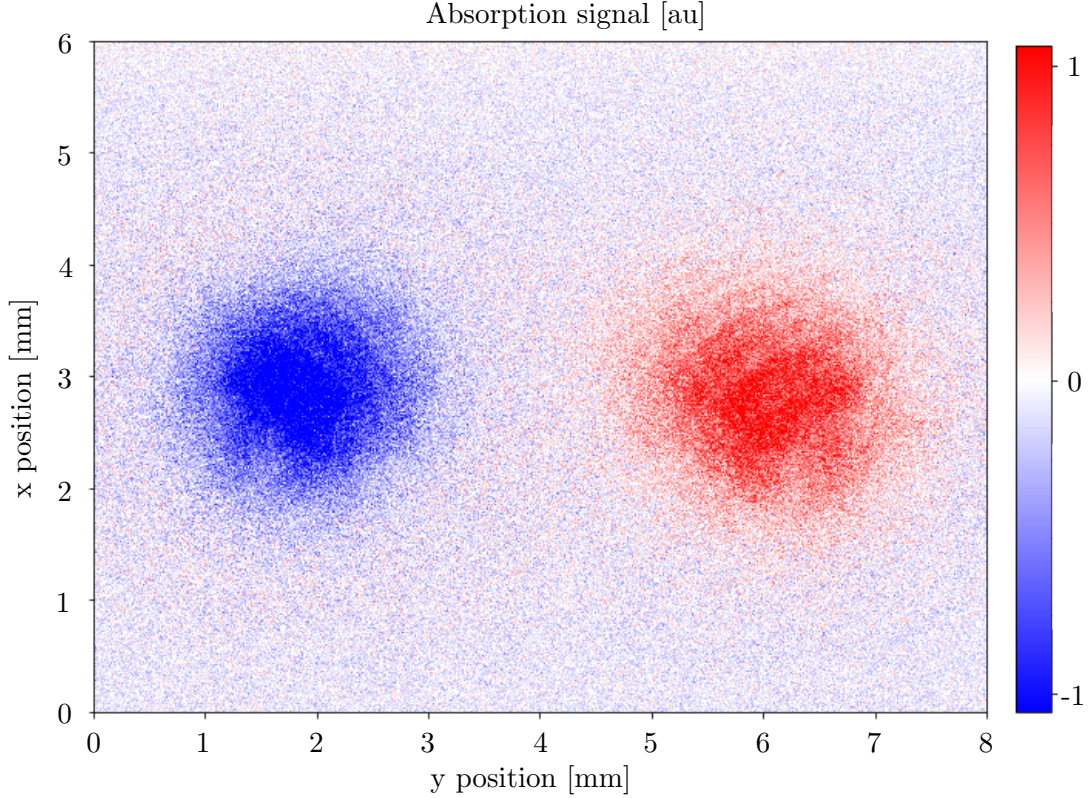
Figure 6.5.: Polarization rotation imaging. Background removed recorded signal shows reduction in the beam intensity in one arm and the enhancement in the other.

source tuned to the ground state hyperfine transition, $6835\,\text{MHz}$ is applied which results in Rabi oscillations in the atomic population. By varying the RF pulse duration, τ_{RF} several population swapping can be observed. A detection scheme as shown in Figure 6.5 is set up for $F = 2$ state. By adjusting RF pulse duration, the images for different relative population are recorded. The population for state, $F = 1$ is measured by repeating the experiment and using a corresponding laser. The combined results are plotted in the Figure 6.7, where the population swapping can clearly be seen. The sum signal has noise subject to the fluctuation in the atom number as the individual state measurements are made at different runs.

6.2.3. Simultaneous detection of two states

The noise due to atom number fluctuation can be circumvented by simultaneous state detection in the same experimental run. As with the dispersive imaging, the condition is fulfilled for the reason that the measurement process does not alter the relative population in the two states. The time sequence for such detection is shown in the Figure 6.6.
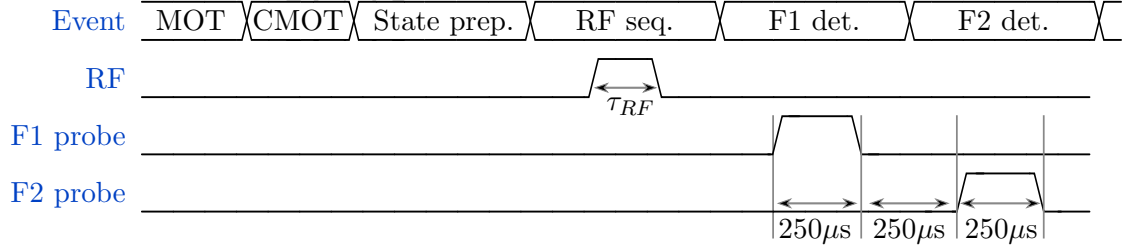
Figure 6.6.: Rabi oscillation between the two hyperfine states.

Here, short pulses of both the probe beams are sent sequentially to record the population in the two states. The pulse durations were kept short enough to minimize the atom expansion yet long enough to minimize small measurement noise. Additionally, the probe detunigs corresponding to the two states, namely $|F = 1\rangle$ and $|F = 2\rangle$ are kept $+200\,\mathrm{MHz}$ and $-300\,\mathrm{MHz}$ respectively. Such large detunings minimize the scattering rate which in turn reduces population transfer between the two ground hyperfine states.
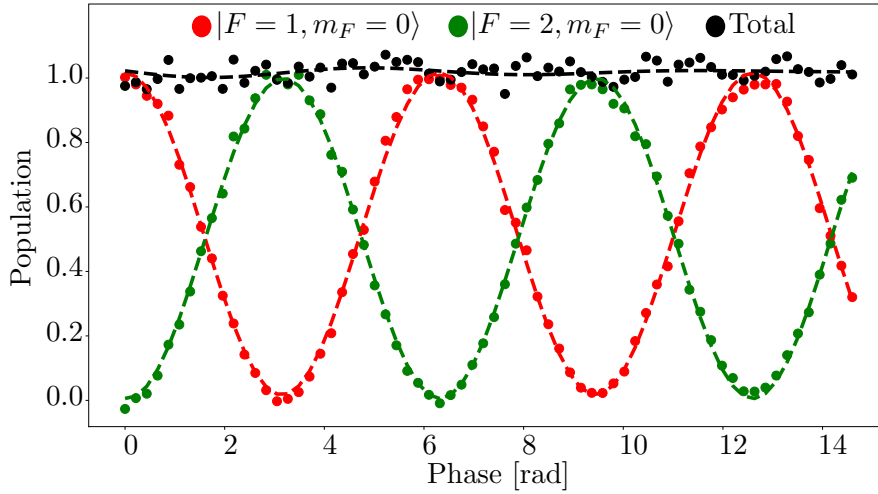
Figure 6.7.: Rabi oscillation between the two hyperfine states

Using the measurement schemes shown in the diagram in Figure 6.6, the Rabi oscillation of the two clock states are detected for the same atomic cloud. This information is used to normalize the atom fluctuation in each individual run. The corrected Rabi flopping is shown in Figure 6.8 where the population difference is plotted against the phase. The value of the phase is obtained by the following relation,

$$\Phi = \Omega_{RF}\tau_{RF}, \tag{6.5}$$

where, Ω_{RF} is Rabi frequency associated with RF transition which mainly depends on the RF intensity and τ_{RF} is the RF exposure time. As is evident, the shot-to-shot

fluctuations due to the atom number is a lot lesser than for the independent measurements. However, there are small deviations still present which can be attributed to the state decoherence, atom expansion during detection or noise coupled to the balanced detector.
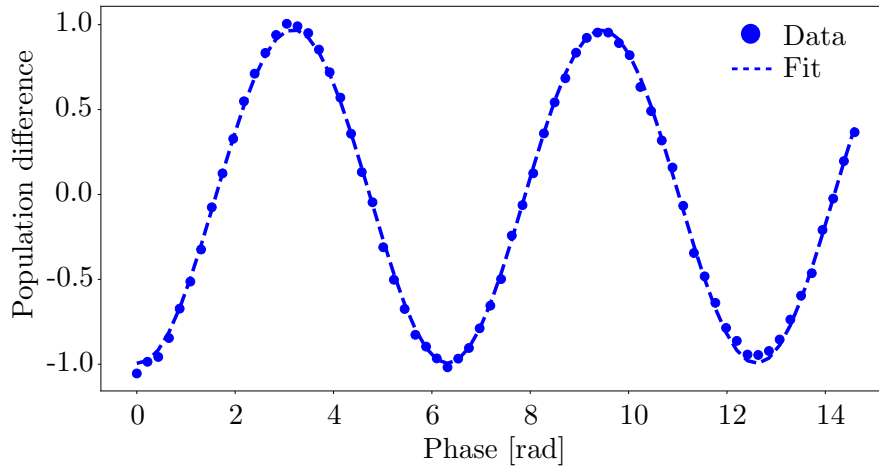
Figure 6.8.: Rabi oscillation between the two hyperfine states

This section concludes with a demonstration of dispersive effects as polarization rotation, and consequently a tool for non-destructive imaging. The next section concentrates on the spatial properties of a probe beam passing through the atoms in an extended confinement with comparable geometries.

6.3. Beam propagation through extended cloud

As it was evident in the Chapter 5, the exact transmission lineshapes were not explained by the Lorentzian model. The geometrical conditions hint at a requirement for an additional model which should take care of the beam as it passes through the elongated cloud. This is argued from the reason that the atomic medium is no longer homogeneous throughout the beam distribution. Hence, this results in lensing-like effects. In this section, the goal is to develop a model to accurately incorporate the dispersive effects in addition to the absorption.

6.3.1. Split step method

To simplify the model, the atomic cloud is split into small slices as shown in Figure 6.9. As the entering light field passes through each of the slices, it gets modified due to the atomic density distribution. Under the slow-varying-envelope-approximation (SVEA), the complex amplitude of the electric field is described by the Helmholtz equation

$$\frac{\partial \boldsymbol{A}}{\partial z} = \frac{i}{2k}\nabla_\perp^2 \boldsymbol{A} + \frac{ik}{2n_r^2}\chi \boldsymbol{A}, \tag{6.6}$$

where, $\boldsymbol{A}$ and ∇ are complex field and Laplacian operator.
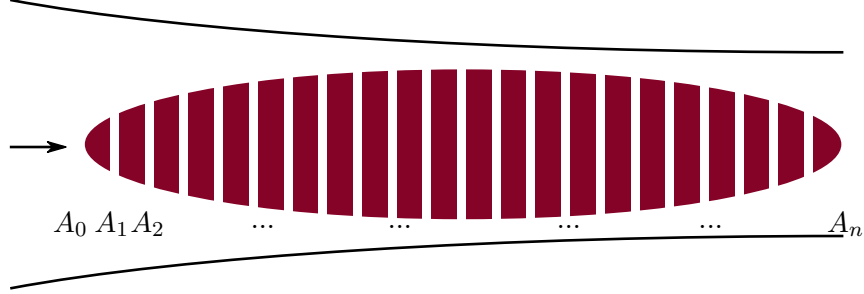
Figure 6.9.: Beam propagation through atomic cloud sections. A_i represents conplex field after i_{th} slice.

The Helmholtz equation is numerically solved by using so-called split-step method. The input field represented by $\boldsymbol{A}_0$ transforms into $\boldsymbol{A}_1$ after passing through the first slice of the cloud as a result of the Equation 6.6. The newly obtained field becomes input for the next atomic slice. The thickness of each of these slices is taken small enough such that the z-dependent higher order terms remain insignificant. The evolving light field after n slices gives an estimate of the complex electric field along the z-axis. The numerically efficient approach of solving the split-step method is described in the Appendix A.1 where the differential equation term is avoided by transforming the equation 6.6 in Fourier domain. With the fields obtained for different axial positions the complete intensity profile is reconstructed.

6.3.2. Propagation of light: Micro-lensing effect

The results are shown in Figure 6.10 for various laser detunings. In here, beam profile for three different detunings are presented. Much like lensing effects, depending upon the detuning, the beam either focuses or defocuses. The effects are results of dispersive interaction which has a contrasting difference from the absorptive scattering. The dispersive processes are non-dispersive where no photons are scattered randomly whereas the absorption is a result of random scattering of light resulting in loss or heating. A remarkable point to notice is that for the negative detuning, the beam stays confined in the center of the atomic cloud in contrast with the positive detuning case. This adds more complexity in the final beam which comes out of the cloud due to the radial density variation of the atomic cloud. In particular, the negatively detuned beam encounters denser atomic cloud which results in a more absorptive response. On the other hand, the positively detuned beam avoids the cloud. This control has significant effect on the final absorption signal. Moreover, it adds another control knob to enhance or diminish the light-matter coupling. The probe beam after the fiber has additional layer of complexity due to the mode selectivity properties of the fiber which filters out the Gaussian mode from the transmitting beam after the atomic cloud.
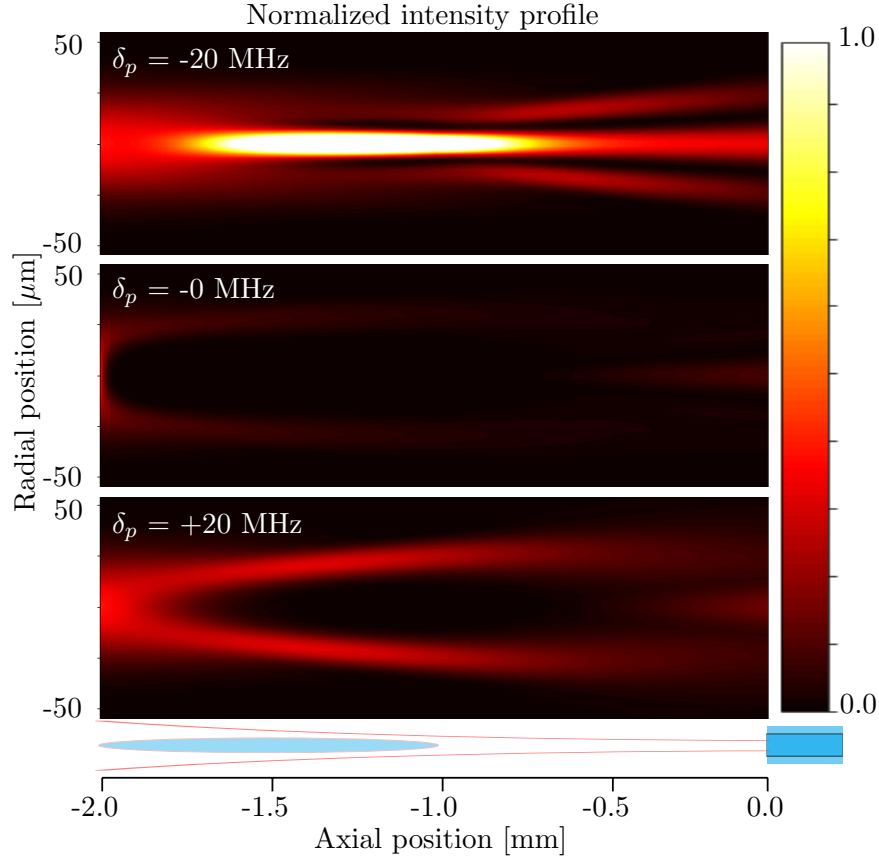
Figure 6.10.: Intensity profile for three different detunings. Probe beam enters from left side into the cloud shown in the lowest part. Different detunings show significantly altered beam profile in the way a lens works.

6.4. Micro-lensing induced lineshapes

Absorption imaging discussed in the Chapter 3 is only limited to detecting atoms when they are outside the fiber. As these atoms are transported inside the fiber, a new technique needs to be developed. For this purpose, the probe beam is overlapped on to the dipole trap beams which as a result passes through the atomic cloud. By scanning the probe detuning the atomic responses can be detected and hence the spectral information about the atoms. Interesting features about such interface, like optical depth can be estimated by this technique.

To obtain the exact transmission detected on the PMT, a complete information of the beam as it passes through the cloud, is needed. First, a model is constructed for the trapped atoms outside the fiber to make the problem simple. Then the transmitting intensity profile for different detunings show interesting features. The probe beam is coupled into a single mode fiber after passing through the hollow-core (HC) fiber. The coupling efficiency into the HC fiber is above 90% and that for the single mode

fiber is $> 70\%$. To include the finally detected beam into the single mode fiber, high coupling into HC fiber helps in simplifying the model.

6.4.1. Detection setup: Mode selection

Absorption causes the drop in the intensity of the propagating beam, while the dispersion is responsible for bending of light. In the case of this work, the cloud is cylindrically symmetric, acting like a thick lens. Hence the beam will not only encounter absorptive losses but will also undergo focusing or defocusing depending upon the detuning. For the typical experimental constraints, SVEA treatment is valid and appropriate.

The complete model for understanding the lineshape requires the inclusion of detection scheme. In this case, the first contribution comes from the propagating beam profile as certain part of it gets terminated due to its size exceeding the HC fiber wall. This is clearly visible in the the beam profile images and the model is included in the calculations discussed in Appendix A.2. In addition, the probe beam is coupled into a single mode fiber for the final detection. This fiber essentially selects the Gaussian mode of interest which is sensed on a PMT. The detected signal is calculated by integrating the field overlap between the fiber mode and the light field profile as:

$$I = \int_s \boldsymbol{A}(x,y)\mathcal{E}(x,y)dxdy, \tag{6.7}$$

where, s represents the area of integration which encompasses the HC fiber boundaries. The results can be perceived as effective change in coupling efficiency as a result of atom-induced-lensing. To estimate the transmission efficiency altered due to the atomic cloud, the overlap integral is normalized with a signals with atoms of homogeneous density as to isolate the shift due to lensing. In the Figure 6.11, the dispersive contribution is plotted along with the absorptive part. The absorptive part mainly remains symmetric about the $\delta_p = 0\,\text{MHz}$ in all three cases, whereas the dispersive contribution has significantly strong asymmetry. The combined signal, which is actually detected on a sensor, shows additional absorption along with an asymmetric shift. The reason for small bump near $-15\,\text{MHz}$ is the suppression in transmission at $-20\,\text{MHz}$ as a result of dispersion.

6.4.2. Transmission profile

The transmission signals for an expanding atomic cloud are shown in Figure 6.12(a). Here, the cloud is released from the trap and monitored continuously using a weak probe beam. Utilizing the thermal expansion governed by the temperature of the cloud, the radial extend is estimated for different evolution time. The experiment is repeated for a set of varying detunings to obtain a complete spectral features. The overall features can very well be compared with the simulation shown in Figure 6.12(b). Moreover, the lack of non-trivial absorption can be seen near a detuning of $-15\,\text{MHz}$ which is in good agreement with the simulation.
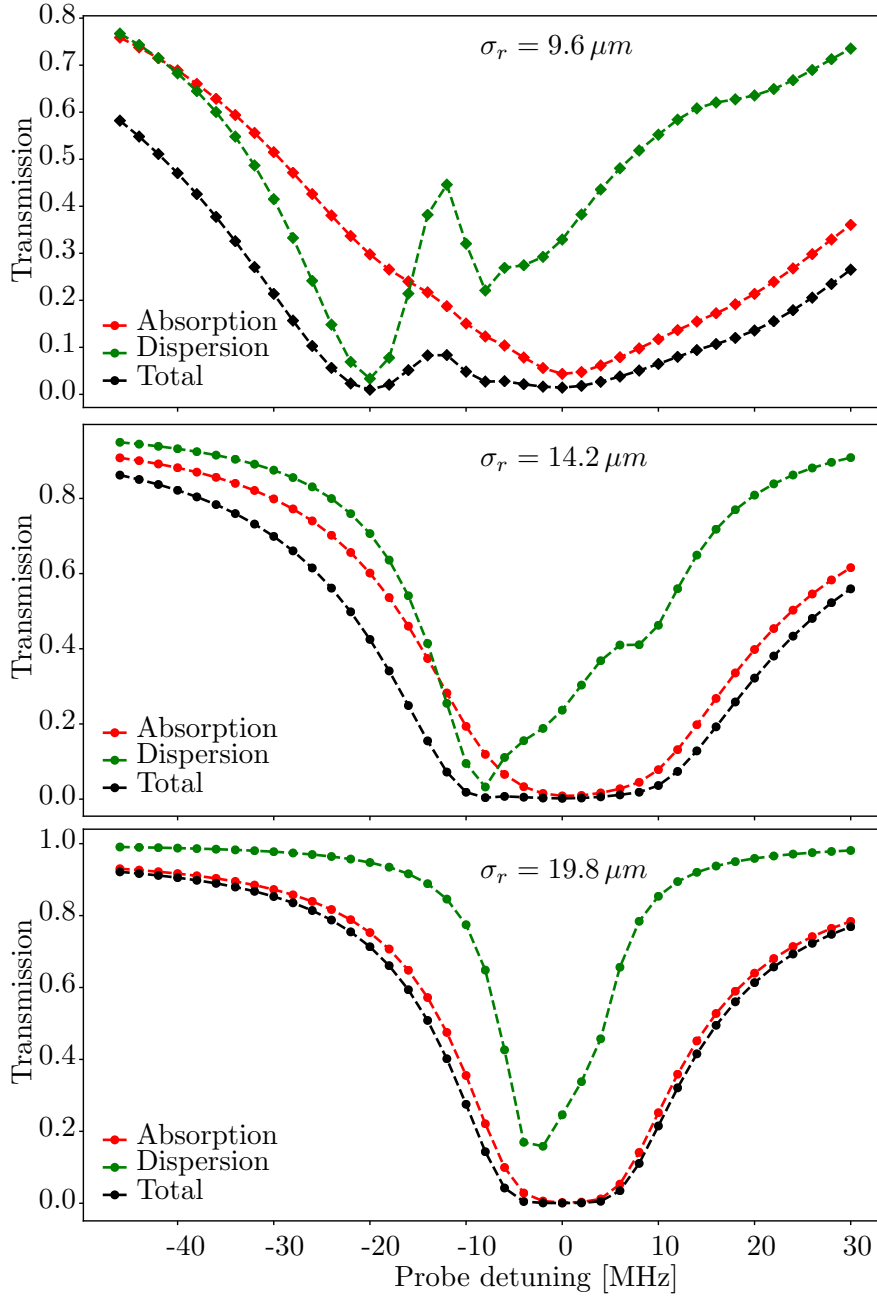
Figure 6.11.: Simulated lineshape for the different cloud sizes, σ_r.

Horizontal cuts of the Figure 6.12 are plotted in the Figure 6.13. In the Figure (a), the perfect agreement between the spectral lines are good indication of lensing induced line shapes. As for a large atomic size, the absorption profile resembles that obtained from a Lorentzian model which is symmetric in nature. For smaller cloud sizes the asymmetry increases which can not be explained by a simple Lorentzian model. Main
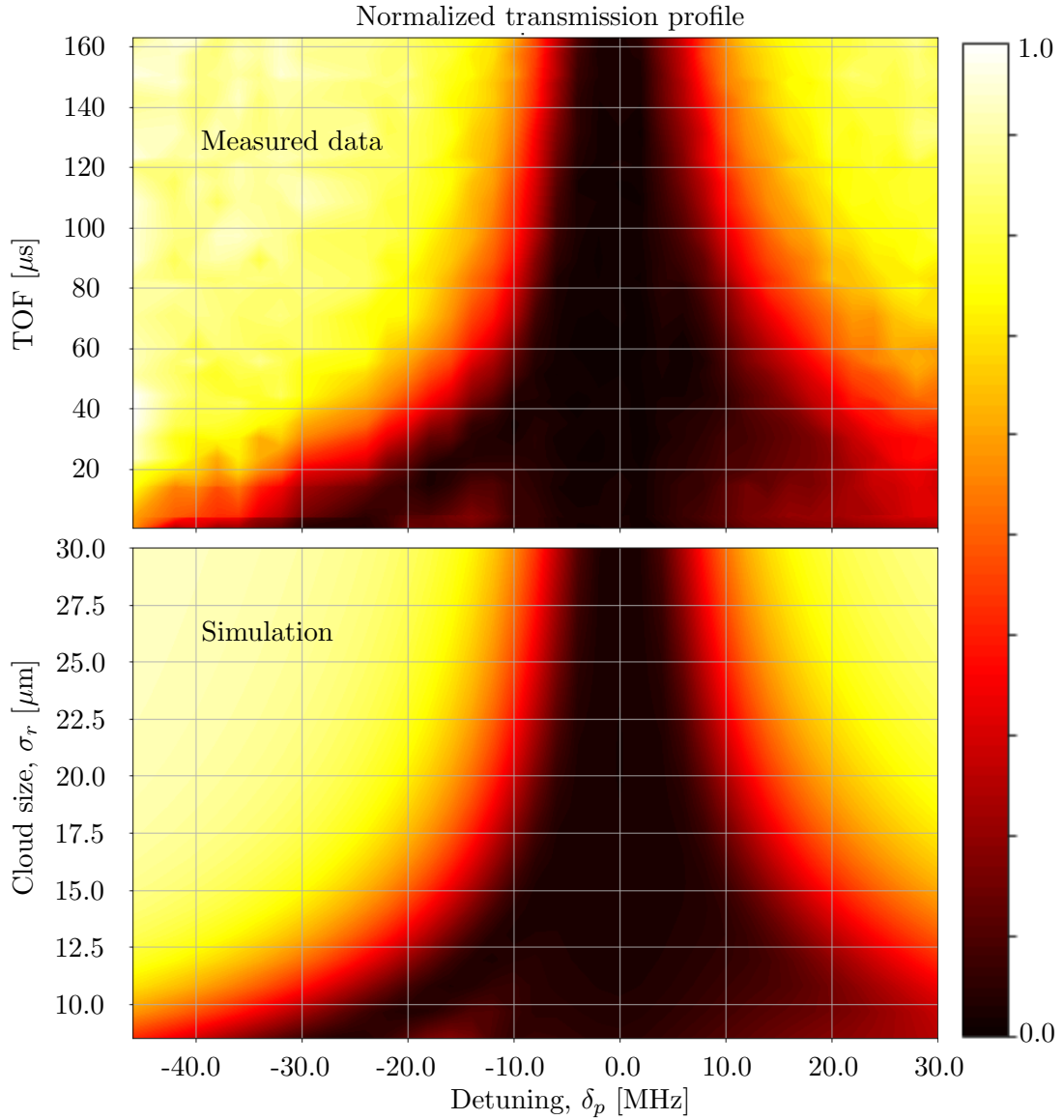
Figure 6.12.: Complete temporal and spectral transmission signal for (a) measured data and (b) simulated result.

point of focus here lies near detuning $-15\,\mathrm{MHz}$ where an increase in transmission can be seen. The explanation for this behaviour is due to the lensing effects, which is inhomogeneous, i.e. for one detuning it focuses the beam, while it defocues for the other. As a result, the beam is completely lost for a detuning near $-25\,\mathrm{MHz}$ leaving an apparent bump near $-15\,\mathrm{MHz}$. This appears because of the coupling into the single mode fiber.

The Figure 6.13(b) shows a simulation and data for OD measurements inside the fiber. The overall features satisfy the data, while the exact lineshapes lack from the goodness

of the model as for the case where the atoms are inside the fiber, the complete model needs a term for guiding properties of the hollow-core fiber which is a work of separate research topic.
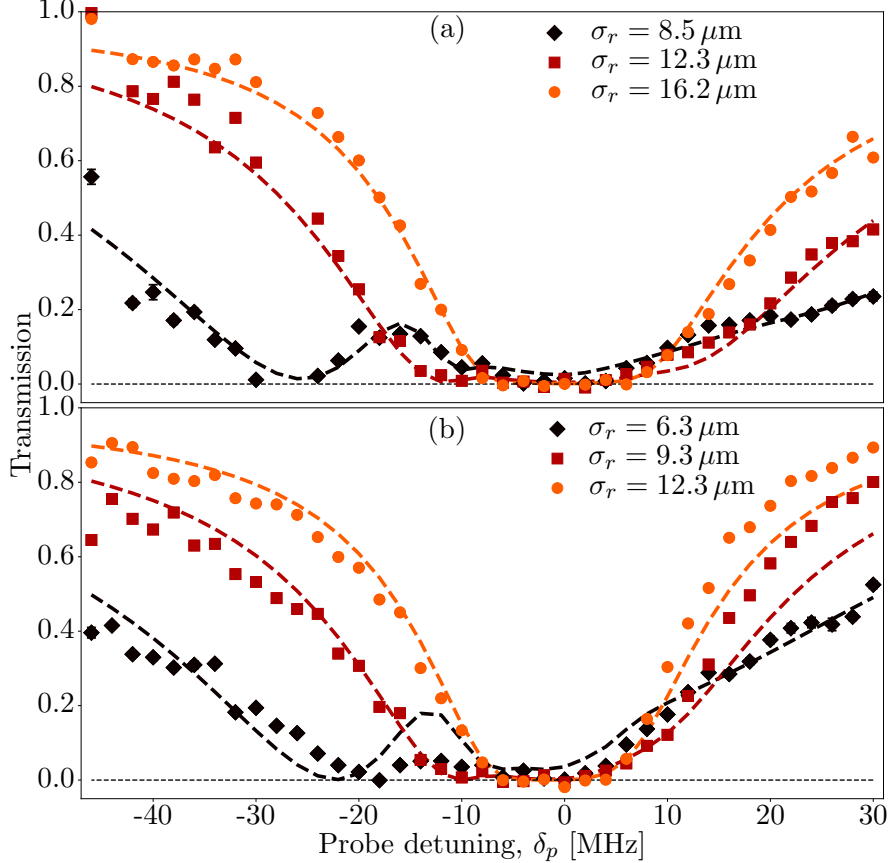
Figure 6.13.: Transmission signal for (a) outside and (b) inside the fiber. The dashed lines are fit model and markers are data taken from the experiment.

To compare the accuracy of the beam propagation model, a simple Lorentzian model, discussed in Chapter 2 is fitted to obtain the OD for the transmission data. As is evident that such model lacks the dispersive effects, hence the lineshapes deviate broadly for the tightly confined clouds. A comparison between the two models is plotted in Figure 6.14. A deviation above 50% in OD values are observed. For cloud sizes, comparable or larger than the probe beam size, the deviation is negligible.

6.5. Rydberg EIT line shapes

With the results strongly depending upon dispersive nature of the atomic cloud, now the goal was to understand the line shapes for the Rydberg EIT processes, in particular near the two-photon resonances. As known for the EIT processes, the control beam
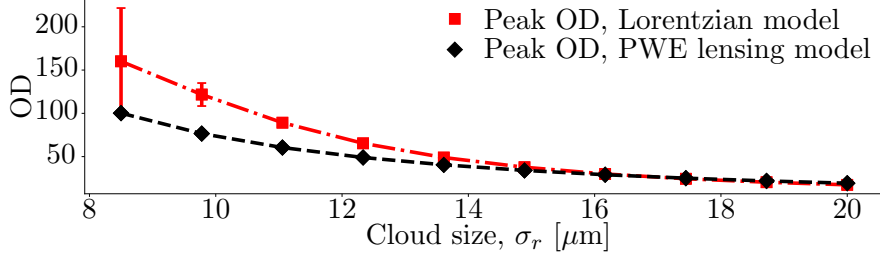
Figure 6.14.: Comparison of OD estimated from the PWE model and Lorentzian model

modifies the optical properties of the atomic cloud. The results combined with the tightly confined atoms should again require a beam propagation model over standard EIT model discussed in Chapter 2. The control beam further modifies the susceptibility radially as the control intensity is overlapping with the probe beam

$$\chi_{EIT} = \frac{\sigma_0 \rho(x,y)}{k_0} \frac{i\gamma/2}{\gamma/2 - i\delta_p + \frac{\Omega_c^2(x,y)}{\Gamma/2 - i(\delta_p + \delta_c)}}, \tag{6.8}$$

where, $\rho(x,y)$ and $\Omega_c(x,y)$ are atomic density and control Rabi frequency. In this case, the modification in the optical susceptibility is primarily affected by two experimental constraints. The first case is induced by the geometrical configuration of atoms as present in the previous case with two level system. The second factor is considered due to the radially varying control Rabi frequency since the control beam propagates through the HC fiber. It is evident from the equation 6.8 that the local Rabi frequency, Ω_c has certain influence on the susceptibility, χ_{EIT}. To this end, the control beam profile is approximated to a Gaussian distribution as the influence of the atoms will have marginal effects,

$$I_c(r) = I_{c0} e^{-(\frac{r}{\sigma_r})^2}. \tag{6.9}$$

EIT lineshapes are studied for two distinct control detunings to explore the spectral features. The transmission signals are plotted in the Figure 6.15. Here, the particular interest is in the lineshapes near the EIT resonances. For the given cases, the lineshapes show significantly distinct asymmetry. The model for the EIT system is calculated by introducing the radially varying control Rabi frequency, $\Omega_c(r)$ in the equation 6.6 and followed by the numerical treatment. The numerical calculations confirm the observed EIT line features. This result is of significant importance for the reason that such asymmetries can arise from various factors such as ion production or induced effects. While, the work done in this thesis claim that a geometrical reasons can also modify the lineshapes.

In conclusion, this chapter explores the significance of the dispersive effects as a result of the real part of the susceptibility. On the one hand, the atomic population is preserved as a result of non-destructive nature. On the other hand, the strong alteration in transmission lineshapes are obtained. These are some results of significant
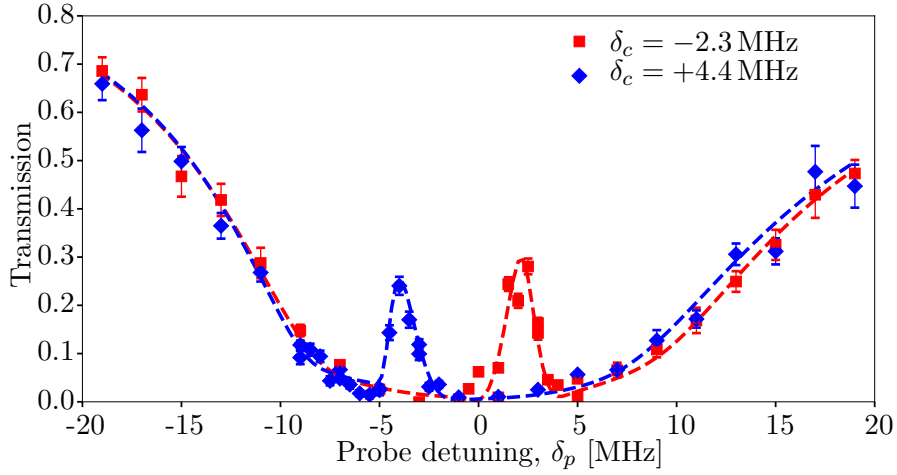
Figure 6.15.: Comparison of EIT line shapes using the PWE model for two different control detunings.

importance as the exact lineshape can have a range of underlying mechanism. In this case, the geometrical constraints contribute to similar alterations which is otherwise absent in such simple setup. In addition, the controlled environment can be utilized to manipulate the light propagation. As was apparent from the results that the beam can be made to stay focused in the core of the cloud or can avoid the cloud by just changing the laser detuning. The significance is in the fields of photon storage or spectroscopy. Rydberg EIT lineshapes have shown added feature as a result of control beam overlap which shows in excellent example of controlling the light not only by making it transparent but also by physically altering the path.

7. Conclusion and outlook

The results presented in this thesis demonstrate promising outcomes in the framework of quantum technology and its applications. The work can be categorized in three main sections – Development of light-matter overlap for strong interaction, Rydberg excitation inside a confined geometry and light propagation through the tightly confined media.

As for creating strong light-matter interaction, the spatial overlap of light and atomic cloud is maintained for an extended length beyond the limitations imposed by Rayleigh range. This is overcome by utilizing a hollow optical waveguide, namely a hollow-core photonic crystal fiber. The task of the waveguide is not limited to the optical confinement, but to further utilize the optical forces in what is known as dipole trapping to make an equally extended confinement for atomic media. High OD for a typical atom number is an indicator of the strong light-matter interaction. In this thesis, the novel fiber-atom interface is created and studied.

Considerable attention have been drawn towards creating long-range interaction using Rydberg atoms. The natural choice is to utilize the experimental platform set using the light-matter fiber interface. Quasi-one dimensional chain of Rydberg polaritons have potential significance in understanding non-classical states of light. The inherent high sensitivity of the Rydberg atoms towards external fields is underlying driving force to achieve the goal. However, it is this high sensitivity that poses an experimental barrier to excited the atoms to high Rydberg states due to the stray field present near fiber surface as confirmed by the shift observed in the EIT peaks. In attempt to overcome the barrier, a variety of fibers with different core and inner wall coatings have been tested. To conclude the outcomes, a coating of Rb vapour inside the fiber wall demonstrate the potentiality to nullify the electric field. This can be understood due to the fact that the atoms shield the fiber from inside in much like Faraday cage. The results open up a broad scope for creating high Rydberg excitation which is a key requirement for long range interactions.

With the promising applications, the atom-fiber interface lays a novel experimental platform. However, critical understanding of light propagation through such extended media becomes an independent topic. As hinted by the enhanced susceptibility offered by the atomic media which is indicated by high OD, the dispersive effects also plays a crucial role. The radially inhomogeneous phase delay caused by the atoms leads to bending of light in much like a lens. Furthermore, by adjusting the laser detuning the sign of the lens is inverted. The theoretical model developed in this thesis and backed up by the experimental measurements demonstrate a way to control and manipulate a propagating beam through the atomic media. For instance, as has been discussed, the probe beam, in one case of detuning travels through the

central part of the atoms while for the opposite detuning the beam avoids the atoms.

In this thesis several experimental achievements are illustrated which advance our understanding towards creating strong light-matter interaction utilizing a geometrical confinement. The confinement over the light field is achieved by using hollow-core fiber as an optical wave guide. Consequently, optical dipolar forces are exploited to trap and transport cold atoms in the same confining geometry giving an excellent overlap between light and matter. Not limited to the Rayleigh range, such confinements offer a novel platform for arbitrarily extended interaction length.
To precisely control the cold atoms along the fiber axis, optical conveyor belt is realized through the fiber. The exact position is extracted by the adjusting the time and speed of the optical transport. By additionally overlapping a weak probe beam a light-matter interface is realized. As an indicator to the strong coupling, the light propagation is highly modified through the confined atomic cloud. The results reflect on the detected transmission signals in our detection system which is also confirmed by a beam-propagation model. The findings show that the dispersive effects, which are not too prominent in a typical atomic cloud, here plays a crucial role in understanding the transmission processes. Furthermore, the model is utilized to understand the lineshapes associated with Rydberg EIT. The results show a detailed understanding of the obtained asymmetry in the line. Typically such lineshape deformations have been reported to arise from several different mechanisms. Rydberg excitation near surfaces have been difficult task due to presence of charges or induced fields. In this thesis, similar shifts are observed which confirms a presence of electric field inside the fiber. Although, presently it sets a limitation in addressing very high Rydberg states which are the key desire for the many-body photonic states. To circumvent the fields, additional experimental setup is replicated with different fibers inside the vacuum chamber. Here, however, Rb vapour at room temperature is exposed for several months which eventually cover the inner wall of the fibers. The results have shown remarkable achievements in exciting higher Rydberg states. This way Rydberg EIT upto 80 have been realized with not so much significant shift.

Following is a summary of the task performed:

- Atom transport

- High radial and longitudinal control

- Strong effects on light: dispersive and absorptive

- Rydberg EIT inside fiber

- Room-temperature Rydberg EIT high state possible

The research work performed for this thesis offers a range of promising perspectives in the fields of quantum information, quantum computation and sensing. The major aspect of the atom guiding techniques is to provide a precision control for

manipulating quantum systems. Enhancement of light-atom interaction becomes essential particularly at a few photon level. As shown in the first part of the experiment, as a figure of merit, the enhancement of optical density in a simple setup and not large number of atoms show has paved a way into creation of single photon type interactions. Light propagation through a tight cloud of atoms as shown in the discussed experiment gives a valuable understanding about controlling and manipulation of light. On the one hand, for a given detuning of the laser, the probe beam travels through the denser part of the cloud. On the other hand, for a different detuning, the beam avoids the cloud. This way a precision control over light-matter overlap is achieved. This type of control additionally benefits from dispersive detection where on-resonant losses are reduced. In the Rydberg EIT processes, the control beam further modifies the beam propagation properties which depends on the control detuning and spatial overlaps. Eventually the detected lines reflect the distortion in lineshapes which has important consequences as such distortion can also arise from other mechanisms. In this project Rydberg excitation was explored by observing EIT lines for different states. However, presence of electric field was confirmed which limits the principle quantum number of a given Rydberg state. To understand and circumvent the shift and broadening, different fibers were considered. In an additional setup, Rb atoms filled at room temperature could be excited to n=80 states. These results are remarkable as it opens a way to address higher states which is one of the key requirements for creating strong light-matter interaction.

A list of benefits this project offers:

- High OD for rather small atom number

- Dispersive detections for non-demolition measurements

- Control over light propagation through tight cloud

- Rydberg excitation to high states near surfaces

After understanding lineshifts due to charges, the origin of electric field inside the fiber can be studied and manipulated. This can be achieved by either filling the fibers with Rb atoms or coating the fiber surface using conducting materials. It would be important to study how the light propagation properties are maintained after such coatings. Furthermore, the knowledge of beam propagation can be utilized to address certain part of the cloud. For example, for negative detuning, the probe beam stays in the center, hence the electric field would have minimal affects. Further study of room-temperature system can also be model exactly by the light propagation model as it is a Gaussian sum over a range of velocity class atoms. Light storage and retrieval can be achieved.

A list of future ideas this project offers:

- focusing or defocusing for EIT

- Thermal cloud EIT lineshapes

- Storage and retrieval of light

- coating with metallic materials

As a final remark, the work done for this thesis has addressed and advanced a platform for quantum information, quantum computation and sensing aspects. The implementation of a controllable trap of cold atoms inside hollow core fiber should allow for strong light matter interaction that are limited in free-space system. Rydberg EIT for a variety of configurations demonstrate a mean to realize strongly interacting many-body photonics system. Detailed study of light beam propagation through such atoms in the trap enhances our understanding when dealing such tightly confined media.

A. Appendix 1

A.1. Split-step method

The Helmholtz equation is expressed in a general form as

$$\frac{\partial \boldsymbol{A}}{\partial z} = D\boldsymbol{A} + N\boldsymbol{A}, \tag{A.1}$$

where, the linear and non-linear terms are $D = \frac{i}{2k}\nabla_T^2$ and $N = \frac{ik}{2n_0^2}\chi$. Brute-force method faces difficulty due to the double derivative term. Fortunately, in the Fourier domain, the solution becomes much easier by completely avoiding the differentiation. For a small step size δz, the updated value for the complex electric field is

$$\boldsymbol{A}(z + \delta z) = exp^{-i(D+N)\delta z}(A)(z) \tag{A.2}$$

$$\approx exp^{-i(D)\delta z}\left[exp^{-i(N)\delta z}\boldsymbol{A}(z)\right]. \tag{A.3}$$

Now, to transform the equation into Fourier domain following substitutions are made

$$\partial/\partial x = \imath\mathbf{k}_x, \quad \partial/\partial y = \imath\mathbf{k}_y \tag{A.4}$$

$$\nabla_T^2 = \partial^2/\partial x^2 + \partial^2/\partial y^2 = -\mathbf{k}_x^2 - \mathbf{k}_y^2 \tag{A.5}$$

$$\mathbf{k}_x = 2\pi/\mathbf{x}, \quad \mathbf{k}_y = 2\pi/\mathbf{y} \tag{A.6}$$

The Helmholtz equation is represented in Fourier domain as

$$FT[\boldsymbol{A}(z + \delta z)] \approx FT[\exp^{-\imath D\delta z}]\ (FT[\exp^{-\imath N\delta z}\boldsymbol{A}(z)])$$

$$\boldsymbol{A}(z + \delta z) \approx FT^{-1}[\exp^{\imath\mathbf{k}^2\delta z}(FT[\exp^{-\imath N\delta z}\boldsymbol{A}(z)])]$$

with the following constrains

$$\nabla_T^2 = -\mathbf{k}_x^2 - \mathbf{k}_y^2 = -\mathbf{k}^2, \mathbf{k}_x = 2\pi/x, \mathbf{k}_y = 2\pi/y.$$

The key factor that lies here is transformation $FT[exp^{-iD\delta z}] = exp^{i\mathbf{k}^2\delta z}$.

A.2. Probing

The beam as it propagates through the atomic cloud approaches the HF fiber tip. At this stage the power that is detected is altered by two factors. First, depending upon the radial size of the beam, it can be masked on the Fiber front end and the second factor comes from the mode overlap of the beam with an unaltered beam profile.

A. Appendix 1

The Figure'A.1 depicts the masking effect as the detection is only made to the part of the beam which lies in the central zone. The remaining power after masking is calculated as

$$P = \int_A I(x,y)dxdy, \tag{A.7}$$

where A is the total allowed area for the beam to enter into the fiber.

Fiber tip　　　　　　　　　　　　　　Masked area
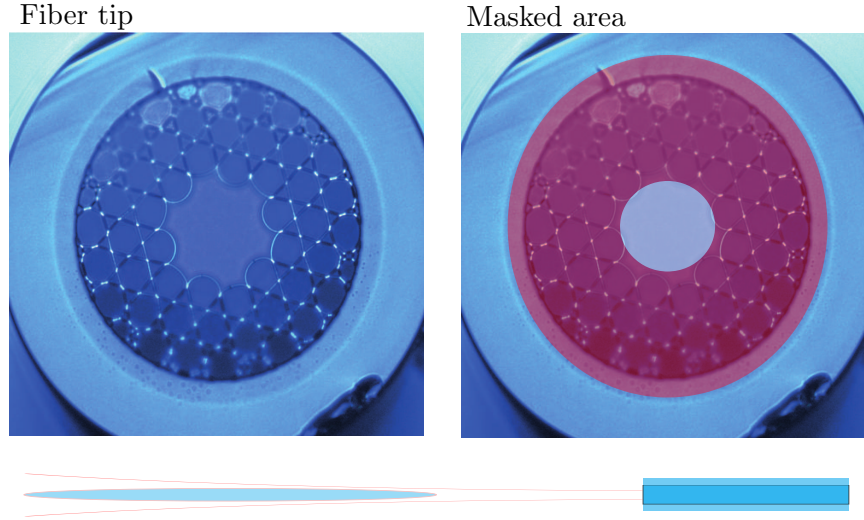
Figure A.1.: model for probing the beam.

The mode overlap is calculated by the integration of the field profiles as follows

$$\eta = \frac{|\int \mathcal{E}_1^* \mathcal{E}_2 dA|^2}{\int |\mathcal{E}_1|^2 dA \int |\mathcal{E}_2|^2 dA}, \tag{A.8}$$

where, $\mathcal{E}_1$ and $\mathcal{E}_2$ are electric field profile for absence and presence of atomic media. It is evident, the term η modifies the coupling efficiency of the beam into the fiber. The total power detected on the PMT is simply calculated by taking a product of the equations A.7 and A.8.

$$P_{tot} = \eta P. \tag{A.9}$$

A.3. Python code for beam propagation

```
import matplotlib.pyplot as plt   # Import library for direct plotting functions
import numpy as np                # Import Numerical Python
from IPython.core.display import display, HTML #Import HTML for formatting output

#%% Gaussian beam specification
w0 = 20*1.e-6  # beam waist
x_um = np.linspace(-15*w0*1.e6,15*w0*1.e6,100) # radial distribution in um
x = x_um *1.e-6 # radial distribution in m
y_um = np.linspace(-15*w0*1.e6,15*w0*1.e6,100) # radial distribution in um
y = y_um *1.e-6 # radial distribution in m

E0 = 1
```

A. Appendix 1

```
lam= 780*1.e-9
k0  = 2*np.pi/lam
n0  = 1
zr = w0**2*n0*np.pi/lam # rayleigh range
def gaussbeam(x,y,z):
        wz = w0*np.sqrt(1+((z-z0)/zr)**2)
        Rz = (z-z0)*(1+(zr/(z-z0))**2)
        E = E0 * w0/wz * np.exp(-(x**2+y**2)/(1*wz**2)  + 1j*k0*(x**2+y**2)/(2*Rz)
-1j*np.arctan((z-z0)/zr))# + 1j*k*(z-z0))#  + 1j*(k*z-w*t))
        return E
z0 = 0

#%% create beam profile using gaussian approximation
xx1,yy1  = np.meshgrid(x,y)
z1 = np.linspace(-.0015,.0005,200)  # position of the beam along the beam propagation axis
efld = []
for i in range(len(z1)):
        zz1 = z1[i]
        efld.append(gaussbeam(xx1,yy1,zz1))
        efld = np.array(efld)
efield = np.abs(efld[150])**2 # beam profile at the gaussian beam waist

#%% atomic cloud information for simulation
n_at = 120000         # number of trapped atoms
l_cl = 1*1.e-3        # length of atomic cloud
sigma_cl = 9*1.e-6    # radial distribution of the cloud
def at_den(sigma,N):  # returns atomic density
        c = N/(2*np.pi*l_cl*sigma**2)
        rho = c*np.exp(-(xx1**2+yy1**2)/(2*sigma**2))
        return rho
rho = at_den(sigma_cl,n_at)

#%% calculate succeptibility, chi using the rho
lam = 780*1.e-9                         # wavelength in nm (780 nm is resonant for Rb atoms)
sigma0 = 3*lam**2/(2*np.pi) # scattering cross section
Gamm = 2*np.pi*6.067*1.e6   # Natural linewidht of Rb atoms
k = 2*np.pi/lam             # wavenumber
det = np.linspace(-50,50,50)    # laser detuing in MHz
del_p = det*2*np.pi*1.e6        # detuing in Hz
def lineshape(detuning,rho):    # returns succeptibility for two level system
        trm1 = -sigma0*rho/k
        trm2 = 2*detuning/Gamm -1j
        trm3 = 1 + 4*(detuning/Gamm)**2
        chi = trm1*trm2/trm3
        return chi
chi = []
for i in range(len(det)):
        chi.append(lineshape(del_p[i],rho))
chi = np.array(chi)             # succeptibility for all detunings
nr  = 1 + 1/2* np.real(chi)     # real part of refractive index
ni  = 1/2* np.imag(chi)         # imaginary part of refractive index


#%% Set axes in the frequency basis (FT)
dx = x[1]-x[0]
dy = y[1]-y[0]
kx = np.fft.fftfreq(x.shape[0])*2*np.pi/dx
ky = np.fft.fftfreq(y.shape[0])*2*np.pi/dy
kkx,kky = np.meshgrid(kx,ky)

#%% FFT beam propagation integral
dz = z1[1] - z1[0]  # step size along the beam propagation direction
in_fld = efld[0]    # initial electric field at the input of the cloud
k0 = 2*np.pi/lam         # wavenumber
beta = k0

def fftbpm(in_fld,chi,nr):
fftfld1 = np.fft.fft2(in_fld)
ifftfld = fftfld1*np.exp(-1j*(kkx**2+kky**2)*dz/(2*beta*nr))
out_fld = np.fft.ifft2(ifftfld)*np.exp(1j*k0/(2*nr**2)*chi*dz)
return out_fld

pos_cld = z1[0]   # initial position of the cloud

def fftcal(in_fld,chi,nr):
phi_z = []
for i in range(len(z1)):
if i%(len(z1)/10) ==0:
print('.',end='')
if z1[i] < pos_cld:                             # before the cloud
out_fld = fftbpm(in_fld,0,1)
phi_z.append(in_fld)
in_fld = out_fld
if (z1[i] < pos_cld + l_cl) * (z1[i] >= pos_cld):       # cloud region
```

A. Appendix 1

```
out_fld = fftbpm(in_fld,chi,nr)
phi_z.append(in_fld)
in_fld = out_fld
if z1[i] >= pos_cld + l_cl:                                  # after the cloud
out_fld = fftbpm(in_fld,0,1)
phi_z.append(in_fld)
in_fld = out_fld
phi_z = np.array(phi_z)
return phi_z

#%% generate list of x,y,z electric field profile for different detuning
xt = round(len(x)/2) # middle of the beam (along x or y axis)
psi1 = []
for i in range(len(det)):
        in_fld = efld[0]
        phph = fftcal(in_fld,chi[i],nr[i])
        psi1.append(phph.T[xt])
        print(i)
psi1 = np.array(psi1)          # complex electric field of the beam
psi0 = fftcal(in_fld,0,1)      # reference complex electric field (without atomic presence)
gaus_fld_ref = efld.T[xt]      # reference gaussian propagation (somewhat analytical solution)
fft_fld_ref = psi0.T[xt]       # reference fft model, numerical solution
fr_ind = 14
fft_fld_sig = psi1[fr_ind]     # reference cloud signal, numerical solution
rad1,ax1 = np.meshgrid(x,z1) # meshgrid of radial and axial vectors
gaus_int_ref = np.abs(gaus_fld_ref)**2
fft_int_ref = np.abs(fft_fld_ref)**2
fft_int_sig = np.abs(fft_fld_sig)**2

#%% gaussian overlap integral to estimate the total transmission
def effcnc(sig1,sig0,x):
ef1 = sig1
ef0 = sig0
X = x
ov1 = (np.abs( np.sum(np.conjugate(ef1)*ef0*np.pi*np.abs(X)) ) )**2
ov2 = (np.sum(   (np.abs(ef1))**2*np.pi*np.abs(X) )   )
ov3 = (np.sum(   (np.abs(ef0))**2*np.pi*np.abs(X) )   )
efcnc = ov1/(ov2*ov3)
return efcnc

#% mode filtering and final detection
fib_core_rad = 26*1.e-6
msk_ind = np.arange(len(x))
cmpr1 = len(x)-(-fib_core_rad < x) * msk_ind[::-1]-1
cmpr2 = (fib_core_rad > x) * msk_ind
msk1 =np.min(cmpr1)
msk2 =np.max(cmpr2)
fr_ind = 10
fftfld = psi1[fr_ind]
reffld = psi0.T[xt]
def pwrout(fftfld):
        pwr = []
        efc = []
        for i in range(len(z1)):
                pw = np.abs(fftfld.T[i])**2 * np.abs(x)
                ef1 = fftfld.T[i]
                ef0 = reffld.T[i]
                if z1[i] < 0:
                        pwr.append(np.sum(pw))
                        efc.append(effcnc(ef1,ef0,x))
                else:
                        pwr.append(np.sum(pw[msk1:msk2]))
                        efc.append(effcnc(ef1[msk1:msk2],ef0[msk1:msk2],x[msk1:msk2]))
                pwr = np.array(pwr)
                pwr = pwr/pwr[0]
                efc = np.array(efc)
        return pwr, efc
pout = []
efcc = []
for i in range(len(det)):
        print('.', end='')
        fr_ind = i
        fftfld = psi1[fr_ind]
        pout.append(pwrout(fftfld)[0])
        efcc.append(pwrout(fftfld)[1])
pout = np.array(pout)
efcc = np.array(efcc)
#%% final transmission plot vs detuning
loc = 160
op = pout.T[loc]
ce = efcc.T[loc]
out_tot = op*ce
```

B. Appendix 2

B.1. Verilog code for FPGA sequence generator

The top level Verilog code for the FPGA pulse generator, Top.v:

```verilog
module top(
        input CLK,
        input rst,
        output TXD,
        input RXD,
        output [7:0]LED);
wire [7:0] rx_data;
wire rcvd;
clk_new clk_new(
        .CLK_IN1(CLK),        // IN
        .CLK_OUT1(CLK_OUT),   // OUT
        .RESET(RESET),        // IN
        .LOCKED(LOCKED));     // OUT
rx_ser serial_rx (
        .c_rx(CLK_OUT),
        .rxd(RXD),
        .flag(rcvd),
        .rx_1(rx_data));
reg reset;
reg we;
reg [11:0] addr;
reg [47:0]   din;
wire [47:0] dout;
bram bram (
        .clka(CLK_OUT), // input clka
        .rsta(reset), // input rsta
        .wea(we), // input [0 : 0] wea
        .addra(addr), // input [11 : 0] addra
        .dina(din), // input [47 : 0] dina
        .douta(dout) // output [47 : 0] douta
        );
reg [7:0] data;
reg [39:0] tim;
reg trig;
reg [30:0] cntr;
reg x;
reg [15:0] seq_len;
reg [15:0] lnum;
reg [7:0] lstr;
reg [7:0] lend;
reg [7:0] llen;
reg [15:0] lcnt;
reg [15:0] lnum2;
reg [7:0] lstr2;
reg [7:0] lend2;
reg [7:0] llen2;
reg [15:0] lcnt2;
reg [7:0] step;  // state machine cases
reg [7:0] ind;
always @ (posedge CLK_OUT)begin
if(rcvd == 1)
begin
        case(step)
        8'd0: begin
                if(rx_data == 8'b01110111)  // press w button to enable writing
                        begin
                        step <= 8'd1;   // go to next case step
                        ind <= 8'd47;
                        addr <= 0;
                        trig <= 0;
                        end
                else if(rx_data == 8'b01110010)
                        begin
                        addr <= 0;
                        trig <= 1;
```

```verilog
                        step <= 8'd0;
                    end
                else begin
                        step <= 8'd0 ;
                    end
            end
        8'd1: begin
                seq_len[15:8] <= rx_data;   // receive length byte2
                step <= 8'd2;
                end
        8'd2: begin
                seq_len[7:0] <= rx_data;    // receive length byte1
                step <= 8'd3;
                end
        8'd3: begin
                lstr[7:0] <= rx_data;    // start of the loop byte
                step <= 8'd4;
                end
        8'd4: begin
                lend[7:0] <= rx_data;    // end of the loop byte
                step <= 8'd5;
                end
        8'd5: begin
                llen <= lend - lstr;     // end - start loop
                lnum[15:8] <= rx_data;   // number of reps
                step <= 8'd6;
                end
        8'd6: begin
                lnum[7:0] <= rx_data;    // number of reps
                step <= 8'd7;
                end
        8'd7: begin
                lstr2[7:0] <= rx_data;    // start of the loop byte
                step <= 8'd8;
                end
        8'd8: begin
                lend2[7:0] <= rx_data;    // end of the loop byte
                step <= 8'd9;
                end
        8'd9: begin
                llen2 <= lend2 - lstr2;  // end - start loop
                lnum2[15:8] <= rx_data;  // number of reps
                step <= 8'd10;
                end
        8'd10: begin
                lnum2[7:0] <= rx_data;    // number of reps
                step <= 8'd11;
                end
        8'd11: begin
                if(we ==1)
                        begin
                        we <= 0;
                        addr <= addr + 1;
                        end
                din[ind -:8]  <= rx_data;
                data <= din[47:40];
                ind <= ind - 8'd8;
                if(ind == 8'd7)
                        begin
                        we <= 1;
                        ind <= 8'd47;
                end
                if (addr == seq_len)
                        begin
                        step <= 8'd12;
                        we <= 0;
                        ind <= 8'd0;
                end
                end
        8'd12: begin
                step <= 8'd0;
                end
        endcase
end
if(rst == 0 && x == 0)    // external trigger
        begin
        addr <= 0;
        trig <= 1;
        x <= 1;  // latch
        end
if(rst == 1 )   // enables only single trigger event
        begin
        x <= 0;
        end
```

```
if(trig == 1 )     // readout data stored in bram
        begin
        data <= dout[47:40];   // dout stored to output
        cntr <= cntr + 1;
        tim <= dout[39:0];
        if(cntr >= tim)
                begin
                if(addr == lend)   // first loop
                begin
                cntr <= 0;
                if(lcnt < lnum)begin
                addr <= addr - llen;
                lcnt <= lcnt + 1;
                end
        else begin
                addr <= addr + 1;    // bram address increases
                cntr <= 0;
                lcnt <= 8'd0;
                end
        end
else if(addr == lend2)   // second loop
        begin
        cntr <= 0;
        if(lcnt2 < lnum2)begin
        addr <= addr - llen2;
        lcnt2 <= lcnt2 + 1;
        end
else begin
        addr <= addr + 1;    // bram address increases
        cntr <= 0;
        lcnt2 <= 8'd0;
        end
end
else begin
        addr <= addr + 1;    // bram address increases
        cntr <= 0;
        end
end
if(addr == seq_len)   // sets limit on the bram address
        begin
        trig <= 0;
        end
end
end
assign LED = data;
assign TXD = RXD;
endmodule
```

Verilog code for UART communication, rx.v:

```
module rx_ser
#( parameter clk_per_bit = 200)
(input c_rx,input rxd,output flag,output [7:0]rx_1);

reg r_rx;
reg rx;
reg [11:0]counter = 0;
reg i_flag;

reg [2:0] bit_index; // bit received
reg [7:0] rx_byte;   // recieved serial byte data
reg [2:0] states = 0;  // states for serial data bit

always @ (posedge c_rx)begin
        r_rx <= rxd;
        rx <= r_rx;
        end


always @(posedge c_rx) begin
        case(states)
        3'd0: begin            // Triggers on rx low
        counter <= 0;
        bit_index <= 0;
        if(rx == 0) begin
                states <= 3'd1;
                end
        else begin
                states <= 3'd0;
                end
        end

        3'd1: begin
```

```verilog
                    if(counter == (clk_per_bit -1)/2) begin
                    if(rx == 0) begin
                            counter <= 0;
                            states <= 3'd2;
                            end
                    else begin
                            states <= 3'd0;
                            end
                    end
            else
                    begin
                    counter <= counter + 1;
                    states <= 3'd1;
                    end
            end

            3'd2: begin        // receives all the 8 bits
                    if(counter == clk_per_bit -1) begin
                            counter <= 0;
                            rx_byte[bit_index] <= rx;
                    if(bit_index < 7) begin
                            bit_index <= bit_index + 1;
                            states <= 3'd2;
                            end
                    else begin
                            states <= 3'd3;
                            end
                    end
                    else
                            begin
                            counter <= counter +1;
                            states <= 3'd2;
                    end
                    end
            3'd3: begin    // closing the state machine
                    if(counter < clk_per_bit -1) begin
                            counter <= counter + 1;
                            states <= 3'd3;
                            end
                    else begin
                            counter <= 0;
                            states <= 3'd4;
                            i_flag <= 1;   // enalbles flag
                            end
                    end
            3'd4: begin   // resets the state machine
                    states <= 3'd0;
                    i_flag <= 0;
                    end
            endcase
            end
assign rx_1 = rx_byte;
assign flag = i_flag;
endmodule
```

C. Appendix 3

C.1. HC fiber cleaning for UHV

The HC fiber is required to be UHV grade cleaned in order to maintain good vacuum level inside the chamber for laser cooling and trapping experiments. Although the fiber material is non-porous and has no issues if placed in UHV chamber however, due to the micro structures such as the fine holes inside the fibers can trap unwanted particles which can degas for enormously long times. These narrow capillaries can act as a differential pumping stage which significantly reduced the throughput rate of pumping out the particles from the inner walls. To circumvent the issues, the fiber is cleaned in a separate pumping system where severely stronger measures can be taken without any risk. The cleaning setup is shown in the Figure C.1 where fibers are placed inside the narrow tube. One of the main openings is attached to a valve which can be opened to flush the system with N2 gas. The idea is to first pump down the system to pressures below 10^{-10} bar of the main chamber. At this pressure, the fibers start to release some particles, however the rate is extremely low due to the reduced pumping rates. To speed up the process the section where fiber is placed is heated to temperatures above 180^{0}C which increases the pressure inside the fiber hence the throughput speed goes high. Now, the pumping stages are turned off and simultaneously, dry N2 is flushed into the chamber. The N2 would take the empty space inside the HC fiber. Now, the pumping process with bakeout is repeated. The argument is that the N2 molecules would eventually replace all the unwanted particles inside the fiber. This has two aspects: first, pumping out N2 is easier and should not affect the main experimental chamber and the second reasoning is to deal with the challenge in transporting the cleaned fiber into the main UHV chamber. Since the fiber would be filled with N2 at ambient pressure, the inflow of unwanted particles would be limited.
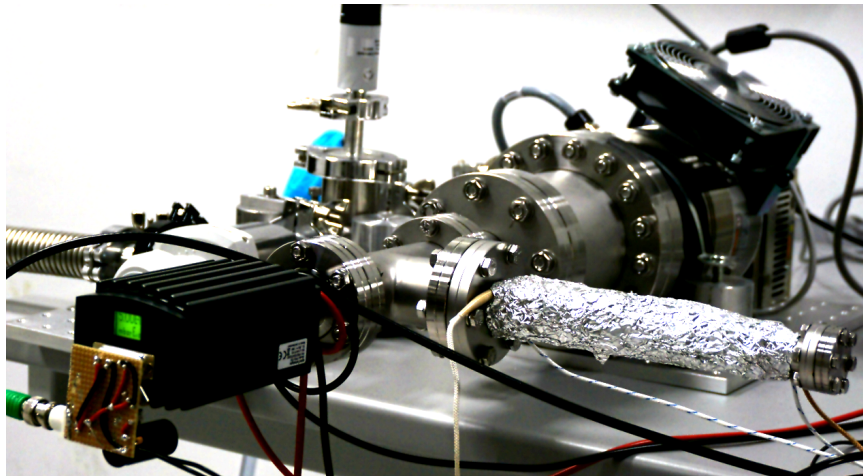
Figure C.1.: Fiber cleaning pumping system.

Bibliography

[1] Niels Bohr.
On the constitution of atoms and molecules, part i.
Philosophical Magazine, 26:1–25, 1913.

[2] O Firstenberg, C S Adams, and S Hofferberth.
Nonlinear quantum optics mediated by rydberg interactions.
Journal of Physics B: Atomic, Molecular and Optical Physics, 49(15):152003, 2016.

[3] Michael Fleischhauer, Atac Imamoglu, and Jonathan P. Marangos.
Electromagnetically induced transparency: Optics in coherent media.
Rev. Mod. Phys., 77:633–673, Jul 2005.

[4] H J Kimble.
The quantum internet.
Nature, 453:1023, jun 2008.

[5] A. Kuhn, M. Hennrich, T. Bondo, and G. Rempe.
Controlled generation of single photons from a strongly coupled atom-cavity system.
Applied Physics B, 69(5):373–377, Dec 1999.

[6] J. D. Pritchard, D. Maxwell, A. Gauguet, K. J. Weatherill, M. P. A. Jones, and C. S. Adams.
Cooperative atom-light interaction in a blockaded rydberg ensemble.
Phys. Rev. Lett., 105:193603, Nov 2010.

[7] J P Reithmaier, G Sęk, A Löffler, C Hofmann, S Kuhn, S Reitzenstein, L V Keldysh, V D Kulakovskii, T L Reinecke, and A Forchel.
Strong coupling in a single quantum dot–semiconductor microcavity system.
Nature, 432:197, nov 2004.